Cool Things you can do with Lasers

Aidan Arnold

A thesis submitted for the degree of
Master of Science
at the University of Otago, Dunedin,
New Zealand

August 19, 1996

Abstract

Theoretical and experimental investigations into a variety of laser cooling phenomena are presented. An overview of the history of laser cooling is followed by an in-depth study of analytic Doppler theory, as applied to both MOTs and optical molasses. The 3D distributions of Gajda *et al.* [27] are generalised, allowing the inclusion of both intensity and frequency imbalances.

Forces arising from reradiation and absorption are then added to the description, with particular emphasis on the non-conservative absorptive force. Constant-temperature solutions do not appear to exist for the differential equations which arise in such a regime, raising questions about the validity of commonly used density relations based on this assumption. Possible errors in the formalism are covered, as well as their means of rectification.

Work on the theoretical Doppler forces involved in ring-shaped MOT structures is reviewed, and possible solutions to the present discrepancy between theoretical and experimental studies in this field are discussed in the context of reradiation. Analytic theory as well as a Doppler Monte Carlo simulation are employed.

A brief description of sub-Doppler theory is succeeded by a theoretical study of the 3D standing waves in laser cooling apparatus, focusing on the relative phases of the laser beams. Properties of various laser polarisation configurations are discussed with respect to the Sisyphus parameter p, of Steane *et al.* [71]. The (analytic) variance of p is evaluated spatially, enabling a simple comparison between different configurations and any combination of relative beam phases.

The thesis concludes with an experimental investigation attempting to replicate the method of Kasevich *et al.* [39]. The expected behaviour of an optical molasses expansion is also considered.

Acknowledges meant

Sleep, the final frontier. These are the voyages of the starship Titanic.... its continuing mission: to boldly type where no language has gone before.

At last, a page where I am free, FREE to type whatever and however I like. Firstly of course I would like to thank my super super, Peter Manson, for somehow managing to rein me in when tangents with flashing orange lights drew my attention away from the big picture. You have been a true saint in the lab (do they give VCs for work on dye lasers?) and always found time for Kirsten and myself in a rather hectic schedule. All credit to you!

And (yes, I used 'and' to start a paragraph!) of course all credit to my friend and trusty sidekick Kirsten (well actually I was the sidekick, but don't tell anyone). I would've been handing my MSc to the sanatorium staff if it weren't for your help in the lab... the most important part of an MSc is to have somebody to complain about things with!

All credit to Don too, for somehow managing to revive the Argon whenever it died/broke legs/caught the flu.

A big ta flies across the Tasman to Jürgen and Ian for my groovy 'working' holiday at ANU. My soldering benefited immensely as did my appreciation of sodium atoms (NOT!)

Many thanks to Ann-Marie for her veritable library of relevant references, and for providing the answers to a zillion silly questions (you show great patience, maybe you should become a lecturer? :-)

A large quantity of awe must go to Peter Stroud for his uncanny ability to create exactly what I wanted in a third of the time I wanted it in. Thanks also to the Electronics technicians for explaining the significance of various other-worldly gizzmos, and telling me where to go (and get them from).

A big thanks to Murray for his invaluable help with C programming. I still don't understand what the first few lines of code do, but that's no fault of yours!

And :-) now I would like to thank my friends for somehow managing to stay friends even if I didn't exist in the same temporal plane as them. No time to say hi to everyone (just hit me if you have been omitted), but especially thanks to Sonia for her excellent, often well-timed emails, Dave (you big freaker) for his proof-reading and midnight hot chocolates, Peter (this means I finished first) for calling me mad at every opportunity (mirror, mirror, on the wall, but who's the maddest of them all?), Paul for the hotly-contested motorbike races, air hockey and T-Meks (they improved my typing no end) as well as advice on how to beat the MSc system! Last of all (this is not in any particular order by the way) thanks to Mum and Dad for providing me with life-sustaining food on Sundays, a roof over my head *every* day, and generally just for being who they are—really cool people!

Right, it's 5am and I'm going to sleep...... good morning.

Contents

Chapter 1

Introduction

1.1 Overview of Trapping and Cooling

1.1.1 Radiation Pressure

In 1881 Maxwell postulated that light could exert pressure on matter, and this was verified experimentally in 1901 by Lebedev in Russia and also by Nichols and Hull in the US. Einstein, in 1909, showed theoretically that light could be envisaged as quanta (photons) with discrete momenta. The deflection of a beam of sodium atoms by light resonant with a sodium energy level transition, observed in 1933 by Frisch, confirmed that light could transfer momentum to atoms.

The magnitude of the momentum of a single photon is given by:

$$p = \frac{h}{\lambda} = \hbar k, \tag{1.1}$$

where h is Planck's constant, $\hbar = \frac{h}{2\pi}$ and λ is the wavelength of the light. The direction of the momentum vector $\mathbf{p}$ is parallel to the direction of propagation of the light. The photon absorption rate of a two-level atom is given by the Lorentzian function [43]:

$$R(I, \omega, \omega_0) = \frac{\Gamma}{2} \frac{I/I_S}{1 + I/I_S + (\frac{2}{\Gamma})^2(\omega - \omega_0)^2}, \tag{1.2}$$

where $1/\Gamma$ is the excited state lifetime (Γ is also the full width at half maximum, FWHM, of the Lorentzian), I is the intensity of the light, I_S is the saturation intensity for the transition, ω is the angular frequency of photons as observed by the atom, and ω_0 is the angular frequency corresponding to the energy difference between the ground and excited electronic states of the atom. Throughout this thesis the saturation intensity for a given energy level transition is defined by the equation $I/I_S = 2\left(\Omega/\Gamma\right)^2$, where Ω is the Rabi frequency of the transition. Definitions for Ω vary, however this form has been used more frequently in recent literature [71], [74], [7], [29].

An approximation for the rate of absorption will be used in this chapter:

$$R(I, \omega, \omega_0) = \frac{\Gamma}{2} \frac{I/I_S}{1 + (\frac{2}{\Gamma})^2(\omega - \omega_0)^2}. \tag{1.3}$$

This is the low-intensity ($I << I_S$) limit and the full effects of saturation will be discussed in chapter 2.

By applying the relation $\mathbf{F} = \frac{d\mathbf{p}}{dt}$, it follows that an atom absorbing photons with momenta $\hbar\mathbf{k}$, at a rate R, will experience a force: $\mathbf{F} = \hbar\mathbf{k}R$, and this force is in the direction of propagation of the photons. Thus

$$\mathbf{F} = \frac{\hbar\mathbf{k}\Gamma}{2} \frac{I/I_S}{1 + (\frac{2}{\Gamma})^2(\omega - \omega_0)^2}. \tag{1.4}$$

This force equation is only valid when all photons have equal momenta $\hbar\mathbf{k}$—i.e. the light is uni-directional. The force derivation also assumed that an atom continually absorbs photons—however every photon ab-

sorbed by an atom must in turn be emitted by spontaneous or stimulated emission. Only the low intensity regime will be considered here, and stimulated emission can therefore be neglected.

Each photon emission ensures an atom will return from its excited state to its ground state, where it can absorb another photon. When an atom spontaneously emits a photon, it does so in a random direction. The full nature of spontaneous emission will be discussed in detail later, but in particular spontaneous emission is symmetric. This property ensures that the total recoil an atom receives from spontaneous emission will average to zero over time. The force equation 1.4 therefore details the macroscopic force on an atom averaged over several absorption-emission cycles.

It is clear that the force in equation 1.4 is strongest when $\omega = \omega_0$ and the incident light is intense. For this reason Ashkin [4], in 1970, suggested the use of lasers to observe the effect of light on atoms: lasers can create extremely high intensities over narrow, tunable frequency domains. Ashkin studied the effect of laser light pressure on micron sized particles and also created a dipole trap which acted on particles situated between two counter-propagating laser beams. Light causes a perturbation, proportional to its intensity, in the energy levels of an atom—the AC Stark shift. A spatial variation in intensity therefore creates a spatial variation in an atom's energy, i.e. a force on the atom. In the dipole traps this force is configured to produce confinement [16], [1].

1.1.2 Optical Cooling

In 1975 Hänsch and Schawlow [31] first considered the use of laser radiation to cool atoms. An atom with velocity $\mathbf{v}$ travelling in a laser beam containing photons of wavevector $\mathbf{k}_L$ (also in the lab. frame) will observe photons with Doppler-shifted angular frequency $\omega = \omega_L - \mathbf{k}_L \cdot \mathbf{v}$. Both $\mathbf{v}$ and $\mathbf{k}_L$ are measured in the laboratory frame and the subscript 'L' is used to denote laser parameters.

By defining the detuning, $\Delta = \omega_L - \omega_0$, the equation $\omega - \omega_0 = \Delta - \mathbf{k}_L \cdot \mathbf{v}$ is obtained. This can be substituted into equation 1.4 to obtain the approximate force on an atom with velocity $\mathbf{v}$. If an atomic beam, collimated along the x axis and travelling in the $+x$ direction, passes through a laser propagating in the opposite direction, i.e. $\mathbf{k}_L = -k_L \mathbf{i}$, then $\omega - \omega_0 = \Delta + k_L v_x$. Equation 1.4 becomes:

$$F_x = -\frac{\hbar k_L \Gamma}{2} \frac{I/I_S}{1 + (\frac{2}{\Gamma})^2 (\Delta + k_L v_x)^2}. \tag{1.5}$$

All atoms in the atomic beam initially have $v_x > 0$ and the force from the laser acts in the $-x$ direction—it tends to decrease an atom's x velocity. At $v_x = -\Delta/k_L$ the force magnitude is maximised, thus the largest force on the atoms will arise from negative detunings. For atoms with velocity:

$$-\Delta/k_L - \Gamma/(2k_L) < v_x < -\Delta/k_L + \Gamma/(2k_L),$$

the force magnitude is over half its maximum value and outside this velocity range the force rapidly decays to zero. The magnitude of the velocity range is $\Gamma/(k_L)$, or $\approx 6\mathrm{ms}^{-1}$ for sodium atoms ($\Gamma = 2\pi 10^7 \mathrm{rad\ s}^{-1}$, $\lambda_L = 589\mathrm{nm}$). A typical thermal beam of metal atoms has a velocity range of $\approx 10^2 - 10^3 \mathrm{ms}^{-1}$, and the force therefore only interacts with a small velocity sub-group of atoms in the beam.

Atoms within this velocity sub-group are initially decelerated, but continue to slow only whilst their velocities are resonant with the force. Outside this velocity range the force has a negligible effect on them. The velocity distribution will therefore alter before reaching an approximate equilibrium—unless the laser frequency is shifted.

If the detuning of the laser is changed so that it initially interacts with a high velocity group, and the frequency of the laser is then continuously adjusted to interact with decreasingly lower velocity groups, this has a much stronger cooling effect. At the start of the laser 'sweep' high-velocity atoms are initially cooled by the laser into a slightly lower velocity group. As the laser's frequency becomes resonant with this new velocity group, the atoms that were already in this velocity bracket are cooled, as well as the atoms obtained from the initial velocity group. In this way a metaphorical wave sweeps the velocity distribution

of the atomic beam, collecting atoms as it travels. The frequency sweep is typically stopped when the laser detuning reaches zero and the 'swept' atoms acquire a near-zero velocity. If the frequency of the laser continued increasing, then the atoms would acquire non-zero velocities in the direction opposite to their original motion—the atoms would heat up.

This method of cooling an atomic beam, chirped cooling, was first achieved experimentally by Balykin *et al.* [8] in 1979. Another cooling method, Zeeman cooling, can be achieved with a static laser frequency and was first demonstrated by Phillips and Metcalf in 1982 [55]. Chirped cooling involved altering the value of ω in equation 1.4 as the atoms' velocities decreased. A spatially varying magnetic field along the path of the atomic beam, allows the energy levels of the atom to change, and thus ω_0 changes too. In essence Zeeman cooling alters ω_0 over time, whereas chirped cooling alters ω. The symmetry of these two variables in equation 1.4 shows that both processes can be set up to have a similar effect.

In initial experiments chirp-cooled atoms were not cooled as well as expected. No real atom has only two energy levels and an atom's excited and ground states often contain several energy levels. The process of optical cooling involves several absorption-emission cycles through the same energy levels and if an atom jumps to a different ground energy level then the cooling process stops. Laser light that was resonant for the trapping transition may not be capable of exciting the atom out of this new energy level. To get around this problem 'repump' laser beams were included in experiments, at frequencies which induced atoms to return to the energy levels of the cooling cycle.

With a slow source of atoms, from a cooled atomic beam, it was now possible to investigate the effect of a cooling mechanism suggested by Hänsch and Schawlow. They noted that if counterpropagating laser beams were detuned to the red of an absorption line, the lasers would always provide a net force opposing the velocity of an atom—a damping force. The average force due to a laser beam of intensity I propagating in the $-x$ direction was obtained in equation 1.5 and the equation for the force from an equally intense counterpropagating beam can be obtained similarly. The net force of both beams, neglecting standing wave effects, can be approximated by the sum of the individual forces and is shown graphically in figure 1.1.
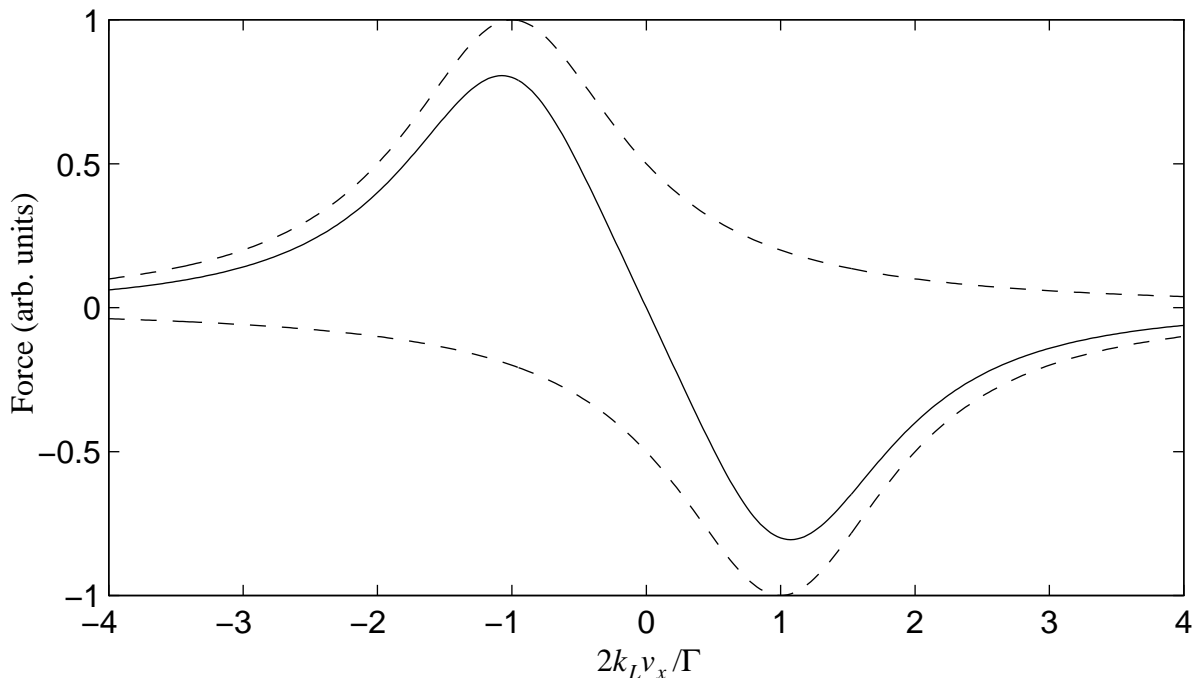

Figure 1.1: Force versus velocity (with respect to x axis) for atoms acted on by counterpropagating lasers, each with detuning $\Delta = -\Gamma/2$. The dashed curves correspond to the forces from the two individual beams, and the solid curve shows the total force.

Although the force always opposes an atom's motion, it is strongest for slower atoms. Therefore the vis-

cous light force from counterpropagating laser beams, commonly called 'optical molasses', works extremely well in cooling atoms loaded from a laser-cooled atomic beam. An important point is that the total force provides a cooling effect only when the detuning Δ of the laser beam is negative.

Optical molasses was first realised by Chu *et al.* [10] in 1985. The set-up incorporated three orthogonal pairs of counterpropagating laser beams, extending the one dimensional cooling idea to three dimensions. A temperature in sodium of $\approx 240\mu$K was obtained and as laser cooling of trapped ions had resulted in temperatures of $5 - 100$mK, and laser cooling of an atomic beam had yielded (3D) temperatures of $50 - 100$mK, optical molasses was a considerable improvement on previous cooling techniques.

The Doppler temperature, T_D, was then believed to represent the minimum temperature obtainable by laser cooling. Derivations of this temperature can be found in refs. [72] and [43], and it will be derived in a more general framework in chapter 2. The Doppler temperature is:

$$T_D = -\hbar\Gamma\frac{1 + (2\Delta/\Gamma)^2}{8k_B\Delta/\Gamma}$$

and it can be easily shown that T_D has a minimum value of $T_D = \hbar\Gamma/(2k_B)$ when $2\Delta/\Gamma = -1$. The Doppler temperature for sodium is 240μK, and so the experiment of Chu *et al.* approached what was then considered to be the lowest temperature attainable by laser cooling.

1.1.3 Optical Trapping

A drawback of 'optical molasses' is that although the molasses cools atoms it does not confine them—they drift away via Brownian motion. A magneto-optical trap, or MOT, which both cooled and trapped atoms was first demonstrated by Raab *et al.* in 1987. The trapping scheme in the MOT was based on an idea of Jean Dalibard [58], and allowed atoms to be trapped in the intersection of counterpropagating laser beams similar to those used in optical molasses. Necessary refinements required to create a MOT were the use of lasers with carefully chosen circular polarisations, and the application of an inhomogeneous magnetic field.

Like optical molasses, the underlying processes behind the MOT are most easily illustrated in one dimension, but readily extend to three. Suppose that a linear magnetic field $\mathbf{B} = (0, 0, \beta z)$ exists along the z axis. This field cannot exist physically, due to Maxwell's equations, however magnetic fields which vary linearly in three dimensions *can* be obtained and the 1D field will suffice for a theoretical illustration.

Consider an atom with an $F = 0$ ground state and $F' = 1$ excited state, where F denotes the total angular momentum quantum number. The magnetic field experienced by the atom causes a Zeeman effect, lifting the degeneracy of the excited state sublevel energies. The change in energy of the $F' = 1, m_{F'}$ level is $\Delta E = g_U(F')\mu_B m_{F'} B = \mu_B m_{F'}\beta z$, where μ_B is the Bohr magneton and $g_U(F')$ is the upper-state Landé g-factor. Throughout this thesis a Landé g-factor of one will now be assumed, for simplicity, although the results readily extend to other g-factors. The angular frequency corresponding to the $F = 0 \rightarrow F' = 1, m_{F'}$ energy transition is thus:

$$\omega(z) = \omega_0 + \omega_B m_{F'}\beta z, \tag{1.6}$$

where $\omega_B = \mu_B/\hbar$.

If the laser propagating in the $+z$ direction has σ^+ polarisation, then it can only excite transitions of the form $F = 0 \rightarrow F' = 1, m_{F'} = +1$. If the counterpropagating laser beam has σ^- polarisation, it can only drive $F = 0 \rightarrow F' = 1, m_{F'} = -1$ transitions.

Equation 1.3 shows that an atom is more likely to absorb a photon the closer ω is to ω_0. In this situation, the frequency of either laser, as seen by an atom, is $\omega \approx \omega_L$ when v_z is small. Also the energy level difference between the ground and excited states (ω_0 in equation 1.3) is given by $\omega(z)$. Proximity of ω_L to $\omega(z)$ therefore increases the probability of photon absorption. In figure 1.2 this corresponds to shorter distances between the photon and excited state energies.

When $z < 0$ the $m_{F'} = +1$ upper state energy is closer to the photon energy than the $m_{F'} = -1$ upper state. Thus if $z < 0$ and the laser beams have equal intensities, photons which excite the atom to
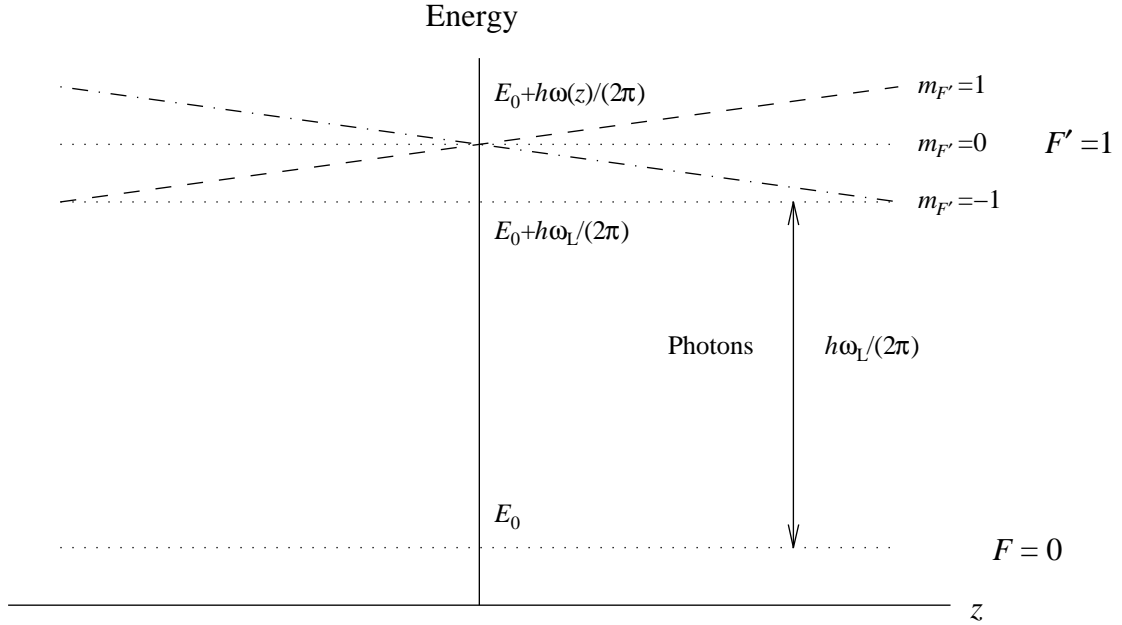
Figure 1.2: Energy levels of an atom versus z position.

the $m_{F'} = +1$ energy level, i.e. σ^+ photons which are only available from the $+z$ laser, are more likely to be absorbed than their $-z$ laser counterparts. Similarly when $z > 0$ photons from the $-z$ laser beam are more likely to be absorbed than those from the $+z$ beam. The imbalance in radiation pressure from the laser beams creates a force in the $-z$ direction for atoms with $z > 0$, and a force in the $+z$ direction for atoms with $z < 0$. Thus a trapping force exists, confining atoms to the region near $z = 0$.

The MOT was found to be extremely robust—several of the trap parameters, including the frequency, intensity, intensity imbalances and ellipticity of the lasers, could be varied, yet a trap was still obtained. Another feature of the first MOT was the appearance of ring-shaped clouds of atoms when the laser beams were misaligned. Later papers by other authors studied these structures.

Further investigation indicated that a MOT could capture atoms loaded from a cooled atomic beam with velocities up to $\approx 12\mathrm{ms}^{-1}$. It was also found that a comparable number of atoms could still be collected from an uncooled atomic beam, and this lead Monroe it et al. [50] to attempt capturing atoms directly from a room-temperature vapour. Their success in 1991 greatly simplified the MOT set-up because a substantial vacuum apparatus was previously necessary to provide a slowed atomic beam. Capture from a background vapour meant that only a small cell was necessary for trapping, and that the cumbersome atomic beam was extraneous.

The MOT greatly increased the density of cold atoms obtainable through laser cooling, however there are limits on attainable densities. The atoms in a MOT absorb photons from the laser beams and then re-radiate them in a random, approximately isotropic, distribution. The atoms therefore behave like point sources of light, and will therefore also contribute to the radiation pressure felt by other atoms in the trap. The force between two atoms is proportional to $1/r^2$ where r is the distance between the atoms. It is a repulsive force which limits the density of atoms in the MOT. The theoretical density in a MOT will be discussed in more detail in section 3.1.

Mechanisms for increasing the density limit of a MOT were found in the 'dark' and 'compressed' MOTs [41], [53].

1.1.4 Sub-Doppler Cooling

In 1988 Lett *et al.* [42] observed sodium atoms in optical molasses with the lowest temperature previously recorded: $43 \pm 20\mu$K. This result was surprising, given that the temperature was below the generally accepted minimum temperature of 240μK predicted by Doppler theory for sodium.

The experimental set-up was similar to that in ref. [10], and involved a laser-cooled atomic beam loading the intersection region of three orthogonal counter-propagating beams with cooled atoms. The optical molasses was formed in a region where the magnetic field had been reduced to $< 20\mu$T $= 200$mG; this was a particularly important feature.

Theoretical explanations for the low observed temperatures soon followed. Two independent groups [32] suggested theories involving polarisation gradients created in the standing waves of counterpropagating laser beams, as well as a complicated combination of optical pumping and atomic-state-dependent transition rates. In chapter 4 this theory will be covered with greater depth.

Sub-Doppler temperatures were also observed in a caesium MOT [70], [71], and such MOTs can provide a dense sample of low-temperature atoms.

The new limiting temperature for laser-cooled atoms was postulated to be the recoil limit: $T_R = \frac{\hbar^2 k_L^2}{2m k_B}$, the temperature at which the average speed of an atom is the recoil velocity induced by a single photon. Experiments have yielded temperatures lower than the recoil limit through velocity-selective coherent population trapping, VSCPT [5]. The atomic density is low in this configuration, however.

Further cooling through optical processes appeared to be difficult, due to the inherent heating effects that are produced by laser light. The cooling laser beams can

be turned off however, and new mechanisms were then employed which continued to lower atomic temperatures.

1.1.5 Magnetic Trapping

Due to their associated charge, ions can easily be confined by means of electric and magnetic fields [37]. It is their charge which also limits the temperature and density to which ions can be cooled—the repulsive force between any two ions produces a decrease in density. Neutral atoms interact together only weakly, but as they have no electric dipole moment, they cannot be trapped by electric fields. Atoms have a magnetic dipole moment however, and a force can be exerted on atoms by magnetic field gradients. This property was used to trap neutral atoms, although magnetic traps do not cool the atoms they confine.

The basic principle behind the magnetic trap involves the potential energy of a magnetic moment $\boldsymbol{\mu}$ in a magnetic field $\mathbf{B}$:

$$U(\mathbf{r}) = -\boldsymbol{\mu} \cdot \mathbf{B}.$$

If the magnetic field in the atom's frame changes slowly enough that the magnetic moment of the atom can follow it, the magnetic moment will precess, at a fixed angle, around the magnetic field during the atom's motion through the trap. The projection of the magnetic moment onto the magnetic field vector is therefore constant—$g_L(F)\mu_B m_F$, where the atom's ground state total spin is F and g_L is the associated Landé g-factor. The potential can thus be written:

$$U(\mathbf{r}) = -g_L(F)\mu_B m_F B,$$

and depends linearly on the magnitude of the magnetic field. It is therefore obvious that atoms with $m_F > 0$ will be attracted to minima in the magnetic field magnitude.

Because there are no photons present, magnetic trapping does not limit the temperature and density of the atoms like optical trapping and cooling. The spatial distribution of atoms in the trap is determined by their energy distribution, and this provides a measure of atomic temperature. Magnetic traps have a reasonably shallow potential depth, and only atoms with a low kinetic energy can be trapped. Due to the advent of laser cooling, a cold source of atoms could be obtained and used to load magnetic traps; greatly increasing their efficiency.

Cold neutrons were magnetically trapped in 1978, but the first successful neutral atom trap was created by Migdall *et al.* [48] in 1985. They loaded their magnetic trap using sodium atoms from a laser-cooled atomic beam.

1.1.6   Evaporative Cooling

Evaporative cooling is a term used to describe processes which 'lowers the lid' of a trapping potential, allowing the more energetic, hotter atoms to escape. The higher end of the energy spectrum is truncated, and if the atoms in a trap have sufficiently high density then collisions between the atoms rethermalise the energy distribution. The new energy distribution is a Boltzmann distribution with the mean energy of the truncated distribution. By continuously removing the higher energy atoms, a sample of magnetically trapped atoms can be cooled orders of magnitude below its initial temperature.

One technique used very successfully is radio frequency, RF, induced evaporation, otherwise known as an RF scalpel due to the spatial precision with which it can be used to remove high-energy atoms [19], [54].

1.1.7   Bose-Einstein Condensation

An important application of laser cooling is its role in the production of Bose-Einstein condensates, BECs. In 1924 Bose and Einstein predicted that below a certain temperature, a gas of non-interacting bosonic atoms (i.e. atoms with integral spin) will suddenly develop a macroscopic population in the lowest energy quantum mechanical state [2]. This property manifests itself when the atoms are cold enough and dense enough that the distance between atoms is approximately their de Broglie wavelength.

This condition on temperature and density can be more readily expressed as a restriction on the dimensionless phase space density,

$$\rho = n\Lambda^3,$$

where n is the number density of an atom sample, and Λ is the thermal de Broglie wavelength of the atoms. When ρ increases past 2.612, a phase transition occurs which creates BEC.

Although superfluid helium and superconducting metals exhibit some features of macroscopic quantum states, the strong interactions between the atoms in liquids and solids mask the underlying properties of the small percentage of quantum matter obtained. It is for this reason that BEC was sought in a gas.

The first observation of BEC in an atomic vapour was by Anderson *et al.* in 1995 [2]. They relied on the combination of a variety of techniques to reach the required phase space density. Firstly they used a 'dark' MOT, to provide a large number of cold atoms. The atoms were then compressed by adjusting the magnetic field of the MOT, and cooled using sub-Doppler techniques.

The resulting cold, dense sample of atoms was ideal for loading a magnetic trap. Because magnetic traps are relatively shallow, loading them with a cold source is very important, which is why the atoms were prepared by laser-cooling before trapping. Once the atoms are loaded into a magnetic trap, the cooling lasers can be turned off, and there are no longer any restrictions on the temperature or density of the atoms in the trap. Evaporative cooling techniques could then be applied, to increase the phase space density of the atoms past the value required for condensation.

Two condensates have been observed to date, and were obtained by Anderson *et al.* using ^{87}Rb [2] and K. B. Davis *et al.* with ^{23}Na [20]. Although the BECs were formed by different techniques, the condensates were both prepared using a sequence of optical trapping and/or cooling, magnetic trapping and evaporative cooling.

Once the first BECs were obtained, intensive studies of their properties began, as well as work in the realms of coherent matter, 'atom lasers' and other concepts which have previously been theorised on, but are only now within reach of experimentalists.

1.2 Thesis Outline

The laser group at Otago University entered the field of laser cooling in 1991, when Dr. Ann-Marie Oien commenced production of a background-loaded sodium MOT [50]. The MOT formed an integral part of Dr. Oien's PhD thesis and became operational in late 1993. Although sub-Doppler temperatures approaching 70μK were observed in this static MOT, sodium temperatures of $\approx 25\mu$K were obtained by Kasevich *et al.* [38] [39] using time-dependent cooling parameters.

The cooling process of Kasevich *et al.* initially involved the formation of a stable MOT, enabling the collection of a large number of atoms (atoms cannot be collected in molasses). Immediately after the atoms were collected, the MOT's magnetic field was removed, and the laser intensity was decreased. Removing the magnetic field eliminates the position-dependent trapping force on the atoms, turning the MOT into the 'optical molasses' of Chu *et al.* [10]. The atoms can then diffuse from the laser intersection region. The advantage of releasing the atoms is that, when the laser intensity and magnetic field are low, a strong, sub-Doppler cooling force acts on the atoms. This force induces low temperatures, at the cost of confinement. The slow molasses expansion also leads to a method for determining temperature parameters in the atomic cloud.

A description of the mechanisms involved in the sub-Doppler forces will be given in chapter 4, and the experimental techniques, used in an attempt to reproduce the results of Kasevich *et al.*, will be given in chapter 5.

Theoretical studies were carried out concurrently with the experimental investigations. The focus of the theoretical research was initially on Doppler theory (chapters 2, 3) including descriptions which can be adapted to either Doppler or sub-Doppler theory. Sub-Doppler processes were considered in chapter 5.

Chapter 2 deals with the atomic position and velocity distributions in MOTs and molasses, as predicted by Doppler theory. The analytic MOT distributions of Gajda *et. al* [27] are generalised. Considerations of intensity and/or frequency imbalances in counterpropagating laser beams are also implemented, further generalising the MOT and molasses distributions. An investigation into the 'launching' of atoms is made, and the chapter concludes with the description of a Doppler Monte Carlo simulation. The simulation accuracy is verified by comparison with earlier analytic results.

Chapter 3 considered the addition of complications in the MOT structure. The reradiative and absorptive forces [65], omitted in chapter 2, are included in the formalism. The non-conservative nature of the absorptive force leads to results which appear to contradict the findings of Sesko *et al.* [65], and also raises questions about the relatively widespread rule that the density in a MOT has a maximum value [65], [74].

The second half of chapter 3 studies the theory behind ring structures in a MOT. A review of existing theories is followed by new postulates; the new theory is then compared with that of refs. [65], [7], [29], [3]. The comparison implicates the necessity for inclusion of the reradiative and absorptive forces in models of certain ring structures.

As well as a brief description of existing sub-Doppler theories, chapter 4 studies the properties of various laser standing wave polarisation configurations, focussing in particular on the Sisyphus parameter 'p' of Steane and Foot [71]. The variance of p, is used to compare different configurations, for a variety of relative laser phases.

Chapter 2

Doppler Theory

2.1 Introduction

Two theoretical models of a MOT will be investigated—an analytic model and a Monte Carlo, or MC simulation. Analytic models are extremely fast in the sense that the solution is obtained 'instantaneously' after entering the parameters. The solution is only valid under certain, usually quite stringent, conditions however. The MC method is a lot more versatile, and can deal with situations where analytic solutions either don't exist or are extremely difficult to obtain. The drawback of a MC is that large amounts of CPU time are often required before a well-resolved result can be obtained.

This chapter will begin with a look at the analytic theory, studying cases with Cartesian or spherical symmetry, before using the MC to check the validity of the analytic models. The following chapter will deal with regimes where analytic models break down: rings and other structures in a MOT.

2.2 Analytic Theory

2.2.1 The Starting Blocks

In the introduction, the force on an atom due to the light from a single laser was considered (equation 1.4). In Doppler theory, the force on an atom due to several lasers is considered to be the superposition of the forces from each individual laser. This is not entirely correct, as when two or more light waves of the same frequency are superposed they form a standing wave, with a spatially modulated intensity. This leads to new physics, which will be considered in chapter 4, however the Doppler approximation is valid under some circumstances and gives a basic physical picture of laser cooling processes.

In order to apply equation 1.4, it is first necessary to determine ω and ω_0 for an atom moving in a magnetic field. An atom containing four energy levels will be considered, comprising an $F = 0$, $m_F = 0$ ground state and $F' = 1$, $m_{F'} = -1, 0, 1$ excited states. In the presence of a magnetic field, the degenerate $F' = 1$ energy is perturbed by the Zeeman effect into three non-degenerate energy levels differing from the original energy level by $\Delta\omega = m_{F'}\omega_B B$, where B is the magnitude of the local magnetic field vector, $\mathbf{B}$. Thus $\omega_0 + m_{F'}\omega_B B$ can be substituted for ω_0 in equation 1.4, and the Doppler-shifted laser frequency $\omega_L - \mathbf{k}_L \cdot \mathbf{v}$ can be substituted for ω. This leads to the relation $\omega - \omega_0 = \Delta - \mathbf{k}_L \cdot \mathbf{v} - m_{F'}\omega_B B$.

If laser light is circularly polarised and $\mathbf{B}$ is parallel (or antiparallel) to $\mathbf{k}_L$, the light will only excite transitions to either the $m_{F'} = -1$ or the $m_{F'} = +1$ excited states, depending on the helicity of the light and the value of $\mathbf{k}_L \cdot \mathbf{B}$. If the two vectors are not parallel, then the light will excite all three possible transitions.

Consider a point in space, (x, y, z), where the magnetic field is $\mathbf{B}$, and circularly polarised light is incident with wavevector $\mathbf{k}_L$. At (x, y, z) the tip of the light's electric field vector $\mathbf{E}$ will be tracing out a circle of radius E_0 in the plane perpendicular to $\mathbf{k}_L$. If viewed along the direction of $\mathbf{B}$, an ellipse with

semi-major axis E_0 and semi-minor axis $E_0 \cos\theta$ is observed, where θ is the angle between the $\mathbf{k}_L$ and $\mathbf{B}$ vectors. The $\mathbf{E}$ field has a component along the $\mathbf{B}$ axis with amplitude $E_0 \sin\theta$ and the elliptically polarised projection of $\mathbf{E}$ in the plane perpendicular to $\mathbf{B}$ is the superposition of two circularly polarised electric field vectors with opposite helicity and amplitudes $E_0 \frac{1+\cos\theta}{2}$, $E_0 \frac{1-\cos\theta}{2}$.

The circularly polarised light with intensity $I_0 = c\epsilon_0 E_0{}^2$ can therefore be decomposed into light which excites the $m'_F = 0$ transition ($I_\pi = c\epsilon_0 E_0{}^2 \sin^2\theta$) and light which excites the $m_{F'} = \pm 1$ transitions ($I_{\sigma+} = c\epsilon_0 E_0{}^2 (\frac{1+\cos\theta}{2})^2$ and $I_{\sigma-} = c\epsilon_0 E_0{}^2 (\frac{1-\cos\theta}{2})^2$). Note that $I_0 = I_{\sigma-} + I_\pi + I_{\sigma+}$ and that the labels σ^+ and σ^- will interchange, depending on the helicity of the light about $\mathbf{B}$.

Consider a laser beam propagating in the $+x$ direction, i.e. $\mathbf{k}_L = k_L \mathbf{i}$, in a spherical quadrupole magnetic field, $\mathbf{B} = b(x, y, -2z)$. The force felt by an atom within a laser beam of (low) intensity I_0 is given by a modified equation 1.4:

$$\mathbf{F} = \frac{\hbar k_L \Gamma \mathbf{i}}{2} \left(\frac{I_{\sigma-}/I_S}{1 + (\frac{2}{\Gamma})^2(\Delta - k_L v_x + \omega_B B)^2} + \frac{I_\pi/I_S}{1 + (\frac{2}{\Gamma})^2(\Delta - k_L v_x)^2} + \frac{I_{\sigma+}/I_S}{1 + (\frac{2}{\Gamma})^2(\Delta - k_L v_x - \omega_B B)^2} \right).$$
(2.1)

In an $F = 0 \to F' = 1$ system, the three possible energy transitions have the same Clebsch-Gordan coefficients—and therefore the same saturation intensities.

Following a method similar to those in refs. [43], [72], the next step will be to assume that $(k_L|v_x|$ & $\omega_B B) << (\Gamma$ & $\Delta)$, enabling a Taylor expansion of the force to first order:

$$F_x \approx \frac{\hbar k_L \Gamma}{2} \left(\frac{I_{\sigma-}}{I_S}(K - C(-k_L v_x + \omega_B B)) + \frac{I_\pi}{I_S}(K - C(-k_L v_x)) + \frac{I_{\sigma+}}{I_S}(K - C(-k_L v_x - \omega_B B)) \right),$$
(2.2)

where $K = \frac{1}{1+(2\Delta/\Gamma)^2}$ and $C = 8\Delta(\frac{K}{\Gamma})^2$. A better test for the validity of the Taylor expansion is the requirement $k_L|v_x|$, $\omega_B B << K/|C|$. Equation 2.2 can be simplified to:

$$F_x \approx \frac{\hbar k_L \Gamma}{2} \left(\frac{I_0}{I_S}(K + Ck_L v_x) + C\omega_B B \frac{I_{\sigma+} - I_{\sigma-}}{I_S} \right).$$

The expressions for $I_{\sigma-}$, $I_{\sigma-}$ show that: $B\frac{I_{\sigma+} - I_{\sigma-}}{I_S} = \pm \frac{I_0}{I_S} B\cos\theta$ (the sign depends on the helicity of the light relative to $\mathbf{B}$). Substituting $B\cos\theta = bx$ yields:

$$F_x \approx \frac{\hbar k_L \Gamma}{2} \frac{I_0}{I_S}(K + C(k_L v_x \pm \omega_B bx)),$$
(2.3)

and the helicity of the laser light is always chosen to obtain a force of the form:

$$F_x \approx \frac{\hbar k_L \Gamma}{2} \frac{I_0}{I_S}(K + C(k_L v_x + \omega_B bx)),$$
(2.4)

for reasons that will become apparent shortly. Points to note are:

- The force is linearly proportional to intensity.

- K is unaffected by a sign change in Δ, and Γ is always positive.

- C changes sign with Δ.

It can be similarly shown that the force experienced by an atom due to a laser propagating in the $-x$ direction is:

$$F_x \approx -\frac{\hbar k_L \Gamma}{2} \frac{I_0}{I_S}(K - C(k_L v_x + \omega_B bx)).$$

If two laser beams, with the same frequency (and therefore detuning), counterpropagate in the $\pm x$ directions and simultaneously interact with an atom, they create a force:

$$F_x \approx \frac{\hbar k_L \Gamma}{2} \left(\frac{I_{x+} - I_{x-}}{I_S} K + \frac{I_{x+} + I_{x-}}{I_S} C(k_L v_x + \omega_B bx) \right),$$
(2.5)

where the intensities of the $\pm x$ directed laser beams are $I_{x\pm}$, and standing wave effects are neglected. Lasers with intensities $I_{x+} = I_{x-} = I_x$ lead to a force $F_x \approx \hbar k_L \Gamma \frac{I_x}{I_S} C(k_L v_x + \omega_B bx)$.

The elements of this force are relatively familiar in Physics. A force that is linear in velocity provides a frictional or damping force if the constant of linearity, the damping constant, is negative—a positive damping constant creates a heating force. A force that is linear in position provides a trapping force if its constant of linearity, or spring constant, is negative. If a superposition of a damping and trapping forces are provided, then atoms can be cooled and trapped. This occurs precisely when C is negative—i.e. by choosing lasers that are detuned below the atomic transition ($\Delta < 0$).

By including four more laser beams in the $\pm y$ and $\pm z$ directions, all with detuning Δ, it is possible to create the force:

$$\mathbf{F} \approx \hbar k_L \Gamma \frac{C}{I_S} \left(I_x(k_L v_x + \omega_B b x), I_y(k_L v_y + \omega_B b y), I_z(k_L v_z + 2\omega_B b z) \right), \tag{2.6}$$

and provide three-dimensional cooling and confinement to a gas of atoms. The intensities I_y and I_z correspond to the $\pm y$ and $\pm z$ lasers respectively.

2.2.2 Saturation

As yet, only low intensity laser beams have been dealt with. When an atom is in an intense laser field the transition rate to the upper state increases. A two-level atom, subject to low intensity light from a single laser, absorbs photons at the approximate rate given in equation 1.3. The rate of photon absorption from a single laser when atoms are subject to more intense light is given by equation 1.2. The intensity term in the denominator ensures that there is never more than half of the atomic population in the excited state, due to an increased upper level stimulated emission rate when the light intensity increases. In the low intensity regime stimulated emission effects can be neglected.

With the added complication of two or more laser beams incident on an atom, there does not appear to be any precise way of including the effects of saturation in the absorption rates—two approximations can be used however [43], [28], [29], [65], [74]. One approximation assumes that only one of $2N$ laser beams is close enough to resonance for saturation to occur. The absorption rate from beam $i \in \{0, 1, ..., 2N\}$ is then:

$$R_i = \frac{\Gamma}{2} \frac{I_i/I_S}{1 + I_i/I_S + (\frac{2}{\Gamma})^2(\omega_i - \omega_{0_i})^2}.$$

Saturation may occur when several of the beams are resonant however, and a better approximation for the absorption rate from individual beams is then:

$$R_i = \frac{\Gamma}{2} \frac{I_i/I_S}{1 + I_{tot}/I_S + (\frac{2}{\Gamma})^2(\omega_i - \omega_{0_i})^2},$$

where $I_{tot} = \sum_{i=1}^{2N} I_i$. This regime ensures the total absorption rate from all beams, $\sum_{i=1}^{2N} R_i$, has the upper bound:

$$\sum_{i=1}^{2N} R_i \leq R_{max} = \frac{\Gamma}{2} \frac{I_{tot}/I_S}{1 + I_{tot}/I_S} \leq \frac{\Gamma}{2},$$

and the upper state population cannot exceed 50%. The second method of including saturation is advocated widely in the literature and will be adopted throughout this thesis.

The MOT of the previous subsection had $2N = 6$ lasers with total intensity $I_{tot} = 2(I_x + I_y + I_z)$. By including the I_{tot}/I_S term in the denominator of previous Taylor expansions (cf. equation 2.2), expressions that include the approximate effects of saturation in a MOT can be obtained. The following variable substitutions will correct for saturation:

$$K \rightarrow K_{tot} = \frac{1}{1 + I_{tot}/I_S + (2\Delta/\Gamma)^2},$$

$$C \rightarrow C_{tot} = 8\Delta \left(\frac{K_{tot}}{\Gamma}\right)^2. \tag{2.7}$$

11

2.2.3 Heating and Distribution of Atoms in a MOT

So far, only the average effect of the light force has been considered. Atoms solely governed by the force described in equation 2.6 oscillate about $\mathbf{r} = \mathbf{0}$ with exponentially decaying velocity and displacement amplitudes. As an atom tends to lower velocities however, the recoil impulses due to the random process of spontaneous emission create a non-negligible disturbance. Spontaneous effects prompt atoms into 'random walks' through velocity space—i.e. they create a heating mechanism which counteracts the cooling force. Equilibrium is reached when the heating and cooling forces balance.

Consider an atom acted on by two laser beams, of equal intensity and frequency, which counterpropagate along the x axis. If the velocity of the atom is low, then equation 2.4 and the relation $\mathbf{F} = \hbar \mathbf{k} R$, can be used to find the rate of absorption from each beam: $R \approx \frac{\Gamma}{2} \frac{I_x}{I_S} K$. The total absorption rate is twice this figure. Note that the atom is equally likely to absorb a photon from either beam—regardless of which laser it last absorbed a photon from. The atom can therefore occasionally receive several impulses in the same direction.

Ignoring spontaneous emission and the damping force, let the atom have initial velocity $v_x = 0$. The two laser beams will create a force along the x-axis only: the atom's x-velocity alone will change. With every photon absorption, the atom's x-velocity alters by $\Delta v_x = \pm(\hbar k_L/m = p/m = \Delta v)$, where p is the magnitude of a photon's momentum. There is an equal probability of a $+$ or $-$ change in velocity, as the damping force is ignored and so the rate of absorption is not velocity dependent. The impulses will occur at a rate $R \approx \Gamma \frac{I_x}{I_S} K$.

At $t = 0$ the probability that $v_x = 0$ is 1. At $t = 1/R$ the relative probability that the atom has $v_x = +\Delta v$ is 1, and the relative probability that the atom has $v_x = -\Delta v$ is 1 also (all other velocity groups have zero probability). Continuing in this vein, for $t = n/R$ and $n \in \{0, 1, 2, ...\}$, a relative probability table similar to Pascal's triangle can be found:

n	t	Relative probability that atom has x-velocity v_x (units of Δv) at time t								
		$v_x = -4$	$v_x = -3$	$v_x = -2$	$v_x = -1$	$v_x = 0$	$v_x = 1$	$v_x = 2$	$v_x = 3$	$v_x = 4$
0	0	0	0	0	0	1	0	0	0	0
1	1/R	0	0	0	1	0	1	0	0	0
2	2/R	0	0	1	0	2	0	1	0	0
3	3/R	0	1	0	3	0	3	0	1	0
4	4/R	1	0	4	0	6	0	4	0	1

If the time is $t = n/R$, then the possible velocities the atom can have are $v_x = (n - 2k)\Delta v$ for $k = 0 \to n$ in integer steps of k. The relative probability that the atom has $v_x = (n - 2k)\Delta v$ is given by $\binom{n}{k}$ Now since $\sum_{k=0}^{n} \binom{n}{k} = 2^n$, the probability that an atom has $v_x = (n - 2k)\Delta v$ is $\binom{n}{k}/2^n$. Note that this is a binomial distribution, and that as n increases, the binomial distribution will tend to a normal, i.e. Gaussian, distribution of velocities.

The average value of $v_x{}^2$ at time $t = n/R$ is given by the sum of the products of probability and squared velocity over all possible velocities:

$$\overline{v_x{}^2} = (\Delta v)^2 \sum_{k=0}^{n} \frac{\binom{n}{k}(n - 2k)^2}{2^n} = n(\Delta v)^2$$

(the second equality can be proved by induction). Substituting $t = n/R$, the expectation value of $v_x{}^2$ can be found as a function of time:

$$\overline{v_x{}^2(t)} = (\Delta v)^2 Rt. \tag{2.8}$$

The discussion so far has neglected spontaneous emission. As well as receiving impulses from the x lasers due to absorption, an atom also recoils after every spontaneous emission. If spontaneous emission

is restricted to one dimension, the x-axis, it is clear that including spontaneous emission leads solely to a factor of two increase in the absorption rate of equation 2.8.

Laser cooling can be compared to the problem of an atom with mass m, subject to a 1D force of the form:

$$F_x = ma_x = -\alpha_x v_x - \beta_x x + F_{H_x}(t),\tag{2.9}$$

where α_x is the friction constant, β_x is the spring constant and $F_{H_x}(t)$ is a fluctuating heating force that acts in the x direction and has a direction which averages to zero over time. The probability an atom, subject to this force, has x co-ordinate between x and $x + dx$, and x velocity between v_x and $v_x + dv_x$ is $P(x, v_x)\, dx\, dv_x$, where

$$P(x, v_x) = A_x e^{\frac{-\beta_x x^2}{2k_B T_x}} e^{\frac{-m v_x^2}{2k_B T_x}},\tag{2.10}$$

$$A_x = \frac{1}{2\pi k_B T_x}\sqrt{m\beta_x},$$

and T_x is the x-'temperature' of a sample of atoms [59], [60].

The value of $\overline{v_x^2(t)}$ for a particle subject to the force $F_{H_x}(t)$ alone is given by:

$$\overline{v_x^2(t)} = \frac{2k_B T_x \alpha_x}{m^2}t,$$

and comparison with equation 2.8 leads to the relation:

$$T_x = \frac{R(\Delta v)^2}{2k_B \alpha_x}.\tag{2.11}$$

The total rate of absorption and emission (both contribute to heating) in a 1D trap is given by $R \approx 2\Gamma \frac{I_x}{I_S}K$ and from equation 2.5 it can be deduced that $\alpha_x \approx \hbar k_L^2 \Gamma \frac{I_x}{I_S}C$, thus:

$$T_x = \frac{-\hbar K}{k_B C} = -\hbar\Gamma\frac{1 + (2\Delta/\Gamma)^2}{8k_B \Delta/\Gamma} = T_D.\tag{2.12}$$

This is the Doppler temperature, T_D, mentioned in the first chapter. The minus sign does not indicate a negative temperature, as cooling exists only when $\Delta < 0$. It can be shown that the Doppler temperature has a minimum value of $T_D = \hbar\Gamma/(2k_B)$ when $2\Delta/\Gamma = -1$. If saturation effects are included (i.e. using K_{tot}, C_{tot} from equation 2.7) the Doppler temperature is given by:

$$T_D = -\hbar\Gamma\frac{1 + I_{tot}/I_S + (2\Delta/\Gamma)^2}{8k_B \Delta/\Gamma}.\tag{2.13}$$

Equation 2.12 gives an approximate formula for the 1D temperature of atoms subject to a force solely in the x-direction. However, in a more realistic 3D setting spontaneous emission will have a distribution of directions. Suppose that instead of spontaneously emitting along the laser beam axis, atoms emitted photons isotropically. The probability an atom receives an impulse in the $+x$ or $-x$ direction is equally likely, however the magnitude of the impulse along the x direction is distributed continuously between 0 and Δv.

The rate at which $\overline{v_x^2(t)}$ increased in equation 2.8 was proportional to the photon absorption rate multiplied by p_x^2, where p_x was the magnitude of the photon's momentum in the x direction. Suppose several of these processes, with different rates of absorption for different p_x^2 values, were superposed. It can be shown that equation 2.8 is then modified to

$$\overline{v_x^2(t)} = \overline{p_x^2 R}\frac{t}{m^2},\tag{2.14}$$

where $\overline{p_x^2 R}$ is the expectation value of photons' p_x^2 magnitudes, weighted by their absorption rates. A brief explanation of equation 2.14 can be found in appendix B and the equation will now be used to derive various temperatures.

An earlier result in the subsection was that lasers along the x axis cause an atom to absorb and emit photons at a total rate $R_{tot} \approx 2\Gamma\frac{I_x}{I_S}K$. This will be of use in solving equation 2.14. It is now only necessary to work out the value of $\overline{p_x^2 R}$.

The absorption of photons has a contribution to $\overline{p_x^2 R}$ of $\left(\frac{\hbar k_L}{m}\right)^2 R_{tot}/2$. The factor of 1/2 arises because absorption processes only occur at half the rate of R_{tot}. The contribution to $\overline{p_x^2 R}$ from spontaneous emission must now be found. If an atom emits a photon with momentum magnitude $p = \hbar k_L$, then $|\mathbf{p}|^2 = p_x^2 + p_y^2 + p_z^2 = \hbar^2 k_L^2$. If the emission is isotropic, then $\overline{p_x^2} = \overline{p_y^2} = \overline{p_z^2} = \hbar^2 k_L^2/3$. The contribution from emission to $\overline{p_x^2}$ is thus

$$\frac{1}{6}\left(\frac{\hbar k_L}{m}\right)^2.$$

If spontaneously emitted photons, excited by circularly polarised x laser beams, are emitted in a dipole radiation pattern, then it can be shown (see appendix A) that

$$(\overline{p_x^2}, \overline{p_y^2}, \overline{p_z^2}) = \hbar^2 k_L^2(2/5, 3/10, 3/10),$$

and hence the contribution from emission to $\overline{p_x^2 R}$ would be

$$\frac{1}{5}\left(\frac{\hbar k_L}{m}\right)^2 R_{tot}.$$

The one-dimensional temperature for a system of atoms acted on by two laser beams is thus (using equation 2.14 to find the temperature, as before):

$$T_x = \frac{2}{3}T_D$$

for isotropic spontaneous emission and

$$T_x = \frac{7}{10}T_D$$

if dipole emission is considered instead.

The other four lasers will now be included in the analysis, providing confinement in all three dimensions.

Six laser beams, propagating along the $\pm x, \pm y, \pm z$ directions are considered here. Counterpropagating beams on the x_i axis have equal intensities I_{x_i}. The forces acting on an atom in the x direction are the cooling and trapping forces produced by the two x beams. These forces provide the values of α_x and β_x, the x direction damping and spring constants, respectively. The heating force in the x direction has several contributions: the absorption process from the x-beams, as well as spontaneous emissions subsequent to the absorption of light from any one of the six laser beams.

The heating rate due to absorption from the x beams is $R \approx \Gamma\frac{I_x}{I_S}K$ as before. Absorptions from the y and z beams don't affect atoms' x velocity, or x position, and so do not contribute to heating in the x direction. The spontaneous emissions from these beams *will* contribute to the heating force however, with $\overline{p_x^2 R}$ for the processes given by either

$$\left(\frac{\hbar k_L}{m}\right)^2 \Gamma\frac{I_{y/z}}{3I_S}K,$$

for isotropic emissions or

$$\left(\frac{\hbar k_L}{m}\right)^2 \Gamma\frac{3I_{y/z}}{10I_S}K,$$

for dipole emissions.

In this model the fluctuating heating force of equation 2.9 depends on absorption and spontaneous emission, which have no spatial dependence. This is because, if an atoms' velocity and displacement are low, the heating force depends solely on the intensities in the laser beams—which are assumed to have a constant intensity profile over all space. The 1D separability of the problem arose because the x_i force on an atom depends solely on its x_i component of position and velocity. Thus the different x_i probability distributions are independent and can be worked out separately.

The value of the x temperature is given by the modified version of equation 2.11

$$T_x = m^2 \frac{\overline{p_x^2 R}}{2k_B \alpha_x}. \tag{2.15}$$

Thus for isotropic spontaneous emission, the x temperature is:

$$T_x = T_D \left(\frac{4I_x + I_y + I_z}{6I_x} \right)$$

and for dipole emissions,

$$T_x = T_D \left(\frac{14I_x + 3I_y + 3I_z}{20I_x} \right). \tag{2.16}$$

The 'temperature' in the y and z directions can be obtained using the above formula and permuting (x, y, z). The coefficients T_{x_i} are not the temperature in the sense of statistical physics [27], as here the temperature of the system is not isotropic.

The spring constants β_{x_i} can be found using equation 2.6, and are given by:

$$\beta_{x_i} = -(1 + \delta_z^{x_i})\hbar k_L \omega_B b \frac{8I_x \Delta}{I_S \Gamma} \left(\frac{1}{1 + (2\Delta/\Gamma)^2} \right)^2. \tag{2.17}$$

(the different form of β_z is a result of the magnetic field $\mathbf{B} = b(x, y, -2z)$). The probability distributions (equation 2.10) for each direction can now be deduced, by substitution of the correct temperatures and spring constants. Approximate saturation effects can be included in the parameters above if T_D of equation 2.13 ($I_{tot} = 2(I_x + I_y + I_z)$) is used, as well as the equation

$$\beta_x = -\hbar k_L \omega_B b \frac{8I_x \Delta}{I_S \Gamma} \left(\frac{1}{1 + I_{tot}/I_S + (2\Delta/\Gamma)^2} \right)^2$$

and its parallels.

Because the x, y, and z distributions are independent, the probability of finding an atom in the MOT with x co-ordinate between x and $x + dx$, y co-ordinate between y and $y + dy$, z co-ordinate between z and $z + dz$, x velocity between v_x and $v_x + dv_x$, y velocity between v_y and $v_y + dv_y$ and z velocity between v_z and $v_z + dv_z$ is:

$$P(x, y, z, v_x, v_y, v_z)\, dx\, dy\, dz\, dv_x\, dv_y\, dv_z$$

where

$$P(x, y, z, v_x, v_y, v_z) = A_x\, A_y\, A_z\, e^{\frac{-\beta_x x^2}{2k_B T_x}}\, e^{\frac{-\beta_y y^2}{2k_B T_y}}\, e^{\frac{-\beta_z z^2}{2k_B T_z}}\, e^{\frac{-m v_x^2}{2k_B T_x}}\, e^{\frac{-m v_y^2}{2k_B T_y}}\, e^{\frac{-m v_z^2}{2k_B T_z}}. \tag{2.18}$$

The 'temperatures' and spring constants in the above distribution generalise the results of Gajda and Mostowski [27]. The above model reduces to that of Gajda and Mostowski in ref. [27] if the following simplifications are made: the x and y laser beams have equal intensity, the saturation term is neglected and only the dipole, i.e. most realistic, spontaneous emission scenario is considered. The method used here has invoked the separability of the three dimensions of a Doppler theory MOT, in order to simplify a 3D problem into three 1D problems. The method in ref. [27] uses a three dimensional Wigner functions to solve the MOT equations in 3D.

2.2.4   Doppler Molasses

In the previous subsections, the Doppler theory of a MOT was considered—six circularly polarised beams in a magnetic field. Many experiments have also been performed using linearly polarised laser beams, and/or with no magnetic field. Turning off the magnetic field greatly simplifies the forces, as the substitution $B = 0$ in equation 2.1 reduces the three position-dependent force terms into a single velocity-dependent, spatially invariant term. Optical molasses is a term used to describe lasers which provide solely a damping, rather than trapping, force. Removing the magnetic field therefore creates molasses. This subsection will deal with the behaviour of atoms in molasses, as predicted by Doppler theory. The atomic position distribution

in molasses is largely determined by the loading process, and thus only the velocity distribution can be calculated in general. Loading is necessary as atoms are lost from the laser beam intersection via Brownian motion.

The full $B = 0$ form of equation 2.1, neglecting saturation, is:

$$\mathbf{F} = \frac{\hbar k_L \Gamma \mathbf{i}}{2} \left(\frac{(I_{\sigma-} + I_\pi + I_{\sigma+})/I_S}{1 + (\frac{2}{\Gamma})^2(\Delta - k_L v_x)^2} \right), \tag{2.19}$$

which depends only on velocity and $I = I_{\sigma-} + I_\pi + I_{\sigma+}$, where I is the total laser intensity in the $+x$ beam, independent of the laser's polarisation.

The average force on an atom in molasses, and the heating rate due to absorption can be found exactly the same way as in a MOT, since position dependence has no bearing on damping or temperature. The damping constants are independent of laser polarisation, as are the heating processes from absorption— however heating rates from spontaneous emission have a polarisation dependence.

The average momentum squared components of photons emitted by spontaneous emission have been calculated for both circular and linearly polarised light in appendix A. For the linearly polarised case, e.g laser light propagating along the x direction and polarised along the z axis, the momenta of emitted photons obey:

$$(\overline{p_x^2}, \overline{p_y^2}, \overline{p_x^2}) = \hbar^2 k_L^2 (2/5, 2/5, 1/5).$$

This final piece of information allows atomic temperatures can be found.

Suppose the beam pairs counter-propagating along the (x, y, z) axes are polarised in the (y, z, x) directions. The temperatures induced in the atoms are (cf. equation 2.16):

$$T_x = T_D \left(\frac{7I_x + 2I_y + I_z}{10I_x} \right),$$

$$T_y = T_D \left(\frac{7I_y + 2I_z + I_x}{10I_y} \right),$$

$$T_z = T_D \left(\frac{7I_z + 2I_x + I_y}{10I_z} \right).$$

Note that unless the intensities of the beams are carefully chosen, the predicted distribution is non-thermal and in fact the formulae above yield an isotropic temperature only when all laser intensities are equal. Shevy *et al.* [68] carried out tests to see if the velocity distribution in such a beam arrangement was isotropic. In ref. [68] it was stated that there are solutions to the optical Bloch equations (OBEs) which lead to non-thermal distributions, although a physical reason for such distributions was lacking. This description perhaps provides one, and predicts that if the x, y and z beams have different intensities (relative beam intensities are omitted by Shevy *et al.*) then isotropic velocity distributions will not be expected, due to the anisotropy in damping and heating forces.

The experiment in ref. [68] focused primarily on the z temperature of atoms in the laser configuration of the previous paragraph. This temperature was also measured when (a) one of the horizontal (x or y) beams was adjusted to be polarised parallel to the z beam, and (b) in a configuration where the two horizontal beams had parallel polarisations. The z temperatures, predicted by Doppler theory, for arrangements (a) and (b) are:

$$T_z = T_D \left(\frac{7I_z + I_x + I_y}{10I_z} \right) \quad \text{((a) if the } x \text{ beam is polarised parallel to the } z\text{),}$$

$$T_z = T_D \left(\frac{7I_z + 2I_x + 2I_y}{10I_z} \right) \quad \text{((a) if the } y \text{ beam is polarised parallel to the } z\text{),}$$

$$T_z = T_D \left(\frac{7I_z + I_x + I_y}{10I_z} \right) \quad \text{((b) if the } x \text{ beam is polarised parallel to the } y\text{),}$$

$$T_z = T_D \left(\frac{7I_z + 2I_x + 2I_y}{10I_z} \right) \quad \text{((b) if the } y \text{ beam is polarised parallel to the } x\text{).}$$

In ref. [68] bimodal velocity distributions were observed, and it was postulated that the separate velocity distributions were governed by Doppler processes in the hotter distribution, and sub-Doppler mechanisms in the cooler collection. When Shevy *et al.*, changed the beam configuration to (a), the colder distribution of atoms became hotter (by a factor of ≈ 2) although the hotter atoms stayed at about the same temperature. Changing the configuration to (b) made the colder atoms slightly hotter and no results were taken from the fast atoms.

If the beams along each co-ordinate axis were of equal intensity, then changing the system to configuration (a) or (b) would lead to temperature changes of $\pm 10\%$ according to Doppler theory. Although this does not quantitatively explain the observations in ref. [68], most of their observations were of the colder (sub-Doppler) atoms. The Doppler theory does give some physical insight into the effects of changing beam polarisation and intensity on the diffusion mechanisms however. Diffusion has a similar effect on the temperature of both Doppler and sub-Doppler atomic populations (the damping forces are markedly different however). Reinvestigation of the bimodal distributions, with emphasis on the hot atoms would provide a quantitative check of the hot distributions and the predictions of Doppler Theory.

The temperature derivations given in this section can be extended to other laser configurations, using the same techniques. The polarisations of all six laser beams could be chosen independently as long as counterpropagating beams had equal intensity.

As well as various optical molasses configurations there is also a variant version of a MOT consisting of three beams of circularly polarised light balanced by counterpropagating linearly polarised beams. Calculations can also be done for this MOT, as with the molasses configurations. Such configurations are numerous, but easily derived and therefore omitted.

2.2.5   Approximation Validity

The linear expansion for the light pressure force was given in the paragraph of equation 2.2, and relied on the relation:

$$k_L |v_{x_i}|, \ \omega_B B << K/|C|. \tag{2.20}$$

As the position and velocity distributions have now been derived, their consistency with the inequality of equation 2.20 can be checked.

Given a probability distribution $P(w) = e^{-cw^2/2}$, for some variable w and constant c, it is easy to show that the root mean square (rms) value of w is:

$$w_{rms} = \sqrt{\overline{w^2}} = 1/\sqrt{c}. \tag{2.21}$$

Comparison with equation 2.18 yields:

$$(v_{x_i})_{rms} = \sqrt{k_B T_{x_i}/m}, \qquad (x_i)_{rms} = \sqrt{k_B T_{x_i}/(m\beta_{x_i})}.$$

Since $B = b\sqrt{x^2 + y^2 + 4z^2}$, a typical value of B in the MOT is given by $B_{rms} \approx 2.5b\sqrt{k_B T/(m\beta)}$ where T and β are the average temperature and spring constant for the trap, respectively. Substituting this expression for B, and using $\sqrt{k_B T/m}$ as a typical $|v_{x_i}|$ value, the conditions in equation 2.20 can be rewritten as:

$$k_L \sqrt{k_B T/m}, \ 2.5b\sqrt{k_B T/(m\beta)} << K/|C|.$$

A reasonable value for T is T_D, and (cf. equation 2.17) β can be approximated:

$$\beta = -\hbar k_L \omega_B b \frac{8I\Delta}{I_S \Gamma} \left(\frac{1}{1 + (2\Delta/\Gamma)^2} \right)^2,$$

where I is the average beam intensity. Using the relation $K/|C| = k_B T_D/\hbar$, it can be shown that the analytic theory satisfies these conditions when:

$$k_L << \sqrt{k_B T_D m}/\hbar \approx 7 \times 10^9 \sqrt{T_D},$$

17

$$2.5\sqrt{\frac{\omega_B b(1+(2\Delta/\Gamma)^2)I_S}{\Gamma k_L I}} << 35 \quad (\text{or} \quad (I/I_S) >> b(1+(2\Delta/\Gamma)^2)/1200)$$

for sodium.

Sodium has $k_L \approx 10^7 \mathrm{rad\,m^{-1}}$, and the minimum Doppler temperature is $240\mu K$ so the condition on velocity reduces to $10^7 << 10^8$. This inequality is satisfied to some extent, but could still be a possible source of small disagreements ($\approx 1\%$) between a complete solution and the linear approximation.

Most MOTs have $b \approx 10^{-1} \mathrm{T/m}$. The inequality in b can therefore be considered as a lower bound on I: $(I/I_S) >> 2 \times 10^{-4}$, when $2\Delta/\Gamma = -1$. Intensities in this range can easily be achieved using a dye laser. The probability distributions were derived for the case $(I/I_S) < 1$, restricting the intensity to a finite range if the analytic results are to be used.

Another point to check is the use of continuous equations to model atoms whose motions are dictated by discrete energy quanta. The necessary requirements for continuous theory are that $dx_i << (x_i)_{rms}$ and $dv_{x_i} << (v_{x_i})_{rms}$, where dx_i and dv_{x_i} are the typical position and velocity changes during a photon absorption cycle. Using previous expressions, as well as the equations $dx_i \approx (v_{x_i})_{rms}/R$ (where $R \approx I/I_S\Gamma$ is the photon absorption rate) and $dv_{x_i} \approx \hbar k_L/m$, it can be shown that:

$$dv_{x_i} << (v_{x_i})_{rms} \quad \text{reduces to the earlier condition} \quad k_L|v_{x_i}| << K/|C|,$$

$$\text{and} \quad dx_i << (x_i)_{rms} \quad \text{reduces to} \quad I/I_S >> 10^{-6}b,$$

which is an even stricter version of the earlier condition on I/I_S.

Thus it seems that the analytic solution for a MOT should be valid as long the condition:

$$b(1+(2\Delta/\Gamma)^2)/1200 << (I/I_S) < 1$$

is satisfied. Other discussions of the necessary approximations can be found in refs. [43], [27].

2.2.6 Intensity Imbalances and Frequency Mismatching in Molasses

The theory thus far has only dealt with cases where the intensities of counterpropagating beams were equal—imbalanced intensities will now be considered. Atoms are still cooled, in the sense of having a narrow velocity distribution, but the mean atomic velocity is non-zero. An understanding of how this velocity varies with intensity imbalance can be useful for launching atoms, or error estimations (in reality counterpropagating molasses beams will always be imbalanced to some extent).

When acted on by a laser in the $\pm x$ direction with intensity $I_{x\pm}$, the average force felt by an atom in molasses is:

$$\mathbf{F}_{x\pm} = \pm\frac{\hbar k_L\Gamma\mathbf{i}}{2}\left(\frac{I_{x\pm}/I_S}{1+(\frac{2}{\Gamma})^2(\Delta \mp k_Lv_x)^2}\right). \tag{2.22}$$

Only the x laser beams contribute to the x average force, although the y and z beams contribute to the x temperature.

Suppose that a change of velocity co-ordinate is made: let $v_x = v_x' + v_{x_0}$ where v_x' is the modified velocity and v_{x_0} is a constant. The force an atom experiences in this new reference frame is the same as in the original frame ($F(v_x) = m\frac{dv_x}{dt} = m\frac{dv_x'}{dt} = F'(v_x')$). If v_x' is small, then the forces in equation 2.22 have Taylor expansions, as seen earlier in the chapter. The force from the beam travelling in the $+x$ direction can be written:

$$F_{x+} = \frac{\hbar k_L\Gamma}{2}\left(\frac{I_{x+}/I_S}{1+(\frac{2}{\Gamma})^2(\Delta^+ - k_Lv_x')^2}\right),$$

where $\Delta^+ = \Delta - k_Lv_{x_0}$. The first order Taylor expansion of the force is therefore:

$$F_{x+} \approx \frac{\hbar k_L\Gamma}{2}\frac{I_{x+}}{I_S}(K^+ + C^+k_Lv_x'), \tag{2.23}$$

where $K^+ = \frac{1}{1+(2\Delta^+/\Gamma)^2}$ and $C^+ = 8\Delta^+(\frac{K^+}{\Gamma})^2$.

Similarly, the force from the beam travelling in the $-x$ direction is:

$$F_{x^-} \approx -\frac{\hbar k_L \Gamma}{2} \frac{I_{x-}}{I_S} (K^- - C^- k_L v_x'),$$

where $\Delta^- = \Delta + k_L v_{x_0}$, $K^- = \frac{1}{1+(2\Delta^-/\Gamma)^2}$ and $C^- = 8\Delta^-(\frac{K^-}{\Gamma})^2$. The net force in the x direction is given by:

$$F_x \approx \frac{\hbar k_L \Gamma}{2 I_S} \left((I_{x+} K^+ - I_{x-} K^-) + (I_{x+} C^+ + I_{x-} C^-) k_L v_x' \right). \tag{2.24}$$

If the force on an object depends on the velocity of the object, $F = F(v)$, then (as in this case) it may be possible for the object to accelerate to a velocity v_0 where $F(v_0) = 0$—i.e. the object can reach and maintain an equilibrium velocity, v_0. The constant v_{x_0} is chosen so that, in the new velocity frame, no average force is felt by atoms in the x direction, when $v_x' = 0$. It is therefore necessary for the constant term in the equation 2.24 to be set to zero, i.e.:

$$I_{x+} K^+ = I_{x-} K^-. \tag{2.25}$$

In the new frame the atoms will have a narrow distribution of atomic velocities centred on $v_x' = 0$, and so the Taylor expansion of equation 2.23 was valid. Equation 2.25 leads to a quadratic in v_{x_0}, with variables Γ, Δ, and $i_x = I_{x+}/I_{x-}$ (the intensity ratio):

$$v_{x_0} = \frac{-\Delta(i_x+1)}{k_L(i_x-1)} \left(1 \pm \sqrt{1 - (\Gamma/(2\Delta))^2 + 1) \frac{(i_x-1)^2}{(i_x+1)^2}} \right). \tag{2.26}$$

The v_{x_0} velocity with the $-$ sign before the squareroot will be considered from now on, as the other velocity leads to a heating force.

If the intensity imbalance of the laser is small, $i_x \approx 1$, then equation 2.26 can be approximated to the form:

$$v_{x_0} = \frac{-\Gamma(i_x-1)\left(1+(2\Delta/\gamma)^2\right)}{16 k_L \Delta/\Gamma}, \tag{2.27}$$

which is precisely the drift velocity obtained in refs. [28] and [43], except these papers include a saturation term. Such a term could have been included in the preceding equations, but was omitted for brevity (see full expressions later).

After the equilibrium velocity is calculated, the x-direction's heating term, damping constant (see equation 2.9) and 'temperature' T_x' can be found in the new frame. The parameter T_x' is a measure of the spread of x-velocities around the mean velocity, v_{x_0}, whereas a normal temperature tends to refer to atomic distributions with zero mean velocity. The form of T_x', ignoring heating from the y and z laser beams, is:

$$T_x' = \frac{-7\hbar}{5 k_B} \left(\frac{i_x K^+ + K^-}{i_x C^+ + C^-} \right), \tag{2.28}$$

which reduces to the 1D Doppler theory temperature when $i_x = 1 \Leftrightarrow v_{x_0} = 0$. Note that it is relatively easy to include the effects of the four y and z laser beams in the analytic calculations, and that they only effect T_x', not v_{x_0}.

Figures 2.1, 2.2 illustrate the variables derived in equations 2.26, 2.28. Note that the 'temperature', T_x', has a minimum at imbalance $i_x = 1$ for detunings $\Delta/\Gamma \approx> -1$, and has a maximum at $i_x = 1$ for detunings $\Delta/\Gamma \approx< -1$. It is also possible to set up configurations, with large detunings and high intensity imbalances, that lead to high mean velocities (hundreds of metres per second) yet low 'temperatures', of about twice the minimum Doppler temperature. An example is shown in figure 2.3.

Large intensity ratios are difficult to achieve experimentally, however, if a reasonably high absorption rate is maintained. The laser with the higher intensity would have to be extremely intense, and the (low intensity) Doppler theory then breaks down. With a low absorption rate the atoms are slow to accelerate to their equilibrium velocity and this means a large laser interaction volume is required for acceleration.
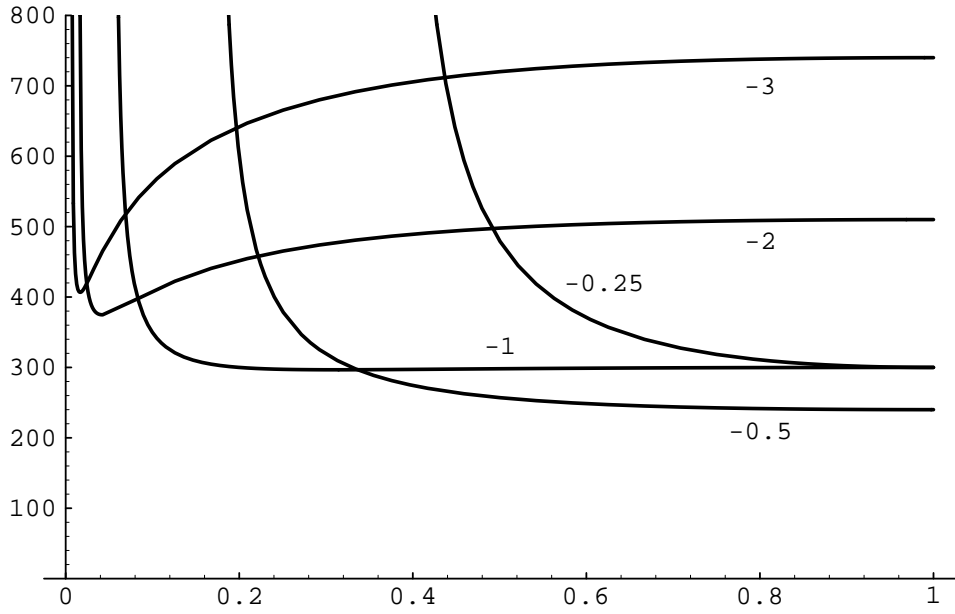
Figure 2.1: One-dimensional 'Temperature', $T_x'(\mu K)$, of Doppler molasses atoms versus intensity ratio, i_x, of the x laser beams. The labels for each curve denote the associated detuning in units of Γ.
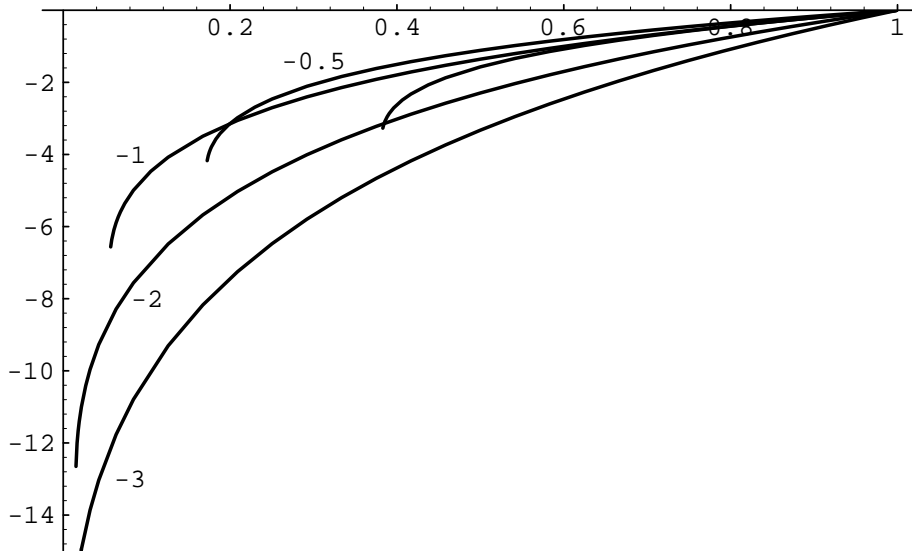

Figure 2.2: Mean velocity, v_{x_0}, of Doppler molasses atoms versus intensity ratio, i_x, of the x laser beams. The labels for each curve denote the detuning in units of Γ. The linear approximation for v_{x_0} corresponds to tangents of the curves at $i_x = 1$.
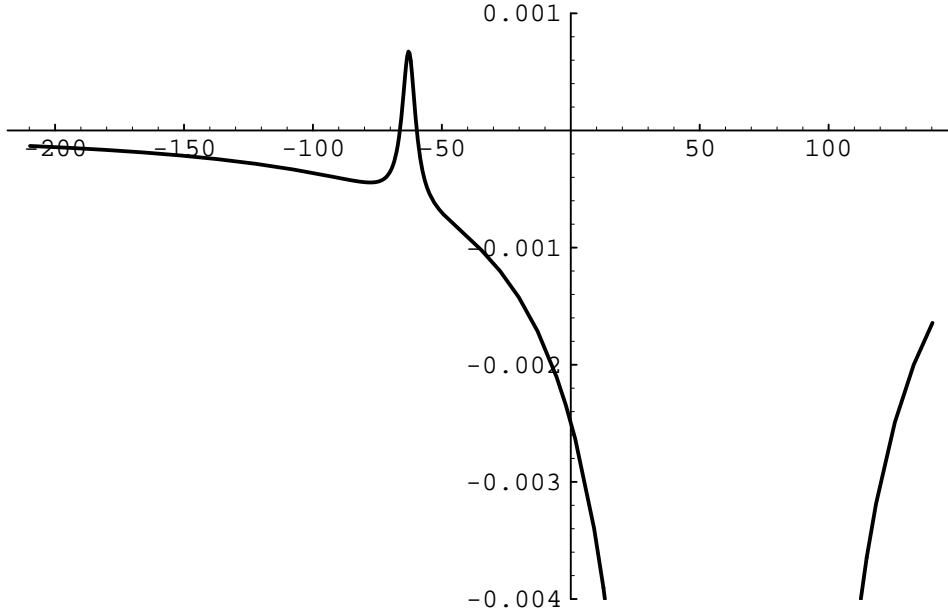
Figure 2.3: The net average force, F_x, versus velocity, $v_x(\mathrm{ms}^{-1})$, for atoms in molasses laser light with detunings $\Delta = -10\Gamma$, and intensity ratio $i_x = 0.0013$. The equilibrium velocity is $v_{x_0} = -60\mathrm{ms}^{-1}$.

A velocity probability distribution similar to equation 2.18 is easily obtained for six laser beams with independent intensities. This distribution has the form given in equation 2.30 and its main difference from intensity-balanced molasses is the non-zero mean atomic velocity, $(v_{x_0}, v_{y_0}, v_{z_0})$. The majority of 3D results can be inferred from the 1D theory however, and thus only this case was considered in detail.

Previously, only counterpropagating beams with the same detuning, Δ, have been considered. This is because the six laser beams used in experimental cooling are often obtained from the same laser, via mirrors and beamsplitters. Many of the problems in launching atoms with a high intensity imbalance can be eliminated if counterpropagating laser beams have similar intensities, but different detunings. This can be achieved using two separate lasers, or using Acousto-Optic Modulators (AOMs) to independently alter the frequency of laser beams picked off from a single laser.

Suppose counterpropagating lasers have equal intensity I, and the detuning of the beam travelling in the $\pm x$ direction is $\Delta_\pm$. The lasers will create the forces:

$$F_{x\pm} = \pm\frac{\hbar k_L \Gamma}{2} \left(\frac{I/I_S}{1 + (\frac{2}{\Gamma})^2 (\Delta_\pm \mp k_L v_x)^2} \right).$$

The total force from the laser beams is zero when $\Delta_+ - k_L v_x = \Delta_- + k_L v_x$, or:

$$v_x = (\Delta_+ - \Delta_-)/(2k_L) = v_{x_0}. \tag{2.29}$$

It can also be shown that atoms travelling at the equilibrium velocity, v_{x_0}, observe both laser beams to be detuned by $\overline{\Delta} = (\Delta_+ + \Delta_-)/2$ and this average detuning can be used instead of the detuning in equation 2.12 to find the one-dimensional Doppler 'temperature' of the atoms.

If counterpropagating laser beams have the same frequency and intensity, a standing wave is created and the atoms are cooled by sub-Doppler processes in the light potential of the standing wave. If the lasers have different frequencies then a 'standing wave' is still formed, but only in the velocity-shifted frame where the atoms observe both frequencies to be the same. This occurs precisely when the atoms' velocities reach the value given in equation 2.29, and therefore both Doppler and sub-Doppler theory predict that asymmetrically detuned lasers will accelerate atoms to the velocity given in equation 2.29.

Whether the Doppler or sub-Doppler 'temperature' is observed will depend on the intensity of the light, and the average detuning of the laser beams.
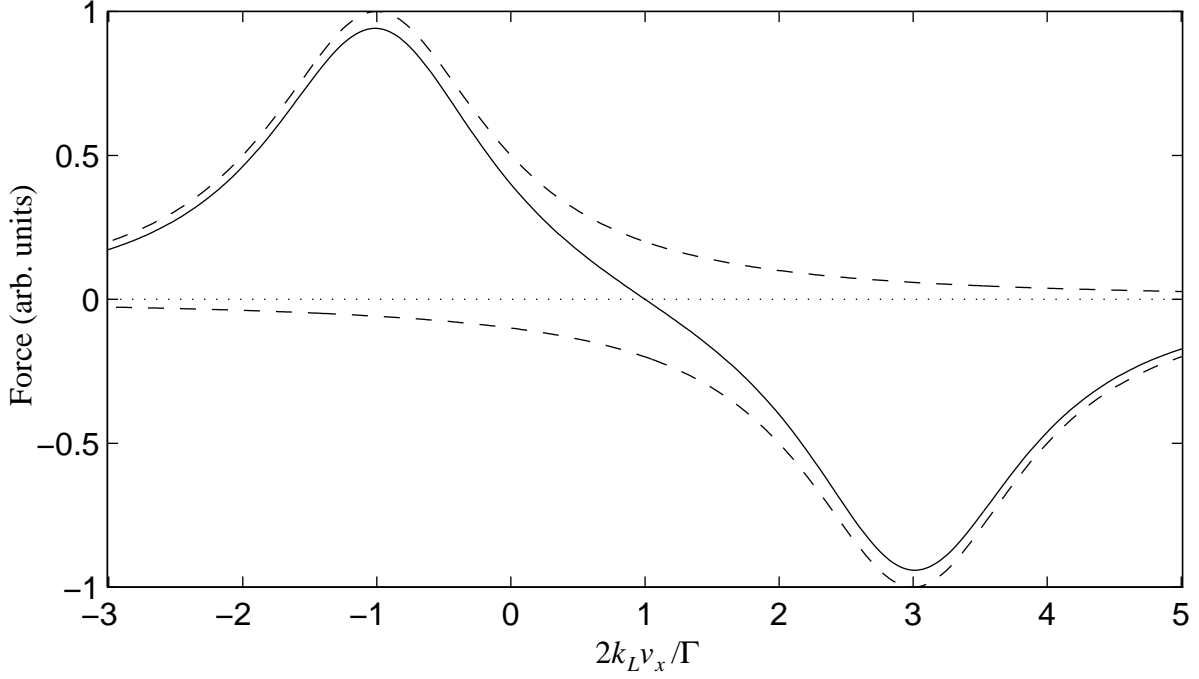
21

Figure 2.4: Total force, F_x, versus x-velocity for molasses atoms in counterpropagating lasers with detunings $\Delta_+ = -\Gamma/2$ and $\Delta_- = -3\Gamma/2$ (solid curve). The dashed curves correspond to the individual laser forces $F_{x\pm}$. The equilibrium velocity is $v_{x_0} = (\Delta_+ - \Delta_-)/(2k_L) = \Gamma/(2k_L)$.

The 3D analytic velocity distribution of equation 2.18 can in fact be generalised still further to allow the six laser beams to have entirely independent intensities and detunings. Saturation effects can also be included. The distributions all have the form:

$$P(v_x, v_y, v_z) = A\, e^{\frac{-m(v_x - v_{x_0})^{\,2}}{2k_B T_x{}'}}\, e^{\frac{-m(v_y - v_{y_0})^{\,2}}{2k_B T_y{}'}}\, e^{\frac{-m(v_z - v_{z_0})^{\,2}}{2k_B T_z{}'}}, \tag{2.30}$$

and their validity can be checked using the method of subsection 2.2.5.

The generalised equilibrium velocities in equation 2.30 for six lasers in the $\pm x_i$ directions, with intensities $I_{x_i\pm}$ and detunings $\Delta_{x_i\pm}$, can be obtained by the following formula:

$$v_{x_0} = \frac{-b - \sqrt{b^2 - 4ac}}{2ak_L}, \tag{2.31}$$

where $a = (i_x - 1)$, $b = 2(i_x\Delta_{x-} + \Delta_{x+})$, $c = (i_x - 1)(1 + I_{tot}/I_S)\Gamma^2/4 + i_x\Delta_{x-}{}^2 - \Delta_{x+}{}^2$ and $i_x = I_{x+}/I_{x-}$. The y and z velocities can be found by substituting these co-ordinates into the equation instead of x. The equation 2.31 was formed using equation 2.25 where the variables $K^\pm$ were generalised to:

$$K_{x\pm} = \frac{1}{1 + I_{tot}/I_S + (\Delta_{x\pm} \mp k_L v_{x_0})^2 4/\Gamma^2}.$$

Equation 2.31 reduces to equation 2.26 when $\Delta_{x-} = \Delta_{x+} = \Delta$. The x-'temperature' of the atoms (permute co-ordinates to obtain $T_y{}'$, $T_z{}'$) is given by:

$$T_x{}' = \frac{-\hbar}{10k_B} \frac{14I_{x+}K_{x+} + 3I_{y+}K_{y+} + I_{z+}K_{z+}}{I_{x+}C_{x+} + I_{x-}C_{x-}},$$

where $C_{x\pm} = 8\Delta(K_{x\pm}/\Gamma)^2$. The 'temperature' here corresponds to six circularly polarised laser beams—the 'temperature' of other polarisation configurations is similar.

The cooling of atoms, with *constant* laser parameters, to a *constant* velocity has been dealt with so far. It is also possible, however, to start with a given atomic velocity distribution, then ramp the equilibrium

velocity (equation 2.29) by altering the laser detunings. A large number of atoms can be accumulated in a MOT configuration, where the average velocity of the atoms is zero, and the atoms are trapped as well as cooled. A MOT therefore provides a good source of atoms to accelerate—the trapped atoms can be released into optical molasses, and then the detunings of the lasers can be ramped. The velocity of the atoms can thus be continuously ramped from zero to another velocity, whilst still maintaining a high number of 'cold' atoms.

A relatively short ramp time is necessary, to slow the expansion of the atomic cloud in molasses, yet the frequency ramp cannot be so fast that the atoms will stop interacting with the lasers. The (one-dimensional) damping force on the atoms can be approximated by:

$$F = -\alpha(v - v_0(t)),$$ \hfill (2.32)

where α is the friction co-efficient of the laser force and $v_0(t)$ is the equilibrium velocity of the force, defined by the detunings, as a function of time. The damping parameter α only remains constant if the average detuning, $\overline{\Delta}$, is held constant. Another feature of the force is that, in both Doppler and sub-Doppler regimes, it will only be linear in a region $|v - v_0| \leq v_{max}$. The parameters α, v_{max} can be obtained by Doppler or sub-Doppler theory depending on which is more appropriate.

The atoms have initial velocity $v(0) = 0$ and are subject to the differential equation 2.32, or:

$$\frac{dv}{dt} + \gamma v = \gamma v_0(t),$$ \hfill (2.33)

where $\gamma = \alpha/m$. The solution to this differential equation is:

$$v(t) = \frac{\gamma \int_0^t v_0(u) \exp(\gamma u) du}{\exp(\gamma t)}.$$ \hfill (2.34)

If a linear velocity ramp $v_0(t) = \kappa t$ is applied, this leads to the solution $v(t) = \kappa t - \kappa/\gamma$—i.e. the atoms' velocities lag behind the steady-state equilibrium velocity by κ/γ. The laser damping forces become non-linear, and in fact weaker, when $\kappa/\gamma > v_{max}$. It is therefore important that the velocity ramp is chosen with $\kappa < v_{max}\alpha/m$. The limiting rate at which atomic velocities can be ramped is thus determined by the value of $v_{max}\alpha$ held by the dominant cooling force. Doppler forces have a higher v_{max}, and a lower α than sub-Doppler forces: it is not immediately clear which of these configurations will lead to the best acceleration constant, κ.

The parameter v_{max} can be approximated by the turning points of the force vs. velocity curves (cf. figure 1.1 for Doppler $F(v)$, ref. [17] for sub-Doppler $F(v)$). An analytic estimate for α is given by F_{max}/v_{max}, where F_{max} is the force at velocity v_{max}. A quick estimate of the mechanism with the most rapid acceleration is therefore given directly by $v_{max}\alpha/m = F_{max}/m$. Doppler forces lead to the highest values of F_{max}, and will thus allow the most rapid velocity ramping to occur. Using Doppler forces to accelerate the atoms will also give the atoms a high 'temperature' however, and many experimenters apply sub-Doppler cooling (with the same equilibrium velocity as the Doppler stage) at the final ramp velocity. The sub-Doppler cooling compresses the velocity distribution after its initial 'hot' acceleration.

Atoms prepared in this manner can be launched, with variable average speed, toward atomic mirrors composed of evanescent light fields, or spatially varying magnetic fields [23], [61], [39].

2.2.7 Intensity Imbalances in a MOT

In the previous subsection the forces involved only Cartesian components of velocity, and consisted of a single term for each laser. In a MOT, the forces are position dependent, and the force from each laser has three components: from π and $\sigma^{\pm}$ light (equation 2.1). The position dependence of the detuning in the forces does not develop through linear Cartesian terms, like the velocity dependence, and in fact depends on $B \propto \sqrt{x^2 + y^2 + 4z^2}$. It was onlypossible to find an analytic distribution for a MOT due to the fortuitous occurrence that, to first order, the force depends on the Cartesian co-ordinates, instead of B (equation 2.3).

Unlike molasses, where the atoms accelerate to a non-zero velocity, the spring constant in a MOT stops the atoms from drifting under an intensity imbalance. Instead the imbalance causes the position of the trap to shift. An approximate value for the equilibrium position of the trap can be made using the linear Taylor expansion theory, as long as the equilibrium position is consistent with the Taylor expansion. The x-component of the average force in a MOT can be approximated by an equation similar to equation 2.3:

$$F_x \approx \frac{\hbar k_L \Gamma I_{x-}}{2} \left(\frac{i_x - 1}{I_S} K + \frac{i_x + 1}{I_S} C(k_L v_x + \omega_B bx) \right), \qquad (2.35)$$

where $i_x = I_{x+}/I_{x-}$, and K, C were defined for equation 2.2. Saturation effects can be included, if required, but the force will always be of the form $F_x = a - bv_x - cx$ (a, b, c, constant). The stable point for a one-dimensional force of the form $F_x(v_x, x)$ is when $F_x = 0$ and $v_x = 0$. Thus the stable point of the present force is $x_0 = a/c$. It is clear that if the co-ordinate transformation $x \to x' + x_0$ is made, with x_0 a constant, then the forces in the x' and x frames are equivalent, $F'(v_{x'}, x') = F(v_x, x)$, and the net force felt by an atom with $v_x = 0$ at $x = x_0$ is zero.

The force in equation 2.35 has its equilibrium position at the point:

$$x_0 = -\frac{(i_x - 1)K}{(i_x + 1)C\omega_B}. \qquad (2.36)$$

This is slightly more general than the result of Steane *et al.* [71], as saturation terms, and intensity imbalances in more than one beam pair, can be included. The equilibrium positions y_0 and z_0 have the same form as equation 2.36 except z_0 has a factor of two in the denominator, due to the stronger z magnetic field gradient. In this first order approximation, the equilibrium x_i co-ordinate in the MOT depends solely on the intensity imbalance in the x_i laser beams . The equilibrium position is independent of intensity—it is only affected by the intensity *ratio*.

In a similar process to that which was covered in the molasses subsection, the temperatures and spring constants in an imbalanced MOT can be found as a function of the trap parameters. The form of the atomic probability distribution is:

$$P(x, y, z, v_x, v_y, v_z) \propto e^{\frac{-\beta_x (x - x_0)^2}{2k_B T_x}} \, e^{\frac{-\beta_y (y - y_0)^2}{2k_B T_y}} \, e^{\frac{-\beta_z (z - z_0)^2}{2k_B T_z}} \, e^{\frac{-m v_x^2}{2k_B T_x}} \, e^{\frac{-m v_y^2}{2k_B T_y}} \, e^{\frac{-m v_z^2}{2k_B T_z}},$$

where the variables are easily deduced and have been omitted for brevity. The temperatures have a dependence on trap parameters similar to that seen in the 'temperatures' of the molasses subsection. Note that the mean velocity of the atoms is zero, and that six independent beam intensities can be used—further extending the results obtained in ref. [27].

If instead of trying to solve the equilibrium equations using a linear approximation, the full system of the three (component) equations:

$$\mathbf{F}(\mathbf{r}, \mathbf{v} = \mathbf{0}) = \mathbf{0},$$

is manipulated in the search for a solution, one obtains three equations in the variables x^2, y^2, z^2. Through substitution it is possible to obtain a single equation in one of these variables, and the resulting equation is a polynomial of order 10 in the variable x^2, say. The solution to such an equation cannot be found analytically, unlike the corresponding quadratic involved in Doppler molasses. Numerical solutions are possible, however, and should provide a better estimation of the equilibrium point in a MOT than the linear theory.

2.3 Monte Carlo

This section deals with the key features in a Monte Carlo (MC) computer simulation of atoms in a MOT. Doppler theory is used, which means the six laser beams are be considered separately and standing wave effects are ignored. The atomic transition considered is $F = 0$ to $F' = 1$ as in the analytic section—and several results from that section will be used here.

An 'Monte Carlo' simulation is typically used to describe a computer program which studies the complete time-evolution of one or several objects. The simulation used in this thesis considers atoms as non-interacting objects, subject to light pressure forces. The atoms move ballistically, until a photon is either (instantaneously) absorbed from the surrounding lasers, or emitted. The position and velocity co-ordinates of the atoms are sampled, yielding information about atomic temperatures and spatial distribution.

2.3.1   Absorption

In the previous section, equation 2.1 yielded the force from a laser beam travelling in the $+x$ direction, and the approximate effect of saturation can be made as in subsection 2.2.2. Force equations can also be obtained for the other five beams typically used in a MOT (a four-beam tetrahedral MOT is also possible). The absorption rates for each beam are similar to the forces.

One advantage of the MC approach is that, unlike most analytic theories, problems can be answered without reducing equations to first order, linear, approximations. The rate equations can be left as Lorentzian functions, and the beam intensities need not be position-independent. Gaussian beam intensities are used in the simulation, and the intensities used in the rate equations are modified accordingly.

Given the position and velocity of an atom, the absorption rates due to each of the six beams can be calculated using the equations mentioned above. These absorption rates can be summed to get the total absorption rate: $R_{tot} = \sum_{i=1}^{6} R_i$. The average time between atomic photon absorptions is thus $\tau = 1/R_{tot}$. In the MC, R_{tot} is evaluated after an atom has spontaneously emitted a photon. The atom is then allowed to travel ballistically for a time interval $\tau' = \tau - 1/\Gamma$, before the atom's position is updated $\mathbf{r} \rightarrow \mathbf{r} + \mathbf{v}\tau'$ and the atom absorbs a photon.

Before every photon absorption, the simulation must decide which laser beam an atom absorbs the photon from. The relative probability of photon absorption from a given laser beam varies. Thus after a time τ, the atom will absorb a photon from one of the six beams, with relative probability

$$R_1 : R_2 : R_3 : R_4 : R_5 : R_6$$

between the six beams. The laser beam from which the photon was absorbed can be randomly picked using a random number generator. Firstly a random number between 0 and 1 can be created. Multiplying this number by R_{tot} will give a random number (r, say) in the interval $i = [0, R_{tot}]$. The interval i can be split into six intervals:

$$[0, R_1), [R_1, R_1 + R2), [R_1 + R2, R_1 + R2 + R3), ..., [R_{tot} - R_6, R_{tot}],$$

with sizes determined by the relative absorption probability of their associated laser beam. The random number r will lie in one of the six intervals, and a photon is absorbed from the laser beam corresponding to that interval.

After photon absorption, the velocity of an atom is updated accordingly. The atom then follows a ballistic evolution (for one excited state lifetime $1/\Gamma$) before spontaneous emission occurs.

After one absorption-emission cycle the rates of photon absorption from each beam are recalculated, and the probable time until the next absorption (τ) is calculated as before. This process is then repeated for any specified number of absorption-emission cycles, and for any number of 'atoms' necessary. A linear increase in either of these parameters will result in a linear increase in CPU time.

2.3.2   Emission

Two spatial distributions for spontaneous emission have been used in the MC simulation—isotropic and dipole. Isotropic emission is when an atom emits a photon with equal probability of emission in all directions. The MC keeps track of the atom's Cartesian velocity components, and so in order to know the effect of spontaneous emission on the atom it is necessary to know the Cartesian momentum components of the

photon. The atom can be considered to be the point of origin of an emitted photon's momentum vector, and the vector tip can lie anywhere on a sphere about the atom. The radius of the sphere is the photon's magnitude. Randomly choosing a point on this sphere will obtain a spontaneous photon's momentum.

In order to emit photons isotropically through the surface of a sphere, a vector point on the sphere must have equal likelihood of lying in two different regions of the sphere, if these regions have equal area. Whatever co-ordinates system is chosen to describe the surface of the sphere, the random generation of co-ordinates must be weighted to coincide with the surface elements of that co-ordinate system.

Spherical polars will be used, $(\phi, \theta$ with θ the azimuthal angle) and the surface element on the sphere is therefore given by $dA = \sin\phi \, d\phi \, d\theta$. As the area element is linear in $d\theta$ it is clear that randomly choosing, with constant weighting, a real value in the interval $[0, 2\pi)$ will generate values of θ that are distributed symmetrically about the sphere's axis. For ϕ a number is required between 0 and π, with the relative weighting $\sin\phi$ of choosing the value ϕ. Computers only generate random numbers that are uniformly distributed between the upper and lower limit points, and so it is necessary to perform a few 'tricks' to obtain random values for ϕ.

Suppose there is a variable $p(\phi)$ such that $dp = f(\phi) \, d\phi$. The function p maps the interval $[\phi_{min}, \phi_{max})$ to the interval $[p(\phi_{min}), p(\phi_{max}))$ and as long as p is one:one then the inverse of p, p^{-1} can be found. Because of the way p is defined, then an interval of size dp in the range of p corresponds to an interval $d\phi$, weighted by $f(\phi)$, in the domain of p. Thus if random numbers are chosen, with uniform weighting, in the range $[p(\phi_{min}), p(\phi_{max}))$, and are then mapped into the domain $[\phi_{min}, \phi_{max})$ using p^{-1}, the resulting random ϕ values will be weighted according to $f(\phi)$.

Substituting $f(\phi) = \sin\phi$ leads to $p = \cos\phi$, if the constant of integration is set to zero. The domain of p is the interval $[0, \pi)$, on which p is one:one, and so its inverse is well-defined. Obtaining isotropic random ϕ co-ordinates can therefore be achieved by generating random numbers in the interval $[\cos(0) = 1, \cos(\pi) = -1)$, then taking their inverse cosine.

Now that randomly generated (ϕ, θ) co-ordinates for emitted photons' recoil momenta have been obtained, it remains to translate the co-ordinates into a Cartesian momentum vector:

$$\mathbf{p} = \hbar k (\sin\phi \cos\theta, \sin\phi \sin\theta, \cos\phi). \tag{2.37}$$

A similar procedure is followed in order to obtain the random distribution of photon momenta due to dipole emissions. Suppose a circularly polarised laser is propagating along the z direction and excites a $|\Delta m| = 1$ transition in an atom. The atom's dipole vector traces out a disc perpendicular to, and centred on, the z axis. It can be shown [15] that the relative flux of emitted photons through an area dA, at the sphere co-ordinates (ϕ, θ) is given by:

$$\text{Flux} \propto \frac{1}{2}(1 + \cos^2\phi) \, dA = \frac{1}{2}\sin\phi \, (1 + \cos^2\phi) \, d\phi \, d\theta.$$

Due to the symmetry of the problem θ can be randomly chosen as before, however a different technique will be necessary for generating ϕ co-ordinates. Here $dp_\sigma = \frac{1}{2}\sin\phi \, (1 + \cos^2\phi) \, d\phi$, therefore

$$dp_\sigma = \frac{5}{8}\sin\phi + \frac{1}{8}\sin 3\phi \, d\phi, \quad \text{and so}$$

$$p_\sigma = -\frac{5}{8}\cos\phi - \frac{1}{24}\cos 3\phi = -\cos\phi \, (3 + \cos^2\phi)/6.$$

Note that p_σ is a one:one function between the limits $p_\sigma(0) = -2/3$ and $p_\sigma(\pi) = 2/3$, and therefore its inverse is well-defined.

Because the function p_σ is a cubic in $\cos\phi$, the roots of p_σ can be solved analytically. Given any value of p_σ in the interval $[-2/3, 2/3)$ it is possible to invert the cubic to find the corresponding value of $\cos\phi$, and hence ϕ :

$$\cos\phi = -\sqrt[3]{-6p_\sigma + \sqrt{9p_\sigma^2 + 1}} - \sqrt[3]{-6p_\sigma - \sqrt{9p_\sigma^2 + 1}},$$

$$\phi = \cos^{-1}\left(-\sqrt[3]{-6p_\sigma + \sqrt{9p_\sigma{}^2 + 1}} - \sqrt[3]{-6p_\sigma - \sqrt{9p_\sigma{}^2 + 1}}\right).$$

This equation can then be used on random numbers between $-2/3$ and $2/3$ to obtain correctly weighted random ϕ co-ordinates for dipole spontaneous emissions.

Finally the dipole emission induced by a linearly polarised laser beam is considered. Suppose a laser beam is travelling with $\mathbf{k}$ perpendicular to the z axis and is polarised parallel to the z axis. It can excite a $|\Delta m| = 0$ transition in an atom, where the atom's dipole vector traces out a line segment on the z axis. In this case the corresponding results are:

$$\text{Flux} \propto \sin^2\phi \, dA = \sin^3\phi \, d\phi \, d\theta,$$

$$dp_\pi = \sin^3\phi = \frac{1}{4}(3\sin\phi - \sin 3\phi)\, d\phi,$$

$$p_\pi = (-9\cos\phi + \cos 3\phi)/12 = \cos\phi(-3 + \cos^2\phi)/3.$$

Like p_σ, p_π is one:one and can be written as a cubic in $\cos\phi$. If values for p_π are randomly chosen between $p_\pi(0) = -2/3$ and $p_\pi(\pi) = 2/3$, then random values for ϕ can be found through the formula:

$$\phi = \cos^{-1}\left(2\cos(\cos^{-1}(3p_\pi/2)/3 + 4\pi/3)\right).$$

Unlike the derivation of $p_\sigma{}^{-1}$, the inverse for p_π requires the use of complex algebra, and in particular De Moivre's theorem.

2.3.3 Sampling

Various techniques were used to study the evolution of the phase space (position and velocity) co-ordinates of atoms in the system. The main method of acquiring information about a system governed by statistical processes is through the ensemble and time averages of properties in the material under consideration. The Ergodic hypothesis [59] states that, for a system in equilibrium, the two averages yield the same result.

To obtain information through the time-averaging technique, a single atom was studied. Since the atoms in the MC system are considered to be non-interacting, all the required information can be obtained from this one atom—as long as the system under consideration consists of an isolated population. If separate populations exist, then the ensemble (several atom) average is required for the determination of relative population characteristics. The possibility of two distinct atomic populations is apparent in MOTs with a ring+ball configuration [7].

The symmetries involved in the trap determined which MOT parameters were the most informative. If the expected spatial probability distribution is separable, i.e. $P(x, y, z) = P_x(x)P_y(y)P_z(z)$ like in the analytic MOT description, then it makes sense to sample the x, y, and z co-ordinates independently. The sampling can be made by dividing the x co-ordinate (say) into several 'bins', or intervals. During the MC simulation the atom's x co-ordinate is sampled, and its corresponding bin is found. The relative probability of the bin is then increased by the amount of time the atom stayed in the bin. In this way a relative probability distribution for the atom's spatial and velocity distributions can be constructed.

In cases where the probability distribution isn't separable (e.g. in a ring setup) then other sampling techniques can be used. One method is to divide the (x, y) plane into square or rectangular bins, extending the 1D sampling technique. In this way a $P(x, y)$ distribution could be created. The disadvantage of this method is that a larger sampling time is necessary in order to acquire the same resolution as the separable probability distributions.

2.3.4 Random Numbers

The computer language used in the MC was C, because its speed was typically a factor of 100 faster than Matlab. The solution matrices created by the C code were saved to file in a form that Matlab could recognise, as the results could then be loaded into Matlab for analysis.

C's inbuilt random number generator created 'random' integers $rand() = 0 \rightarrow 32767$. Random numbers between 0 and 1 could be created using $rand()/32767$, but the MC needed random numbers that approximated a continuum—these random numbers were far too 'discrete'. Another major drawback of the generator was its periodicity (period 32768). Even if 'finer' random numbers of the form $(rand() \times 32768 + rand())/(32768^2 - 1)$ were used, these numbers would also be periodic, with a period close to 32767—i.e this would make no significant improvement.

For this reason random number programs from Numerical Recipes [57] were used: in particular the routines 'ran2' and 'ran4'. These had periodicities of $> 2 \times 10^{18}$ and were therefore quite adequate. An example of a typical MC computer file can be found in appendix C.

2.3.5 MC/Analytic Comparison

Balanced Intensities

After creating the MC, its consistency was checked by comparison with the analytic theory, before it was used for more complicated problems. The saturation terms I_{tot}/I_S were removed from the denominators of the rate equations for the purpose of the test (to be consistent with the analytic MOT theory).

The theoretical MOT system consisted of a field gradient, $b = 7G\text{cm}^{-1}$, beam intensities of $3I_{x\pm} = 2I_{y\pm} = I_{z\pm} = 0.3I_S$ and a detuning of $\Delta = -\Gamma/2$. All other parameters (k_L, Γ, m etc.) were set to values characteristic of Sodium atoms. The velocity and position of a single atom were sampled over 5×10^8 absorption/emission cycles. The cases of isotropic spontaneous emission, and dipole emission (consistent with circularly polarised laser beams) were both considered.

In equation 2.21 it was shown that a distribution $P(w) = e^{-cw^2/2}$ has $w_{rms} = 1/\sqrt{c}$. It is clear that a plot of $\ln P(w)$ vs. w^2 will be a straight line, with gradient $-c/2$. Thus if probability distributions like equation 2.18 are obtained by the MC, it is easy to find the 'c' of the exponents by fitting lines to the log plots, and thus find temperatures and rms positions for the atoms. Plots of the MC MOT probability distributions, using the parameters described above, are given in figures 2.5, 2.6, and a temperature derivation is illustrated in figure 2.7. A comparison of MC and analytic MOT atomic cloud properties is given in the following table (IE and DE denote isotropic and dipole spontaneous emission respectively).

	$T_x(\mu\text{K})$	$T_y(\mu\text{K})$	$T_z(\mu\text{K})$	$x_{rms}(\mu\text{m})$	$y_{rms}(\mu\text{m})$	$z_{rms}(\mu\text{m})$
Analytic, IE	360	240	200	84.7	48.9	25.8
Analytic, DE	348	240	204	83.3	48.9	26.0
MC, IE	363.1 ± 2.1	241.7 ± 0.7	201.7 ± 0.4	84.0 ± 2.7	49.2 ± 1.1	26.3 ± 0.7
MC, DE	350.0 ± 2.1	241.9 ± 0.9	206.1 ± 1.2	85.3 ± 2.9	48.6 ± 1.2	26.3 ± 0.6

The MC properties were the averaged results of five independent runs of the MC. The errors correspond to twice the standard deviation involved with each average. The position errors are greater, as a percentage, than the velocity errors because the damping force is much stronger than the restoring force, and so the time constant for velocity is much shorter than the equivalent time constant for position. For this reason the position probability distributions take longer to reach equilibrium.

Although the MC results are not in strict agreement with the analytic predictions, a margin of error was expected due to the approximations in the analytic theory discussed earlier. The two techniques are in quite close agreement however, and in particular the different effects of dipole and isotropic spontaneous emission are apparent in both descriptions.

Imbalanced Intensities

Another test for the Monte Carlo was to set up a simulation where the intensities were imbalanced, and compare the distribution with the result predicted by the analytic theory. The first simulation had no
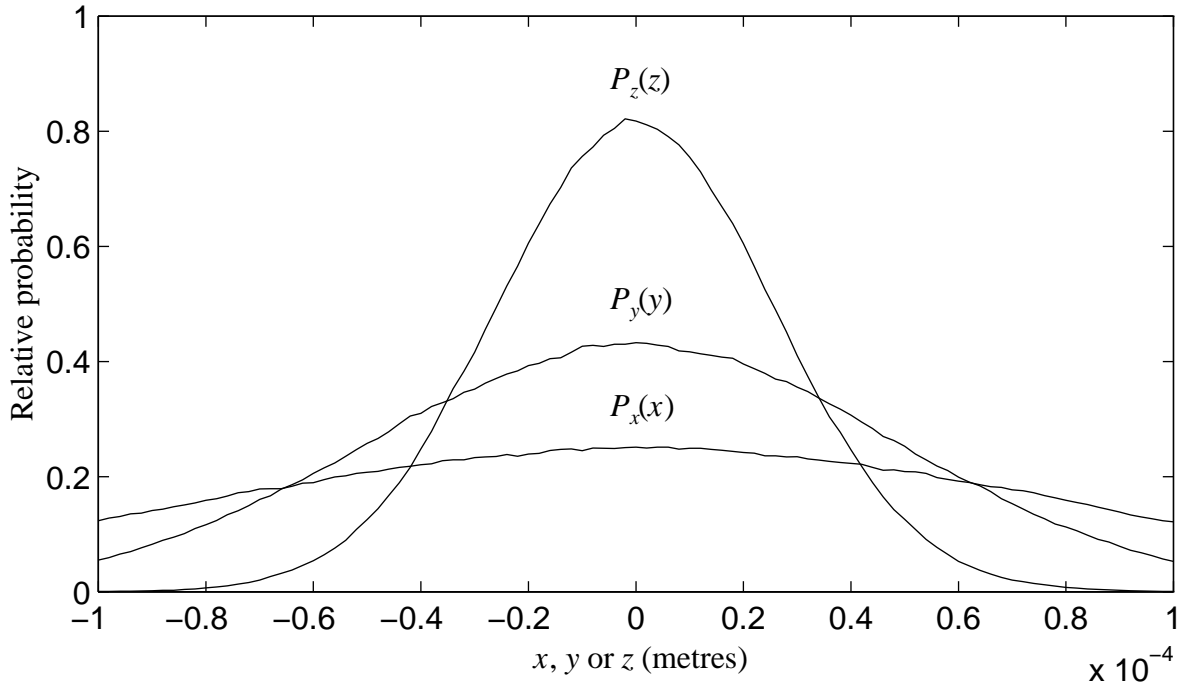
Figure 2.5: Position probability distributions for an MC MOT with isotropic emission: $P_{x_i}(x_i)\,dx_i$ is the relative probability of finding a particle with x_i position between x_i and $x_i + dx_i$.
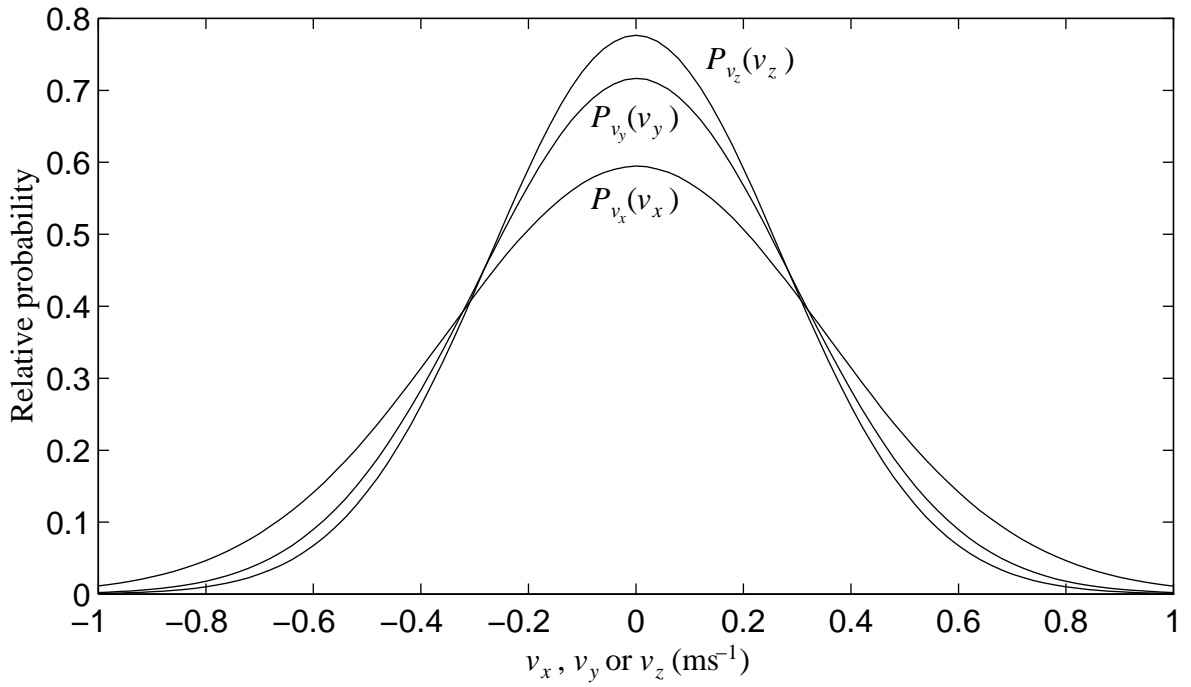

Figure 2.6: Velocity probability distributions for an MC MOT with dipole emission. These are defined in a similar manner to the position distributions.
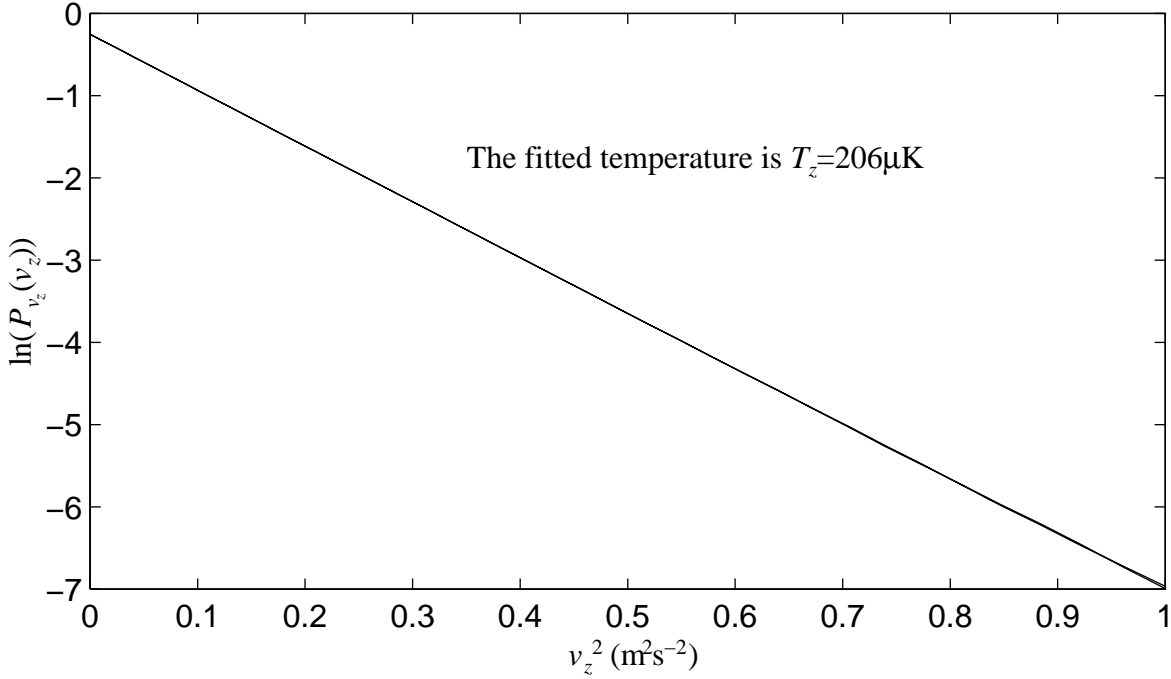
Figure 2.7: $\ln(P_{v_z}(v_z))$ vs. $v_z{}^2$ for an MC MOT with dipole emission: the gradient of the fitted line determines the z 'temperature' of the Gaussian distribution.

magnetic field (i.e. Doppler molasses), and the laser intensities (expressed as fractions of the saturation intensity) were: $I_{x^+} = 0.1$, $I_{x^-} = 0.07$, $I_{y^+} = 0.2$, $I_{y^-} = 0.14$, $I_{z^+} = 0.3$, $I_{z^+} = 0.21$. Note that the three Cartesian directions have the same intensity imbalance ratio: $i_x = i_y = i_z = 10/7$. The analytically predicted equilibrium velocities of the atomic distribution were therefore (equations 2.27, 2.26):

$$v_{x_0} = v_{y_0} = v_{z_0} = 0.520\text{ms}^{-1},$$

$$v_{x_0} = v_{y_0} = v_{z_0} = 0.528\text{ms}^{-1},$$

using the linear and quadratic equations respectively.

The equilibrium velocities were obtained from the MC by taking the logarithm of the velocity probability distributions, and fitting a quadratic to each distribution. The results were (with approximate statistical errors):

$$v_{x_0} = (0.537 \pm 0.005)\text{ms}^{-1}, \quad v_{y_0} = (0.537 \pm 0.005)\text{ms}^{-1}, \quad v_{z_0} = (0.531 \pm 0.003)\text{ms}^{-1}.$$

The quadratic prediction is closer to the MC (as is expected), however it still differs from the MC solution. This is probably due to the approximations in the analytic theory mentioned earlier, although perhaps also due to asymmetries in the atomic distribution from the non-linearities of the MC trapping forces.

The standard deviations of the MC velocity distributions were $\sigma_{v_x} = 0.37\text{ms}^{-1}$, $\sigma_{v_y} = 0.30\text{ms}^{-1}$, $\sigma_{v_z} = 0.27\text{ms}^{-1}$ and it is clear that the equilibrium velocities are quite substantial when compared to the width of the velocity distributions.

The MC was also run for a MOT, with the same intensities as in the molasses simulation, but with a magnetic field gradient of $b = 7\text{G/cm}$. The predicted equilibrium co-ordinates of the atomic distribution, using the linear approximation in equation 2.36, were:

$$x_0 = y_0 = 9.01 \times 10^{-4}\text{m}, \quad z_0 = 4.50 \times 10^{-4}\text{m}.$$

Using a process similar to the method used to find MC equilibrium velocities, the equilibrium co-ordinates in the MC were obtained:

$$x_0 = (9.45 \pm 0.06) \times 10^{-4}\text{m}, \quad y_0 = (9.38 \pm .04) \times 10^{-4}\text{m}, \quad z_0 = (4.49 \pm 0.02) \times 10^{-4}\text{m}.$$

The reasons for any differences are similar to those for Doppler molasses, with the added error margin from the use of a linear approximation in the analytic theory. If the equilibrium point is found by numerically solving the complete force equations, the result is:

$$x_0 = y_0 = 9.31 \times 10^{-4}\text{m}, \quad z_0 = 4.66 \times 10^{-4}\text{m}.$$

The standard deviations of the MC position distributions were $\sigma_x = 8.9 \times 10^{-5}\text{m}$, $\sigma_y = 5.0 \times 10^{-5}\text{m}$, $\sigma_z = 2.8 \times 10^{-5}\text{m}$ and it is clear that the equilibrium displacement is large compared with the width of the position distributions.

Chapter 3

MOTs with Complications

In the previous chapter, various analytic properties of Doppler MOTs and optical molasses were derived. A Doppler Monte Carlo simulation was also developed. The analytic theory relied on the symmetry of beam arrangements, and this chapter will be devoted to regimes where these symmetries are removed. Other complications omitted from the original MOT theory will also be considered.

When the lasers in a MOT are misaligned, various structures including rings, double rings and rings with central cores can be observed. A Doppler analytic theory for these situations will be developed in a later section, then compared with the Monte Carlo simulation and the results of other authors.

In the first section of this chapter, forces that have been neglected in the previous chapter will be treated. These forces result from the absorption and reradiation of the laser light, and upon inclusion with the earlier MOT forces, these forces can lead to density distributions markedly different from the Gaussian distributions of chapter 2. Such distributions manifest themselves in conditions where the number of atoms and/or the laser intensity are high.

Previous theoretical research on this topic will be called into question.

3.1   Reradiation and Absorption

3.1.1   The Light Side of the Force

In section 2.2 it was seen that six circularly polarised laser beams can create a trapping and cooling force on atoms, due to the Zeeman and Doppler effects. Unless otherwise stated, all beam intensities are equivalent in the MOT. This leads to an isotropic temperature, and a trapping force proportional to the vector $(x, y, 2z)$. In the calculations that follow, the trapping force on an atom will be simplified to the form $\mathbf{F}_{spring} = -k_{spring}\mathbf{r}$, where k_{spring} is a constant and the anisotropy in the z direction is removed. Note that $\mathbf{F}_{spring}$ is conservative, i.e. $\nabla \times \mathbf{F}_{spring} = \mathbf{0}$. The spring constant, k_{spring}, of the MOT can be obtained by either Doppler or sub-Doppler theoretical calculations [74].

In chapter 2, two forces which operate inside the MOT have been neglected. These forces were detailed by Sesko *et al.* [65] in 1991—a force due changes in laser beam intensity across the MOT atoms, and a force due to reradiation of laser light from the atoms.

Consider a laser beam propagating in the $+x$ direction through a MOT. The beam divergence is approximated to zero, and the beam is absorbed by atoms in the MOT cloud—lowering the intensity of the laser as x increases. The intensity drop, in travelling from (x, y, z) to $(x + dx, y, z)$, will be proportional to the initial intensity, $I_{x+}(x, y, z)$. The loss is also proportional to the number density, $n(x, y, z)$, of atoms in that region. The constant of proportionality is the absorption cross section, σ_L of the incident laser beam. This leads to the equation:

$$dI_{x+} = -\sigma_L I_{x+}(x, y, z)n(x, y, z)dx,$$

or the partial differential equation

$$\frac{\partial I_{x+}(\mathbf{r})}{\partial x} = -\sigma_L I_{x+}(\mathbf{r})n(\mathbf{r}).$$

This can be rearranged to:

$$\frac{\partial \ln (I_{x+}(\mathbf{r}))}{\partial x} = -\sigma_L n(\mathbf{r}),$$

and solved to yield

$$I_{x+}(\mathbf{r}) = I_{x_\infty} \exp\left(-\sigma_L \int_{-\infty}^{x} n(u, y, z)du\right),$$

where the intensity of the $+x$ travelling laser beam at $x = -\infty$, before absorption occurs, is I_{x_∞}.

Similarly, a laser beam propagating in the $-x$ direction, also with unattenuated intensity I_{x_∞}, has intensity at $\mathbf{r}$ given by:

$$I_{x-}(\mathbf{r}) = I_{x_\infty} \exp\left(-\sigma_L \int_{x}^{\infty} n(u, y, z)du\right).$$

If the exponentials terms of I_{x-} and I_{x+} yield values close to one (i.e. their arguments are close to zero), then the approximation $e^{-x} = 1 - x$ can be made. The linear approximation will be made for the following discussion, although many of the results still pertain to the case where the full exponentials are considered.

The approximate intensities are:

$$I_{x-}(\mathbf{r}) = I_{x_\infty} \left(1 - \sigma_L \int_{x}^{\infty} n(u, y, z)du\right),$$

$$I_{x+}(\mathbf{r}) = I_{x_\infty} \left(1 - \sigma_L \int_{-\infty}^{x} n(u, y, z)du\right).$$

The light pressure force on an atom with cross section σ, subject to incident light of intensity I has magnitude [65]:

$$F = \sigma I/c, \tag{3.1}$$

and is in the direction of the light's $\mathbf{k}$ vector. The absorption force, $\mathbf{F}_{abs}$, on an atom due to the intensity difference between the two x beams therefore has x component:

$$F_{abs_x} = \sigma_L(I_{x+}(\mathbf{r}) - I_{x-}(\mathbf{r}))/c = \sigma_L{}^2 I_{x_\infty}\left(\int_{x}^{\infty} n(u, y, z)du - \int_{-\infty}^{x} n(u, y, z)du\right)/c.$$

No y or z force components arise from the x laser beams, as the photons from both laser beams travel, and therefore create force, only in the $\pm x$ directions. Due to the symmetry of the spring constant and beam intensities, it is expected that the MOT number distribution, n, will be even in x—i.e. $n(-x, y, z) = n(x, y, z)$. This property of n leads to the simplification:

$$F_{abs_x} = \frac{-2\sigma_L{}^2 I_{x_\infty}}{c}\int_{0}^{x} n(u, y, z)du = -2k_{abs}I_{x_\infty}\int_{0}^{x} n(u, y, z)du, \tag{3.2}$$

where $k_{abs} = \sigma_L{}^2/c$.

If there are laser beams in the $\pm y$ and $\pm z$ directions with equal unattenuated intensities of I_{y_∞} and I_{z_∞} respectively, then it can be similarly shown that the remaining components of the absorptive force are:

$$F_{abs_y} = -2k_{abs}I_{y_\infty}\int_{0}^{y} n(x, u, z)du,$$

$$F_{abs_z} = -2k_{abs}I_{z_\infty}\int_{0}^{z} n(x, y, u)du,$$

if the number density, n, is even in y and z. Note that $\boldsymbol{\nabla} \cdot \mathbf{F}_{abs} = -k_{abs}I_{tot}n(\mathbf{r})$, where $I_{tot} = 2(I_{x_\infty} + I_{y_\infty} + I_{z_\infty})$. The divergence is always negative ($n > 0$) and hence the absorptive force compresses a cloud of atoms, and is equivalent to an interatomic attractive force. Another feature of $\mathbf{F}_{abs}$ is that it is non-conservative in most density distributions—this will be important later on.

The other force on atoms in a MOT is the reradiation force, $\mathbf{F}_{rerad}$. Atoms under the influence of the trapping force, $\mathbf{F}_{spring}$, absorb photons from the laser beams surrounding the MOT. When a photon is

absorbed by an atom, it must return to its ground state via spontaneous emission, before it can absorb another photon. The atoms in the MOT are therefore continually reradiating photons provided by the laser beams and are, in effect, point sources of light themselves. In section 2.3, spontaneously emitted photons were seen to have randomly distributed momenta, and the isotropic emission distribution will be assumed throughout this section.

Reradiated photons from an atom will be spherically distributed around the atom, and if a nearby atom (a, say) absorbs such a photon, it will experience a repulsive force from the radiating atom. When a spontaneously emits the absorbed photon, it will, on average, receive no impulse, and so the force arises solely from the absorption process.

In a laser field of intensity I, an atom absorbs, and therefore emits, energy at a rate $\sigma_L I$. If this energy is reradiated isotropically about the atom, it is straightforward to show that the intensity of the reradiated light at distance d from the atom is $I_{rad} = \sigma_L I/(4\pi d^2)$. An important point to note is that the absorbed light undergoes frequency redistribution on re-emission. The probabilities of an atom absorbing a scattered photon or a direct laser photon are therefore slightly different. The cross-section of the reradiated light, σ_R, is distinct from σ_L.

Using equation 3.1 it can now be seen that the magnitude of the force on an atom a, separated by d from an atom in a laser field of total intensity $I(\mathbf{r})$ is given by the equation:

$$F = \sigma_R \sigma_L I(\mathbf{r})/(4\pi c d^2) = k_{rerad} I(\mathbf{r})/(4\pi d^2) \tag{3.3}$$

where $k_{rerad} = \sigma_R \sigma_L/c$ and the force is repulsive.

The force between two atoms, given above, can be extended to the force on an atom at a point $\mathbf{r}$ in an atomic distribution, by summing (integrating) the forces on the atom at $\mathbf{r}$ due to the other reradiating atoms in the distribution. This yields:

$$\mathbf{F}_{rerad}(\mathbf{r}) = k_{rerad}/(4\pi) \int n(\mathbf{r}')I(\mathbf{r}')\frac{\mathbf{r} - \mathbf{r}'}{|\mathbf{r} - \mathbf{r}'|^3}d^3r',$$

and Gauss' law can be used to obtain the result:

$$\boldsymbol{\nabla} \cdot \mathbf{F}_{rerad} = k_{rerad}I(\mathbf{r})n(\mathbf{r}). \tag{3.4}$$

It has been assumed that an incident laser photon is unlikely to be absorbed and emitted more than twice by atoms in the MOT.

The total intensity in the MOT, in the low-absorption limit, can be approximated by:

$$I(\mathbf{r}) = I_{x^+}(\mathbf{r}) + I_{x^-}(\mathbf{r}) + I_{y^+}(\mathbf{r}) + ... \approx 2(I_{x_\infty} + I_{y_\infty} + I_{z_\infty}) = I_{tot},$$

and this approximation can be included in equation 3.4:

$$\boldsymbol{\nabla} \cdot \mathbf{F}_{rerad} = k_{rerad}I(\mathbf{r})n(\mathbf{r}) \approx k_{rerad}I_{tot}n(\mathbf{r}).$$

The form of the divergence is similar to $\boldsymbol{\nabla} \cdot \mathbf{F}_{abs}$, except with opposite sign, so it expands the atomic cloud. It can also be shown that $\mathbf{F}_{rerad}$ is conservative by applying Leibnitz's rule to $\boldsymbol{\nabla} \times \mathbf{F}_{rerad}$.

If the atomic distribution, n, is spherically symmetric, then it is possible to show, using Gauss' law, that the reradiation force on an atom is radially outward with magnitude:

$$F_{rerad}(r) = k_{rerad}I_{tot}\frac{\int_0^r n(u)u^2du}{r^2}. \tag{3.5}$$

3.1.2 Solving the new equations for n and T

The combination of three forces creates the position-dependent total force $\mathbf{F}_{tot} = \mathbf{F}_{spring} + \mathbf{F}_{abs} + \mathbf{F}_{rerad}$ on individual atoms in the MOT. The MOT atoms are in a gas much like an ideal gas, as they have a low

density and only weakly interact with each other. For this reason the equation $P(\mathbf{r}) = k_B n(\mathbf{r}) T(\mathbf{r})$ is used to model the gas properties, where P and T are the pressure and temperature in the cloud.

The equation, $\boldsymbol{\nabla} P(\mathbf{r}) = \mathbf{F}_{tot}(\mathbf{r})n(\mathbf{r})$, is valid for any material with a stress tensor consisting solely of equal diagonal elements, P [45]. This equation is therefore valid for an ideal gas and can thus be applied to the atomic vapour in a MOT. Combining the last three equations leads to:

$$k_B \left(T(\mathbf{r})\boldsymbol{\nabla} n(\mathbf{r}) + n(\mathbf{r})\boldsymbol{\nabla} T(\mathbf{r}) \right) = (\mathbf{F}_{spring} + \mathbf{F}_{abs} + \mathbf{F}_{rerad})n(\mathbf{r}). \tag{3.6}$$

At this point, the temperature will be considered constant throughout the distribution, or equivalently $\boldsymbol{\nabla} T(\mathbf{r}) = \mathbf{0}$. With this restriction, equation 3.6 reduces to:

$$k_B T \boldsymbol{\nabla}(\ln n(\mathbf{r})) = (\mathbf{F}_{spring} + \mathbf{F}_{abs} + \mathbf{F}_{rerad}). \tag{3.7}$$

If $\mathbf{F}_{spring}$ is the only force considered in equation 3.7, then the density solution is given by $n(\mathbf{r}) = n_0 \exp(-k_{spring}r^2/(2k_B T))$, where $r = |\mathbf{r}|$. This is a Gaussian density distribution, in agreement with the solutions of section 2.2. It is also possible to find spherically symmetric solutions to equation 3.7 if only $\mathbf{F}_{spring}$ and $\mathbf{F}_{rerad}$ are considered. Thus, excluding the $\mathbf{F}_{rerad}$-only MOT, because the net force is repulsive, equation 3.7 always yields a solution when the non-conservative absorptive force is omitted.

The divergence of equation 3.7 can be taken to obtain the second order partial differential equation (PDE):

$$k_B T \boldsymbol{\nabla}^2(\ln n(\mathbf{r})) = \boldsymbol{\nabla} \cdot \mathbf{F}_{tot} \approx (k_{rerad} - k_{abs})I_{tot}n(\mathbf{r}) - 3k_{spring}r. \tag{3.8}$$

In ref. [65] it was stated that this differential equation was solved numerically. A density solution, n, for equation 3.8 is not necessarily a solution to equation 3.7 however, as new 'solutions' arise from differentiation. For example it is possible to find spherically symmetric solutions for n that obey equation 3.8, but these 'solutions' do not obey equation 3.7 and are thus not solutions at all. A one-dimensional example is the differential equation $y'(x) = y(x)$, which has solution $y(x) = Ae^x$. Upon differentiation of the initial equation, $y''(x) = y'(x)$ is obtained, which has a solution space, $y(x) = Ae^x + B$, larger than that of the original differential equation.

It would seem logical to employ a numerical integration technique to solve equation 3.7 or the elliptic PDE of equation 3.8. Difficulties arise in the specification of boundary conditions and iterative solving techniques however. The reradiative force at a point is determined by the behaviour of $n(\mathbf{r})$ throughout space. The absorptive force requires less information, however knowledge of the nature of n, along certain line segments in 3D space, is still necessary before iterative techniques can be used. Such techniques would be very complex, due to the highly non-linear nature of the forces. Elliptic PDEs also require boundary conditions, BCs, on a closed 3D surface before solutions can be obtained [81]. A possible BC would be to set $n(r) = 0$ on a sphere with large radius r. This BC *should* ensure that n decayed to zero at large distances from the MOT, however the behaviour of computed 'solutions' outside the sphere would not be known. The condition that n tends to zero in the far field does not necessarily yield a unique n solution either. For these reasons a Taylor series method was employed instead of conventional numerical PDE solving techniques.

It will now be shown that, unlike situations where the force $\mathbf{F}_{abs}$ is omitted, 'smooth' *physical* solutions to equation 3.7 do not exist upon inclusion of $\mathbf{F}_{abs}$. 'Smooth' is used here to describe a function that has a Taylor expansion about $\mathbf{r} = \mathbf{0}$ with an infinite radius of convergence. This result contradicts (in the absence of 'unsmooth' solutions) Sesko *et al.*'s claim of a numerical solution to equation 3.8. Sesko *at al.* did not discuss whether this solution was consistent with equation 3.7 [65].

The left hand side, LHS, of equation 3.7 can be written as the gradient of a single function—or equivalently the curl of the LHS is zero. From this it can be inferred that the curl of the RHS is also zero, and because $\mathbf{F}_{spring}$ and $\mathbf{F}_{rerad}$ are conservative, the condition $\boldsymbol{\nabla} \times \mathbf{F}_{abs} = \mathbf{0}$ is obtained. Thus equation 3.7 will only be soluble when the density, n, is constrained in such a way as to make $\mathbf{F}_{abs}$ conservative.

A number density, $n(\mathbf{r})$, that generates a conservative absorptive force provides a *possible* solution to equation 3.7, however some n distributions that satisfy the condition on $\mathbf{F}_{abs}$ do not satisfy equation 3.7.

Proving that all n distributions with conservative $\mathbf{F}_{abs}$ are unphysical is actually a stronger condition than is necessary to show that there are no physical solutions to equation 3.7.

The definition of $\mathbf{F}_{abs}$ implies the force is conservative precisely when:

$$I_{x_\infty}\frac{\partial}{\partial y}\int_0^x n(u,y,z)du = I_{y_\infty}\frac{\partial}{\partial x}\int_0^y n(x,u,z)du,$$

$$I_{x_\infty}\frac{\partial}{\partial z}\int_0^x n(u,y,z)du = I_{z_\infty}\frac{\partial}{\partial x}\int_0^z n(x,y,u)du,$$

$$I_{y_\infty}\frac{\partial}{\partial z}\int_0^y n(x,u,z)du = I_{z_\infty}\frac{\partial}{\partial y}\int_0^z n(x,y,u)du$$

and Leibnitz's rule can be applied to these equations when necessary.

Because the laser beam/magnetic field arrangement is symmetric in x, y and z, the number density function n must also be symmetric in x, y, z. The Taylor expansion of n must therefore only include terms which have these symmetries. This implies that Taylor expansion terms are functions of x^2, y^2 and z^2, however to retain as much generality as possible, all terms of the form $|x|^{n_x}|y|^{n_y}|z|^{n_z}$, where $n_{x_i} \in \{0,1,2,...\}$, will be included in the expansion.

The Taylor expansion in the $z = 0$ plane (no z-dependent Taylor terms) is considered, as it will be enough to illustrate the non-existence of a physical n solution in a MOT. Consider the equation:

$$I_{x_\infty}\frac{\partial}{\partial y}\int_0^x n(u,y)du = I_{y_\infty}\frac{\partial}{\partial x}\int_0^y n(x,u)du,$$

$$\text{where} \quad n(x,y) = \sum_{i=0}^\infty\sum_{j=0}^\infty n_{i,j}|x|^i|y|^j. \tag{3.9}$$

If the solution is restricted to the quadrant $x \geq 0$, $y \geq 0$, then the density has the form:

$$n(x,y) = \sum_{i=0}^\infty\sum_{j=0}^\infty n_{i,j}x^iy^j, \tag{3.10}$$

and the moduli can be disregarded. The entire solution in the $z = 0$ plane, given in equation 3.9, can be obtained by symmetrically extending the solution to equation 3.10 from its quadrant to the rest of the plane (the co-efficients of equations 3.9 and 3.10 will be the same).

The Taylor series in equation 3.10 can be rearranged, assuming absolute convergence, to:

$$n(x,y) = \sum_{N=0}^\infty\sum_{j=0}^N n_{N-j,j}x^{N-j}y^j.$$

The results:

$$I_{x_\infty}\frac{\partial}{\partial y}\int_0^x n(u,y)du = I_{x_\infty}\sum_{N=0}^\infty\sum_{j=0}^N n_{N-j,j}\frac{j}{N-j+1}x^{N-j+1}y^{j-1},$$

$$\text{and} \quad I_{y_\infty}\frac{\partial}{\partial x}\int_0^y n(x,u)du = I_{y_\infty}\sum_{N=0}^\infty\sum_{j=0}^N n_{N-j,j}\frac{N-j}{j+1}x^{N-j-1}y^{j+1}$$

follow. There is no $N = 0$ term for either equation. The $j = 0$ terms are zero in the first equation, and the $j = N$ terms are zero in the second equation. The two j summations can therefore be taken from $j = 1 \to N$ and $j = 0 \to N-1$ respectively. The $j = 1 \to N$ summation can be replaced by a $j = 0 \to N-1$ summation if all j's in the summation addend are replaced by $j + 1$.

The condition on n is thus:

$$I_{x_\infty}\sum_{N=1}^\infty\sum_{j=0}^{N-1} n_{N-j-1,j+1}\frac{j+1}{N-j}x^{N-j}y^j = I_{y_\infty}\sum_{N=1}^\infty\sum_{j=0}^{N-1} n_{N-j,j}\frac{N-j}{j+1}x^{N-j-1}y^{j+1}. \tag{3.11}$$

The LHS has an x^N term when $j = 0$, however the RHS has no such term. Equating coefficients yields $I_{x_\infty}\frac{n_{N-1,1}}{N}x^N = 0x^N$ or $n_{N-1,1} = 0$ for $N \geq 1$. Similarly the y^N term of the RHS leads to the condition $n_{1,N-1} = 0$ for $N \geq 1$.

The condition of equation 3.11 reduces to:

$$I_{x_\infty} \sum_{N=1}^{\infty} \sum_{j=0}^{N-2} n_{N-j-2,j+2} \frac{j+2}{N-j-1} x^{N-j-1} y^{j+1} = I_{y_\infty} \sum_{N=1}^{\infty} \sum_{j=0}^{N-2} n_{N-j,j} \frac{N-j}{j+1} x^{N-j-1} y^{j+1}.$$

This in turn leads to the coefficient relation:

$$n_{N-(j+2),j+2} = i \frac{(N-j-1)(N-j)}{(j+1)(j+2)} n_{N-j,j} \tag{3.12}$$

for $j = 0 \to N-2$, and where $i = I_{y_\infty}/I_{x_\infty}$.

Suppose that N is odd, i.e. $N = 2l+1$ where l is an integer, $l \geq 0$. The equation 3.12 shows that $n_{0,2l+1}$, $n_{2,2l-1}$, $n_{4,2l-3}$,....., $n_{2l,1}$ are all scalar multiples of each other. The earlier condition that $n_{N-1,1} = n_{2l,1} = 0$ therefore means that all of these coefficients are zero. Similarly $n_{1,2l}$, $n_{3,2l-2}$, $n_{5,2l-4}$,....., $n_{2l+1,0}$ are all zero, and so all n co-efficients with odd N are zero.

If N is even, i.e. $N = 2l$ where $l \geq 1$, then equation 3.12 and the relation $n_{1,N-1} = 0$ can be used again to show that $n_{1,2l-1}$, $n_{3,2l-3}$, $n_{5,2l-5}$,....., $n_{2l-1,1}$ are all zero. The remaining non-zero coefficients are those of the form $n_{N-j,j}$, where $N = 2l$ is even, and $j = 2k$ is also even. The condition on these coefficients is:

$$n_{2(l-k-1),2(k+1)} = i \frac{2(l-k)(2(l-k)-1))}{2(k+1)(2k+1)} n_{2(l-k),2k}$$

which can be used to show that for $0 \leq k \leq l$,

$$n_{2(l-k),2k} = i^k \binom{2l}{2k} n_{2l,0}.$$

The entire solution in the (x, y) plane can therefore be determined by the x-only co-efficients, which is equivalent to defining the function behaviour on the x (or y) axis. The general 2D density surface, with conservative absorptive force, is given by:

$$\sum_{l=0}^{\infty} \sum_{k=0}^{l} i^k \binom{2l}{2k} n_{2l,0} x^{2(l-k)} y^{2k}.$$

The expansion for n along the x-axis $(y = 0)$ is:

$$\sum_{l=0}^{\infty} n_{2l,0} x^{2l}.$$

In order to obtain a physical solution to the MOT equations, the MOT must be localised in space:

$$\lim_{r \to \infty} n(r) = 0 \quad \text{where} \quad r = \sqrt{x^2 + y^2},$$

along any path through the (x, y) plane. Certainly a requirement for n is that:

$$\lim_{x \to \infty} \left(\sum_{l=0}^{\infty} n_{2l,0} x^{2l} \right) = c.$$

where c is zero, but will be kept in this form for generality. It is also clear that

$$\lim_{x \to \infty} \left(\sum_{l=1}^{\infty} n_{2l,0} x^{2l} \right) = c - n_{0,0}. \tag{3.13}$$

Consider the line $x = \sqrt{i} y$—the surface along this line has the form:

$$n(x, x/\sqrt{i}) = \sum_{l=0}^{\infty} \sum_{k=0}^{l} i^k \binom{2l}{2k} n_{2l,0} x^{2(l-k)} (x/\sqrt{i})^{2k}.$$

The relation $\sum_{k=0}^{l} \binom{2l}{2k} = 2^{2l-1}$, where $l \geq 1$, can then be implemented to reduce this equation to:

$$n(x, x/\sqrt{i}) = n_{0,0} + \frac{1}{2} \sum_{l=1}^{\infty} n_{2l,0} (2x)^{2l}. \tag{3.14}$$

The limit of the infinite sum in equation 3.14 as $x \to \infty$ is clearly the same as the limit in equation 3.13—i.e. $c - n_{0,0}$. Therefore the limit as $x \to \infty$ in equation 3.14 is given by:

$$\lim_{x \to \infty} n(x, x/\sqrt{i}) = \frac{1}{2}(n_{0,0} + c).$$

The reason why n is unphysical now becomes clear. If the surface, along the x axis, tends to zero for large $|x|$ (i.e. $c = 0$), then the solution surface doesn't tend to zero along all paths for which $r \to \infty$, as seen in the counter-example above. A graphical display of a typical n surface, subject to the conservative absorptive force condition, is shown in figure 3.1.

Surfaces with $n_{0,0} = 0$, i.e. a 'hole' in the atomic distribution at $(x, y) = (0, 0)$, satisfy the criteria that $n \to 0$ along both the x and $x = y$ axes, however there are other paths in the xy plane along which $\lim_{r \to \infty} n(x, y) \neq 0$ and so these n distributions are also unphysical. This will not be shown in general, due to the complex nature of the unphysical n surface 'arms' (see figure 3.1) in the $n_{0,0} = 0$ scenario.
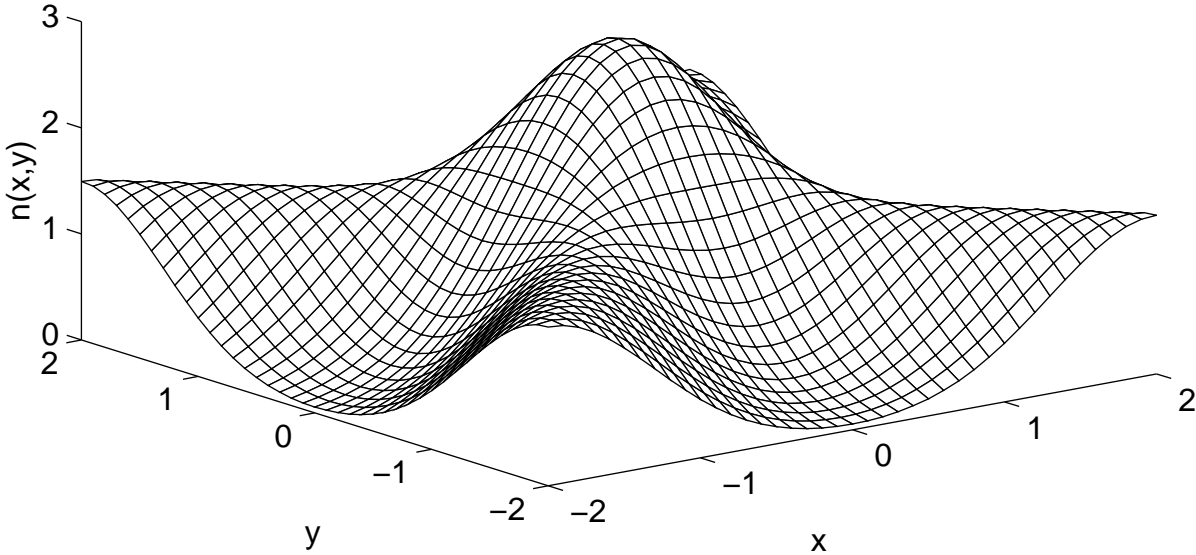

Figure 3.1: The unique n 'solution' surface with $n(x, 0) = 3e^{-x^2}$, subject to the condition that $\mathbf{F_{abs}}$ is conservative. Along the $|x| = |y|$ 'arms' the n solution tends to the value $n_{0,0}/2 = n(0, 0)/2 = 1.5$. The Taylor expansion includes terms up to order 100.

The n surfaces were created in Matlab. As well as the truncated Taylor expansion for the n surfaces, it was also possible, given the n series, to create a Taylor expansion of $\mathbf{F}_{abs}$ from its definition (equation 3.2), followed by an expansion of $(\mathbf{\nabla} \times \mathbf{F}_{abs})_z$ through term-by-term differentiation. The deviation of $(\mathbf{\nabla} \times \mathbf{F}_{abs})_z$ from zero, over the region of the solution surface, gave an indication of the n solution's convergence. Matlab encountered numerical difficulties occasionally, as the higher order Taylor coefficients are stored in the same matrix as the other coefficients, to the same number of decimal places.

The fact that no physical solution exists when $\mathbf{F}_{abs}$ is included in the theory suggests that errors were present during the force derivation: invalid assumptions were used, or the general model for the force was inaccurate. Another possibility is that there *is* a solution surface, but it does not have a Taylor expansion valid throughout the (x, y) plane. The conclusion that no solution exists when $\mathbf{F}_{abs}$ is included in the MOT theory could be intuitively seen from the condition that the force was only conservative for certain n distributions, however. This condition greatly restricts the solution space of n, and this restriction could confine n to an unphysical region of solution space.

Further evidence against $\mathbf{F}_{abs}$ can be found by trying to solve for n, using Taylor expansions, when

only $\mathbf{F}_{abs}$, or the combination of $\mathbf{F}_{abs}$, $\mathbf{F}_{spring}$ are acting. If these forces alone are considered in the MOT, then from the previous proof it can be ascertained that no *physical* solution will exist for this case. From the Taylor expansion it can further be shown that in this case no solutions to equation 3.7 exist *at all*. A sketched proof follows.

Given a constant temperature, and a value of $n_{0,0}$, it is possible to determine the behaviour of n along the x-axis, as long as the relatively complicated $\mathbf{F}_{rerad}$ is omitted. The entire n 'solution' surface can then be generated using the conservative-$\mathbf{F}_{abs}$ Taylor expansion developed earlier. By substituting the n 'solution' into the two sides of equation 3.7, it is possible to show that the sides are unequal, even at the low-order Taylor term level. This shows that solutions to equation 3.7 cannot be obtained. Although the proof of the non-physical nature of n required a solution function with infinite Taylor convergence radius, the non-existence proof for n (omitting $\mathbf{F}_{rerad}$) only requires the solution to have a convergent Taylor expansion near the origin.

Whilst no 2D solution for n exists when $\mathbf{F}_{abs}$, or a combination of $\mathbf{F}_{abs}$ and $\mathbf{F}_{spring}$, are acting in a MOT, solutions exist in 1D. If $\mathbf{F}_{abs}$ is the only force acting in one dimension, then analytic, and more importantly *physical*, solutions can be obtained for the atomic distribution (an approximate solution is given in ref. [18], and a more exact solution in ref. [40]). The equations developed in these papers can be easily extended to include $\mathbf{F}_{spring}$ in the 1D formalism. Although analytic solutions to these equations do not exist, numerical, and apparently physical, solutions can be obtained.

3.1.3 Where to now?

Having concluded that a solution to equation 3.7 is unlikely to exist if $\mathbf{F}_{abs}$ is included, it now remains to suggest viable alternatives for modelling the MOT distribution. It could be that the linear approximation for an exponential (see $\mathbf{F}_{abs}$ description) caused the problem, but the two descriptions are extremely similar in the case of low absorption. In this low absorption regime it would seem plausible that *both* descriptions create unphysical solutions. The methods would thus yield no solution in the low absorption regime, and hence not in general.

Another possibility is that $\boldsymbol{\nabla} T$ is non-zero. This opens up new realms in the sense that it could explain the experimentally observed increase in temperature as the number of atoms, N, in a MOT increases [22], [14]. A more general form of equation 3.7 is:

$$\boldsymbol{\nabla} P(\mathbf{r}) = k_B \boldsymbol{\nabla}(T(\mathbf{r})n(\mathbf{r})) = (\mathbf{F}_{tot}) n(\mathbf{r}). \tag{3.15}$$

Taking the curl of both sides leads to the condition on n that:

$$\boldsymbol{\nabla} \times (\mathbf{F}_{tot} n(\mathbf{r})) = \mathbf{0}, \tag{3.16}$$

and because $\mathbf{F}_{spring}$, $\mathbf{F}_{rerad}$ are conservative,

$$n(\mathbf{r})\boldsymbol{\nabla} \times \mathbf{F}_{abs} + \boldsymbol{\nabla}(n(\mathbf{r})) \times \mathbf{F}_{tot} = \mathbf{0}. \tag{3.17}$$

This new restriction on n is more complex than before, as it relies on all the forces, not just $\mathbf{F}_{abs}$. In the $\boldsymbol{\nabla} T = \mathbf{0}$ regime the condition $\boldsymbol{\nabla} \times \mathbf{F}_{abs} = \mathbf{0}$ was a necessary, but not sufficient, condition for an n solution to equation 3.7. The condition of equation 3.16 however, is a necessary and sufficient condition for an n solution to equation 3.15. The temperature acts like a 'correcting factor' when it is allowed to vary. Although solutions to equation 3.15 will now be possible, the question remains as to whether the solutions are physical.

For this reason solutions to equation 3.17 were attempted. A Taylor expansion technique in the $z = 0$ plane was used, similar to the one used in the previous subsection. Only the absorptive and 'spring' forces, $\mathbf{F}_{abs}$ and $\mathbf{F}_{spring}$ will be included in the theory, as it is extremely difficult to get a Taylor expansion for $\mathbf{F}_{rerad}$.

A formula for multiplying two Taylor expansions together will be used: given two Taylor-expandable functions, $f(x,y) = \sum_{i=0}^{\infty} \sum_{j=0}^{\infty} f_{i,j} x^i y^j$ and $g(x,y) = \sum_{i=0}^{\infty} \sum_{j=0}^{\infty} g_{i,j} x^i y^j$, then their product has Taylor expansion:

$$h(x,y) = f(x,y)\,g(x,y) = \sum_{i=0}^{\infty} \sum_{j=0}^{\infty} h_{i,j} x^i y^j, \qquad (3.18)$$

where $h_{i,j} = \sum_{a=0}^{i} \sum_{b=0}^{j} f_{a,b} g_{i-a,j-b}$. The coefficients of the product function are obtained by multiplying out the Taylor series term-by-term.

For simplicity the lasers in the x, y and z directions will now be set to the same intensity $I_{x_\infty} = I_{y_\infty} = I_{tot}/6$. Due to the symmetry of the laser light, the atomic distribution will have the property $n(x,y) = n(y,x)$, and n will also be even in x and y as before. The Taylor expansion coefficients for $n(x,y) = \sum_{i=0}^{\infty} \sum_{j=0}^{\infty} n_{2i,2j} x^{2i} y^{2j}$ have the property $n_{2i,2j} = n_{2j,2i}$, and n can be written:

$$n(x,y) = \sum_{i=0}^{\infty} \sum_{j=0}^{\infty} n_{\min(2i,2j),\max(2i,2j)} x^{2i} y^{2j}. \qquad (3.19)$$

The rather unwieldy maximum/minimum information will be omitted in subsequent Taylor coefficients equations for n, although the symmetric nature of the Taylor co-efficient indices will be applied later on. The components of the absorption force due to n can be derived using equation 3.2:

$$F_{abs_x} = \sum_{i=0}^{\infty} \sum_{j=0}^{\infty} f_{2i,2j}^{ax} x^{2i+1} y^{2j},$$

$$F_{abs_y} = \sum_{i=0}^{\infty} \sum_{j=0}^{\infty} f_{2i,2j}^{ay} x^{2i} y^{2j+1},$$

where $f_{2i,2j}^{ax} = -k_{abs} I_{tot}/3 \frac{n_{2i,2j}}{2i+1}$ and $f_{2i,2j}^{ay} = -k_{abs} I_{tot}/3 \frac{n_{2i,2j}}{2j+1}$.

As only the trapping and absorptive forces are under consideration, the total force is given by $\mathbf{F}_{tot} = \mathbf{F}_{abs} - k_{spring}\mathbf{r}$. Thus the components of $\mathbf{F}_{tot}$ are:

$$F_{tot_x} = -k_{spring}x + \sum_{i=0}^{\infty} \sum_{j=0}^{\infty} f_{2i,2j}^{ax} x^{2i+1} y^{2j} = \sum_{i=0}^{\infty} \sum_{j=0}^{\infty} f_{2i,2j}^{tx} x^{2i+1} y^{2j},$$

$$F_{tot_y} = -k_{spring}x + \sum_{i=0}^{\infty} \sum_{j=0}^{\infty} f_{2i,2j}^{ay} x^{2i} y^{2j+1} = \sum_{i=0}^{\infty} \sum_{j=0}^{\infty} f_{2i,2j}^{ty} x^{2i} y^{2j+1},$$

where $f_{2i,2j}^{tx} = -\delta_0^i \delta_0^j k_{spring} + f_{2i,2j}^{ax}$, $f_{2i,2j}^{ty} = -\delta_0^i \delta_0^j k_{spring} + f_{2i,2j}^{ay}$, and δ refers to the Kronecker delta.

In the $z = 0$ plane equation 3.16 reduces to:

$$\frac{\partial(nF_{tot_y})}{\partial x} - \frac{\partial(nF_{tot_x})}{\partial y} = 0,$$

and a modified version of equation 3.18 can be used to determine the relations:

$$n\,F_{tot_x} = \sum_{i=0}^{\infty} \sum_{j=0}^{\infty} \xi_{2i,2j}^x x^{2i+1} y^{2j},$$

$$n\,F_{tot_y} = \sum_{i=0}^{\infty} \sum_{j=0}^{\infty} \xi_{2i,2j}^y x^{2i} y^{2j+1},$$

where $\xi_{2i,2j}^x = \sum_{a=0}^{i} \sum_{b=0}^{j} n_{2a,2b} f_{2(i-a),2(j-b)}^{tx}$ and $\xi_{2i,2j}^y = \sum_{a=0}^{i} \sum_{b=0}^{j} n_{2a,2b} f_{2(i-a),2(j-b)}^{ty}$.

Differentiating these expressions by their appropriate co-ordinate yields:

$$\frac{\partial(nF_{tot_x})}{\partial y} = \sum_{i=0}^{\infty} \sum_{j=0}^{\infty} 2(j+1)\, \xi_{2i,2(j+1)}^x x^{2i+1} y^{2j+1},$$

$$\frac{\partial(nF_{tot_y})}{\partial x} = \sum_{i=0}^{\infty}\sum_{j=0}^{\infty} 2(i+1)\,\xi_{2(i+1),2j}^{y}\,x^{2i+1}y^{2j+1}.$$

Comparing coefficients, it is clear that in order for equation 3.16 to hold, the relation:

$$2(j+1)\,\xi_{2i,2(j+1)}^{x} = 2(i+1)\,\xi_{2(i+1),2j}^{y},$$

must be satisfied. Expanding the ξ terms leads to the equation:

$$2(j+1)\sum_{a=0}^{i}\sum_{b=0}^{j+1} n_{2a,2b} f_{2(i-a),2(j+1-b)}^{tx} = 2(i+1)\sum_{a=0}^{i+1}\sum_{b=0}^{j} n_{2a,2b} f_{2(i+1-a),2(j-b)}^{ty},$$

or, after dividing through by k_{spring},

$$2(j+1)\sum_{a=0}^{i}\sum_{b=0}^{j+1} n_{2a,2b}\left(\delta_a^i \delta_b^{j+1} + \frac{k_{abs}I_{tot}}{3k_{spring}}\frac{n_{2(i-a),2(j+1-b)}}{(2(i-a)+1)}\right) =$$
$$2(i+1)\sum_{a=0}^{i+1}\sum_{b=0}^{j} n_{2a,2b}\left(\delta_a^{i+1} \delta_b^{j} + \frac{k_{abs}I_{tot}}{3k_{spring}}\frac{n_{2(i+1-a),2(j-b)}}{(2(j-b)+1)}\right) \qquad (3.20)$$

This relation can be simplified by applying the symmetries of the Taylor coefficients (see equation 3.19); effectively reducing the number of coefficients by a factor of two. The relationships are quite complex and were solved in Mathematica, as it was necessary to use its ability to re-arrange equations in order to solve for the coefficients. When the $\nabla T = \mathbf{0}$ case was considered in the previous subsection, it was shown that the solution surface, $n(x,y)$, could be obtained given only the function dependence along the x (or y) axis. This property, although not quite as obvious, also holds when $\nabla T \neq \mathbf{0}$. Note that the Taylor coefficients only depend on the *ratio* of $k_{abs}I_{tot}$ and $3k_{spring}$. The two constants k_{spring} and $k_{abs}I_{tot}$, by themselves, are therefore not important in determining the distribution function n—however the separate constants, rather than their ratio, are necessary to solve for the temperature distribution.
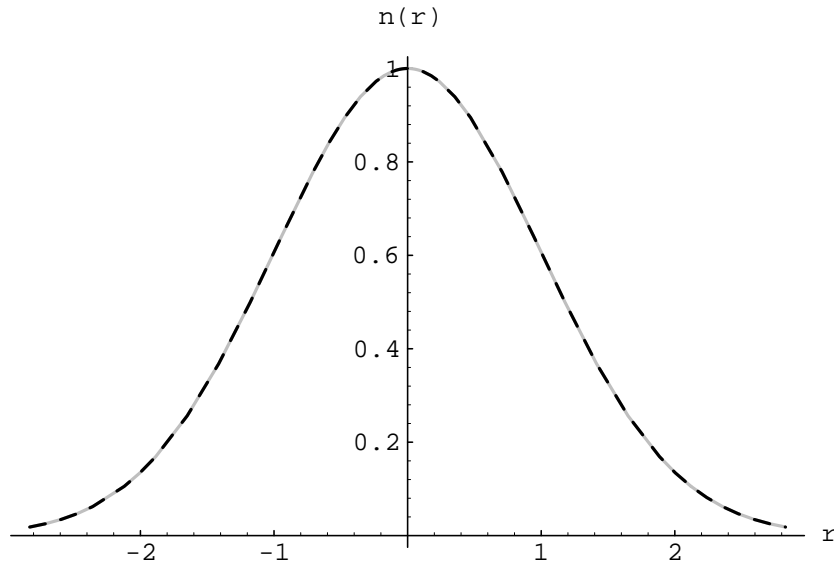

Figure 3.2: Solutions for n along the x (dashed) and $x = y$ (grey) axes as a function of distance from the origin, r. The figure entails a situation where $n(x,0) = e^{-x^2/2}$, $k_{spring} = 1$ and no absorptive force acts—i.e. $k_{abs}I_{tot} = 0$. The numerical n solution differs from its analytic, spherically symmetric counterpart by less than 10^{-15}.

The Mathematica program was used to reproduce the results of the $\nabla T = \mathbf{0}$ subsection, in order to check its numerical precision compared to Matlab. The results were quite similar. A second test was to set k_{abs} to zero, and to enter initial data curves of the form $n(x,0) = n_0 \exp(-k_{spring}x^2/2)$. It is easy to show
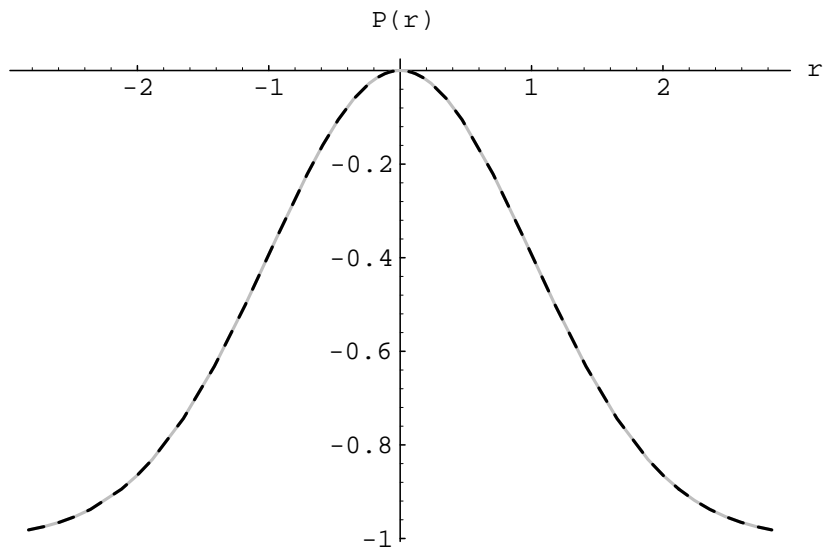
Figure 3.3: A similar plot for the pressure, P', obtained with the parameters of the previous figure. An arbitrary integration constant can be added to $P'(x, y)$, to ensure the function tends to zero along the x axis.
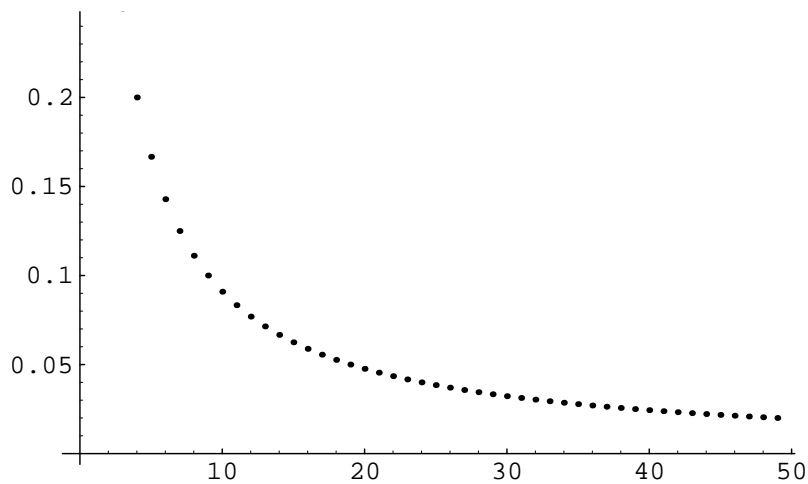

Figure 3.4: A plot of $|a_{i+1}/a_i|$ versus i. The ratio tends to zero as $i \to \infty$, and this indicates that the Taylor series will have an infinite radius of convergence.
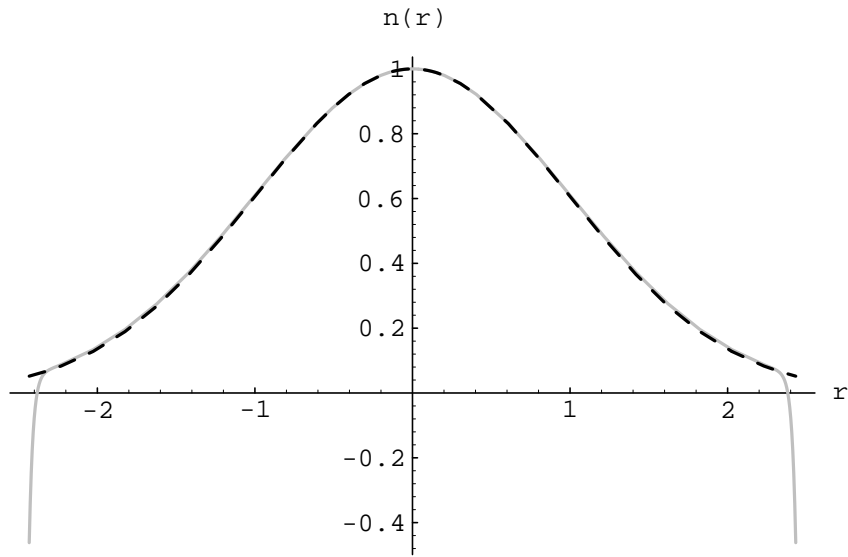
Figure 3.5: A similar plot to the figure of 1D n profiles for $k_{abs} = 0$—except the change $k_{abs}I_{tot} = -0.3$ has been made. Note that the solution is still approximately spherically symmetric.
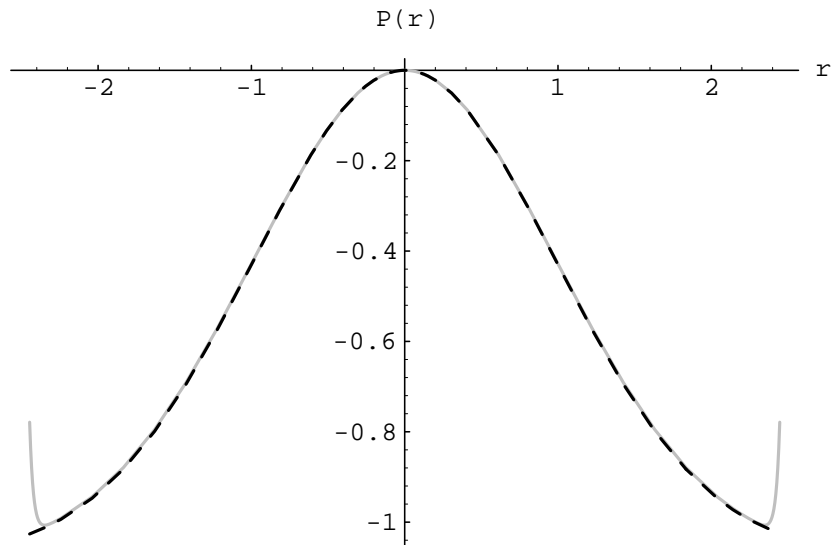

Figure 3.6: The pressure, P', corresponding to the previous figure. An arbitrary integration constant can be added to $P'(x, y)$, to ensure the function tends to zero along the x axis. Whether $P = P'(x, y) + P_0$ tends to zero along other paths as $r \to \infty$ will determine if the pressure is physical.
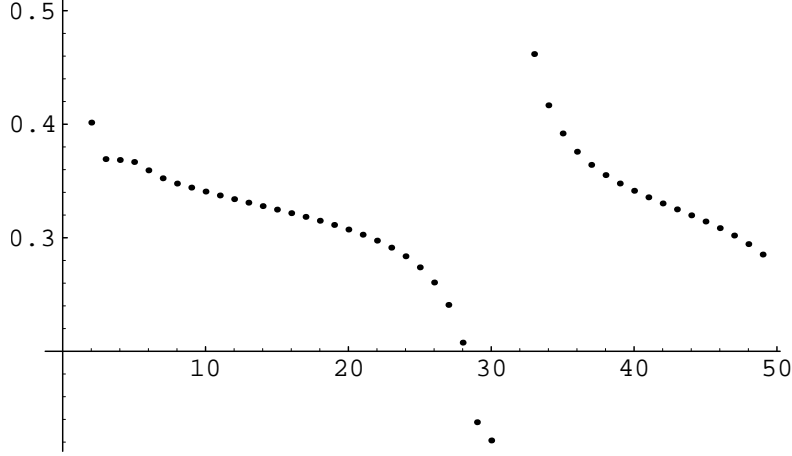
Figure 3.7: A plot of $|a_{i+1}/a_i|$ versus i when $k_{abs}I_{tot} = -0.3$. The ratio $|a_i/a_{i+1}|$ averages to ≈ 3 and thus the Taylor series is only expected to converge until $x \approx 3$: a radial distance of $r \approx 4$ along the $x = y$ axis (the previous figure indicates a radius of convergence, $r \approx 2.5$).

that these initial conditions should yield the analytic solution $n(x, y) = n_0 \exp\left(-k_{spring}(x^2 + y^2)/2\right)$, and the computer program obtained this result (figure 3.2).

Given the solution surface for n, it was possible to construct the forces and derivatives $\frac{\partial n}{\partial x}$, F_{tot_x}, $\frac{\partial (nF_{tot_x})}{\partial y}$ etc., via the Taylor coefficients for n, or by the product of these constructions. Various checks were used to determine the validity of the expansions. Other computational checks verified that solution surfaces to equation 3.16 had been obtained.

The pressure, P, could be computed from the density distribution, n. A Taylor expansion for $\frac{\partial P}{\partial x} = nF_{tot_x}$ (equation 3.15) was obtained by taking the product of the Taylor expansions for n and F_{tot_x}. Integrating with respect to x gives the pressure P, subject to an integration 'constant' $g(y)$. The pressure within the MOT can then be found, using the symmetry relation $P(x, y) = P(y, x)$ to determine $g(y)$, although an arbitrary integration constant, $P_0 = P(0, 0)$, remains. The pressure, before inclusion of the integration constant, will be labelled P' (figures 3.3, 3.6) and obeys the relation $P = P' + P_0$.

It now remains to check whether the solutions to equation 3.15 are physical or not: P' and the density are required to obey the limits $P'(\mathbf{r}) \to p$, $n(\mathbf{r}) \to 0$ as $r \to \infty$, where p is a constant. The computed pressure need not tend to zero, as the integration constant, $P_0 = -p$ will ensure $P(\mathbf{r}) \to 0$ as $r \to \infty$. To obtain a complete solution for $P(x, y)$ and $n(x, y)$, it is only necessary to specify the functional form of the density along the x (or y) axis: $n(x, 0)$. Density distributions of the form $n(x, 0) = n_0 \exp(-k_{spring}x^2)$ were used, as they have simple Taylor coefficients, and yield analytic solutions when $k_{abs} = 0$.

Solution surfaces of n and P' with various values of $k_{abs}I_{tot}/(3k_{spring})$ were created. Given the time it takes to create a 3D surface using the Taylor technique in Mathematica, the main diagnostic was to compare the relatively simple 1D expansions of n and P', along the x and $x = y$ axes (see figures 3.2, 3.3, 3.5, 3.6). This comparison gives an indication of the n and P' distributions' spherical symmetry, and also whether n and P converge to zero along both the 1D paths. If n and P' don't tend to zero along both x and $x = y$ axes, then the solution will be unphysical.

Another diagnostic involved the 1D Taylor co-efficients along the x and $x = y$ axes. The form of n along both these lines is:

$$n(x, 0) \text{ or } n(x, x) = \sum_{i=0}^{\infty} a_i x^i.$$

A series of this form converges when the limit of $|a_{i+1}x/a_i|$, as $i \to \infty$, is less than one. The Taylor series radius of convergence can be approximated by the average of the function $|a_i/a_{i+1}|$, at high i values (figures 3.4, 3.7).

Conclusions

The graphs in figures 3.5, 3.6 show that solutions to equation 3.15 do appear to exist, at least within a finite domain, when the absorptive force is present, and that the solutions are approximately spherically symmetric. The Taylor expansions of n and P' converge, and obey equation 3.16, within a finite domain, much like the expansion of $\frac{1}{1-x}$. The solutions for n might in fact still exist beyond the region in which the Taylor expansion converges, again like $\frac{1}{1-x}$.

The diverging nature of the solution seen in figure 3.5 does not appear to be due numerical errors from truncation of the Taylor series.Increasing the Taylor expansion order by a factor of two does not significantly change the solution—a sign that the Taylor series has probably reached its radius of convergence.

Because of the finite reach of the n and P functions, it is impossible to tell whether they tend to zero along the x and $x = y$ axes when $r \to \infty$. Thus no definitive answer to whether physical solution surfaces to equation 3.15 exist has been obtained, however the solutions are more promising than their $\boldsymbol{\nabla} T = \mathbf{0}$ counterparts. If physical solutions do not exist with the given Gaussian initial data curves, it is still possible that physical n and P distributions would result from other $n(x, 0)$ functions.

An important point to remember is that the n solutions derived here only exist on a 2D plane through the centre of the MOT. It may not be possible to find physical solutions in three dimensions, or if the effects of the reradiation force are included.

If a more complete solution surface exists past the Taylor convergence radius, it could be obtained by several techniques. One possible technique is to take a Taylor expansion about another point close to the edge of the existing Taylor domain, extending the function. This would be quite difficult however! Another possibility is to include the reradiation force in the description again, and consider the whole system of three forces in the MOT. Perhaps self-consistency PDE solving techniques, similar to the ones used to solve the wavefunction of $Z > 1$ atoms, could be applied to the equations. The MOT and wavefunction problems are similar in that they both model complicated N-body systems. Once again this technique would be difficult, and outside the scope of this thesis. The technique, or perhaps an extension of the MC (subsection 3.2.2), may be necessary to properly test the existence of a 3D n solution however.

The results of such a test would perhaps guide future research on this topic. Solutions do not appear to exist when $\boldsymbol{\nabla} T = \mathbf{0}$, and if physical solutions still do not exist when T is allowed to vary, then there must be some form of problem in the theoretical description. The ideal gas law, used in the theory, may break down, as an ideal gas describes molecules which exert forces on each other only during collisions.

The non-conservative nature of F_{abs}, predicted by the theory, leads to the conclusion that atoms travelling between two distinct points within a MOT will require different amounts of energy for the trip, depending on their route between the two points. The mechanism by which a MOT is loaded might then have an effect on the atomic distribution. Other time-dependent effects may also occur.

A simple, and perhaps insightful technique for finding n solutions would be to make some sort of approximation for the absorptive force. By removing its non-conservative nature, easy n solutions result and will be considered in the next subsection.

3.1.4   Combining Forces

In the previous subsection it became clear that solutions to the equations of motion governing a MOT are extremely difficult to solve, even using computational techniques. This subsection will deal with approximations that can be made in order to find quick solutions, that are in essence one dimensional and relatively easy to generate.

¿From the relations:

$$\boldsymbol{\nabla} \cdot \mathbf{F}_{abs} = -k_{abs} I_{tot} n(\mathbf{r}),$$

$$\boldsymbol{\nabla} \cdot \mathbf{F}_{rerad} \approx k_{rerad} I_{tot} n(\mathbf{r}),$$

it is clear that $\mathbf{F}_{abs}$ and $\mathbf{F}_{rerad}$ have quite similar effects—except in opposite directions. An approximation for $\mathbf{F}_{abs}$ (that will hopefully retain all the relevant physics) can be given by:

$$\mathbf{F}_{abs} \approx -(k_{abs}/k_{rerad})\mathbf{F}_{rerad} = -(\sigma_L/\sigma_R)\mathbf{F}_{rerad}, \tag{3.21}$$

which has the same gradient as the full force. The total force on an atom now has the approximate value

$$\mathbf{F}_{tot} \approx -k_{spring}\mathbf{r} + (1 - (k_{abs}/k_{rerad}))\,\mathbf{F}_{rerad},$$

note that $\mathbf{F}_{abs}$ has been removed from the problem, by modifying the strength of the reradiation force. Estimates for σ_L and σ_R can be found in refs. [65], [74].

If the absorptive force is eliminated, then only the trapping and reradiation forces remain, and the solution has spherical symmetry. The trapping force by itself will create a spherical atomic cloud distribution, and adding the reradiation force expands the cloud, without breaking the spherical symmetry. It is easy to show (cf. equation 3.5) that for a spherically symmetric atomic distribution, $n(r)$, the total force can be transformed to:

$$F_{tot}(r) = -k_{spring}r + (k_{rerad} - k_{abs})I_{tot}\frac{\int_0^r n(u)u^2 du}{r^2},$$

if the absorptive force is eliminated. The 'combination' force $\mathbf{F}_{comb} = (1 - k_{abs}/k_{rerad})\mathbf{F}_{rerad}$ depends on the constant $k_2 = k_{rerad} - k_{abs}$, and $k_2 > 0$ in most circumstances [65], [74].

The form of equation 3.15 in spherical polars is:

$$\frac{dP(r)}{dr} = k_B \frac{d\,(n(r)T(r))}{dr} = \left(-k_{spring}r + (k_{rerad} - k_{abs})I_{tot}\frac{\int_0^r n(u)u^2 du}{r^2}\right)n(r). \tag{3.22}$$

Given any function $n(r)$ for the atomic number density in the MOT, a corresponding pressure function $P(r)$ can be found, subject to an integration constant. The pressure is found by integrating the RHS of equation 3.22. Only *one* integration constant will yield a physical pressure, and therefore temperature, for the MOT. The restriction $P(r) \to 0$ as $r \to \infty$ means that the pressure (incorporating the appropriate integration constant) is given by:

$$P(r) = k_B n(r)T(r) = \int_\infty^r \left(-ku + k_2 I_{tot}\frac{\int_0^u n(r')(r')^2 dr'}{cu^2}\right)n(u)\,du. \tag{3.23}$$

The solutions of equation 3.23 can be contrasted with the spherically symmetric n solutions in the $\nabla T = \mathbf{0}$ regime. An equation for the density in a constant temperature ($T = T_0$) MOT can be obtained by differentiating equation 3.22:

$$k_B T_0 \left(n''(r) - \frac{1}{n(r)}(n'(r))^2 + \frac{2}{r}n'(r)\right)/n(r) = -3k_{spring} + k_2 I_{tot}n(r). \tag{3.24}$$

The additional parameters $n'(0)$ and $n(0)$ are required before a solution can be found. Due to radial symmetry $n'(0) = 0$, and defining $n(0)$ will then uniquely specify a solution. It was shown in subsection 3.1.2 that $\nabla T = \mathbf{0}$ distributions apparently had no physical n distributions, so any results of equation 3.24 may be inaccurate.

When the temperature is assumed constant (equation 3.24), it is necessary to specify a temperature, T_0, and central density, $n(0)$, in order to obtain a solution for $n(r)$. If the temperature is allowed to vary then, although more information about n is required ($n(r)$ must be specified for all r), the temperature, $T(r)$, is then determined without requiring $T(0)$.

Solutions to equation 3.24 only exist when $n(0) < n_{max} = 3k_{spring}/(k_2 I_{tot})$ [65], otherwise the combination force dominates the trapping force at the centre of the distribution—the forces cannot reach equilibrium. When $n(0) \to n_{max}$ the n distribution increases in width, allowing more atoms to enter the distribution, whilst retaining the same maximum density n_{max}. This can be contrasted with the $k_2 I_{tot} = 0$ (temperature limited [74]) regime, where the width of the n distribution remains constant, as N increases.

As the number of atoms increases and $n(0) \to n_{max}$ the distribution ceases to be Gaussian, and behaves like a heavyside function of height n_{max} and width $\left(\frac{3N}{4\pi n_{max}}\right)^{1/3}$. The distributions in figure 3.8 depict typical $n(r)$ functions when $\boldsymbol{\nabla} T = \boldsymbol{0}$. A convolution is necessary to obtain the probability distribution in cylindrical polars, i.e. in the form it would be observed experimentally. The cylindrical convolutions of the spherical distributions have narrower widths and are more Gaussian.
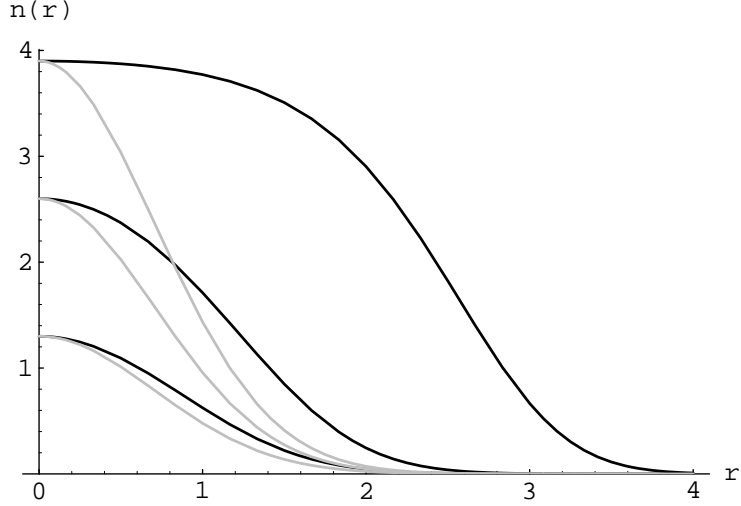

Figure 3.8: Spherically symmetric solutions (black) at constant $T = T_0$ when $k_B T_0 = 1$, $k_2 I_{tot} = 1.5$, $k_{spring} = 2$ ($n_{max} = 4$) for $n_0 = 1.3, 2.6, 3.9$ with the corresponding (grey) solutions in the $k_2 = 0$ temperature-limited regime.

The parameter n_{max} is frequently used to describe the limiting density in a MOT [65], [71], [74]. If the temperature is allowed to vary across the MOT however, solutions are no longer restricted by the $n(0) < n_{max}$ criterion. Pressures and temperatures with maxima at constant, non-zero spherical radii, rather than the point $r = 0$; i.e. 'hollow' atomic distributions are possible. The temperature distributions in the $\boldsymbol{\nabla} T \neq \boldsymbol{0}$ regime, arising from Gaussian $n(r)$ distributions, are usually approximately constant, unless the central density, $n(0)$, approaches n_{max}.

Equation 3.24 can be re-arranged to the form:

$$\frac{k_B T_0}{3 k_{spring}} \left(n''(r) - \frac{1}{n(r)} (n'(r))^2 + \frac{2}{r} n'(r) \right) / n(r) = -1 + n(r)/n_{max}. \tag{3.25}$$

It is easy to show that if n_{max} changes to $a\, n_{max}$ where a is a constant, then if $n(r)$ is a solution to the original differential equation 3.24, $an(r)$ is a solution to the modified equation. Also if the solution of equation 3.25, $n(r)$, is known for a given value of T_0/k_{spring}, then (when $n(0)/n_{max} = an(0)/(an_{max})$ is fixed) the solution with parameter T_0'/k_{spring}' is given by $a\, n\left(\sqrt{T_0 k_{spring}'/(T_0' k_{spring})} r\right)$. Note that if the initial distribution contains N atoms, then the second distribution will contain $a\left(T_0' k_{spring}/(T_0 k_{spring}')\right)^{3/2} N$ atoms.

Atomic distributions, with the same value of $n(0)/n_{max}$, therefore have the same 'shape' when their dimensions are scaled. A good parameter for the 'shape' of a $\boldsymbol{\nabla} T = \boldsymbol{0}$ MOT is therefore $\eta = n(0)/n_{max}$, and if this parameter is constant then the parameter $\epsilon = N(k_{spring}/T_0)^{3/2}$ gives an indication of changes in the absolute sizes of $n(0)$ and n_{max}. As η increases toward one, the atomic distribution becomes flatter, and closer to the n_{max} limit.

The important thing to note from these relationships is that as T_0 increases, a larger number of atoms, N, is required before the density reaches the 'flat' regime seen in figure 3.8. The number and temperature of atoms in a MOT is very much dependent on the parameters of the trap [44], and therefore as these parameters vary the maximum value of the density, $n(0)$, in a MOT will vary relative to n_{max}. In contrast,

the theoretical maximum density in a MOT, n_{max}, has no dependence on T or N. Experiments measuring the maximum density in a MOT should therefore measure η rather than assume $\eta \approx 1$.

This could well be the reason why Townsend *et al.* [74] did not observe a MOT governed by n_{max} in their experiments. They observed Gaussian distributions, which suggests that η was low, and the distributions were inside, or near, the temperature limited regime. Another possibility is that the temperature in the MOT varied with position. In this regime it is possible for the distribution to be Gaussian (or in fact any other shape) and the temperature in the MOT adjusts accordingly—even if $n(0) \rightarrow n_{max}$ or $n(0) > n_{max}$. The temperature should increase radially for Gaussian-shaped MOTs with $k_2 I_{tot} > 0$, according to the theory developed here, and this could have something to do with the observed temperature rise in a MOT with increasing N.

The temperature increase with N was explained in ref. [14]. The explanation used the relationship $T = D/\alpha$ (cf. equation 2.15) where D is the diffusion constant of the MOT, and is proportional to the absorption rate. From subsection 2.2.3 it was shown that two processes contribute to the diffusion: spontaneous emission, and absorption from the lasers. The diffusion term can therefore be considered as $D = D_{spon} + D_{laser}$. Cooper *et al.* [14] noted that if reradiated photons are absorbed by some of the atoms, then these photons will increase the total rate of absorption, whilst making no contribution to the total damping constant, α. The probability of reradiated photon absorption increases with the number of atoms, so D, and therefore T, increase with N. Experimental results verified Cooper *et al.*'s theory that $N^{1/3} \propto T - T_{mol}$, where T_{mol} is the low-N atomic density. The theory relied on the atoms in the MOT maintaining a fixed density as N increased.

It appears that the temperature increase may also be seen using equation 3.23. If $n(r)$ distributions reach a maximum density, then as N increases the atomic distribution becomes wider, and the atoms reach higher radii. Gaussian $n(r)$ distributions, with increasing widths, yield a radially increasing temperature function. Distributions with high N therefore acquire a higher mean temperature.

Experimentally obtained n distributions could be used to test the theories which have been developed here. By convolving the image of the trap, it would be possible to get an approximate relative spherical density distribution. To get the absolute density, n, it would also be necessary to measure the total number of atoms, N. Once an approximate function for $n(r)$ has been obtained it would be possible to predict $T(r)$. The theoretical temperature distribution could be compared with an experimental time of flight (TOF) temperature measurement. If the temperature varies with position then the velocity distribution will be a convolution of different Boltzmann distributions originating from different points in space.

If the TOF measurement is made at a distance from the MOT, then the atoms can be approximated as a point source, removing some of the space dependence from the convolution. A value for the average temperature in the MOT can be obtained by:

$$\overline{T} = \frac{\int_0^\infty n(r) T(r) \, r^2 dr}{\int_0^\infty n(r) \, r^2 dr},$$

and would probably give the closest Boltzmann fit to the convolution. This convolution of Boltzmanns could in fact help explain some of the experimentally observed non-Boltzmann temperature distributions.

The main points to check are therefore whether the temperature is position dependent, and also whether the density is limited by the 'maximum density', n_{max}, derived above. It will also be of interest to compare the numerical predictions of Cooper *et al.* [14] with the temperature/density behaviour of the model shown here.

Extensions of the density n into phase-space density, similar to those in ref. [74], would be relevant to the area of MOTs used as precursors to BEC.

3.2 Rings and Things

3.2.1 Rings with Balls

In 1990 Walker *et al.* [76] observed interesting structures within a MOT if the laser beams were misaligned in such a way as to produce a torque on the atoms. As well as the typical central ball distribution of a MOT, they also saw a ring structure or a rotating clump of atoms that developed around a central atomic ball. To explain this effect they used the reradiation force, of the previous section. A more detailed theory was described in a subsequent paper by the same authors [65].

Succeeding papers discovered rings without central balls [7], and double ring structures [3]. The purpose of this section is to attempt to improve the theory used in the description of these structures, as the models presently used are often applied outside the domain in which they are accurate. Some finer details will also be applied to the theory, adding more information to the atomic distribution than has been seen previously.

Firstly it will be necessary to describe the notation used, as this varies between authors. The notation used here will be similar to that of Bagnato *et al.* [7], and the Rabi frequency Ω is defined $I/I_S = 2\Omega^2/\Gamma^2$. In order to apply a torque to the atoms, a beam misalignment in the horizontal (xy) plane is applied—the geometry is shown in figure 3.9.
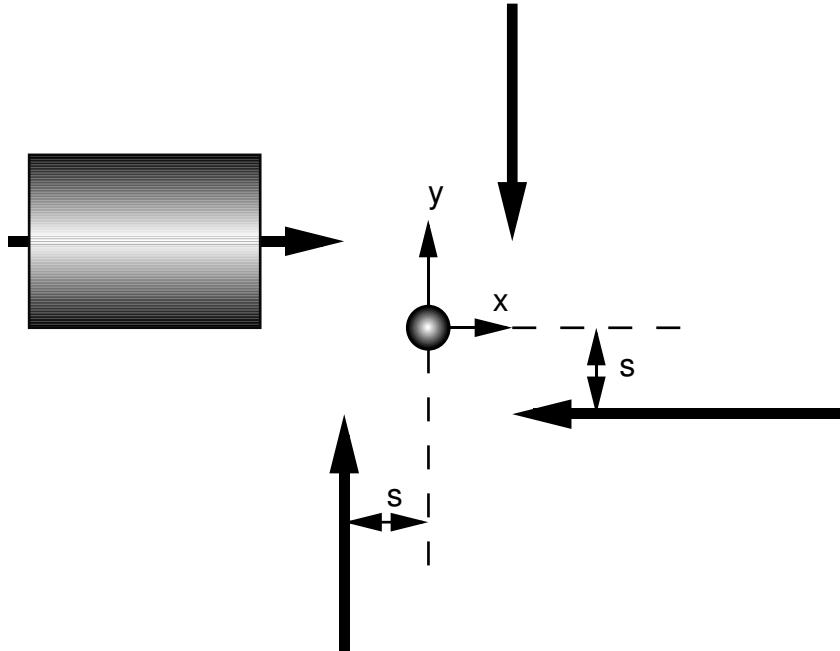

Figure 3.9: The symmetric beam misalignment typically used to create orbital modes in a MOT. The bold arrows indicate the axes, and direction of propagation, of the four Gaussian laser beams in the $z = 0$ plane. The z beams necessary for confinement in the z direction are not shown.

The distance s gives a quantitative measure of the beam misalignment and is an important parameter in determining the ring shape etc. Sesko *et al.* [65] use $s/2$ instead of s. The width of the Gaussian laser beam profiles is another important parameter. Sesko *et al.* [65] used the variable, w, for the FWHM of the beam profile, however Bagnato *et al.* [7] and de Araujo *et al.* [3] use w to describe an intensity variation of the form $I = I_0 e^{-r^2/w^2}$. This definition has been adopted here, although this width parameter, w, is different from the 'waist' often used to describe laser beam widths in laser physics (and used in ref. [29]). The two parameters are related by the equation: waist $= \sqrt{2}w$.

Various methods have been used to predict atomic orbits in the MOT based on the intensities, beam widths, s value and magnetic field gradients in the MOT. One technique is to consider a radial slice through the laser beam configuration (e.g. the x axis) and consider the centripetal and trapping forces acting on the

atom as a function of the radius from the origin. By finding a radius where the force is zero, but restoring on either side of this radius, the equilibrium radii about which atoms orbit can be found. Another method is to find the complete position dependent forces acting on the atoms in two dimensions, and solve for the stable atomic orbits numerically.

The reason only two dimensions are considered is that the *average* force on the atoms is considered and the fluctuating heating term is omitted—i.e. there is no diffusion included in the models used in previous papers. If the average force is applied, and the two z beams have equal intensity, then because of the symmetry of the beam arrangement, the atoms will be trapped in the $z = 0$ plane. With the Monte Carlo (MC) program developed earlier it will be possible to get 3D velocity and position distributions rather than just the 2D mean velocities and paths of the atoms.

For the meantime, however, the analytic 1D approach will be used, as it is faster than the computational 3D MC technique. This analytic theory will be used to choose suitable parameters for MC simulations. A final point to consider before embarking on this course is the effect of saturation on the atoms. This was considered in subsection 2.2.2, where two different methods of dealing with saturation were mentioned. The first method was used in [7], but the second method was used in [65] (without specifying the z laser beam geometry), [29] (omitting position dependence of I_{tot}), [3] (where very little detail of the model is given) and will also be used here. The total intensity in the MC is position dependent, and so this dependence was included in the analytic model, to enable the two techniques to relate well. Controlling the z beam laser geometry can affect the trap geometry, and this is another good reason to allow the total intensity to be position dependent.

The 1D analytic case along the x axis will now be considered. As the average force on the atoms is in the $z = 0$ plane, only the average forces applied by the x and y beams are needed to determine the average force acting on atoms. The four xy laser beams have intensities which vary according to $\frac{I(\mathbf{r})}{I_S} = \frac{I_0}{I_S}e^{-\rho^2/w^2} = \frac{2\Omega_0^2}{\Gamma^2}e^{-\rho^2/w^2}$, where $\rho(\mathbf{r})$ is the radial distance from a laser beam's axis of propagation.

On the x axis, the force from the laser beam travelling in the $+x$ direction is given by (equation 2.1 with $y = z = 0$ and modified intensities/saturation):

$$F_x = \frac{\hbar k_L \Gamma}{2} \frac{2\Omega_0^2 e^{-s^2/w^2}/\Gamma^2}{1 + I_{tot}(\mathbf{r})/I_S + (\frac{2}{\Gamma})^2(\Delta - k_L v_x - \omega_B bx)^2}.$$

Radially stable orbits passing through the x axis will have $F_x = 0$ and $v_x = 0$, and therefore $v_x = 0$ can be substituted into this equation, further simplifying it to a solely position dependent force. The force from the $-x$ beam can be derived similarly, and the two x beams create a total trapping force in the x direction

$$
\begin{aligned}
F_x &= \frac{\hbar k_L \Omega_0^2 e^{-s^2/w^2}}{\Gamma} \left(\frac{1}{1 + I_{tot}(\mathbf{r})/I_S + (\frac{2}{\Gamma})^2(\Delta - \omega_B bx)^2} - \frac{1}{1 + I_{tot}(\mathbf{r})/I_S + (\frac{2}{\Gamma})^2(\Delta + \omega_B bx)^2} \right) \\
&= F_{trap}.
\end{aligned}
\tag{3.26}
$$

The e^{-s^2/w^2} exponential factor in equation 3.26 occurs because the laser beam axes are offset from the x axis. This effect was not taken into account in ref. [7]: the on-axis laser intensities were used throughout. Bagnato *et al.* approximated the trapping force, F_{trap}, using the Taylor expansion demonstrated in section 2.2. The linear approximation for the force is $F_{trap} \approx -\beta x$ where

$$\beta = \frac{-16\hbar k_L \Omega_0^2}{\Gamma^2} \frac{e^{-s^2/w^2}\Delta/\Gamma}{\left(1 + I_{tot}(\mathbf{0})/I_S + (\frac{2\Delta}{\Gamma})^2\right)^2}\omega_B b$$

(i.e. equation (2) of ref. [7] with an exponential correcting term). Note that ref. [7] uses k to refer to $1/\lambda$ rather than $2\pi/\lambda$.

Due to the intensity variation of the y beams along the x axis, the atoms will be accelerated to various non-zero y velocities, depending on their x position. The average force on an atom at x on the x axis, due to the laser beams travelling in the $\pm y$ directions is:

$$F_y = \frac{\hbar k_L \Omega_0^2}{\Gamma} \left(\frac{e^{-(x+s)^2/w^2}}{1 + I_{tot}(\mathbf{r})/I_S + (\frac{2}{\Gamma})^2(\Delta - k_L v_y)^2} - \frac{e^{-(x-s)^2/w^2}}{1 + I_{tot}(\mathbf{r})/I_S + (\frac{2}{\Gamma})^2(\Delta + k_L v_y)^2} \right).
\tag{3.27}$$

In subsection 2.2.6 it was shown that the equilibrium velocity, obtained by atoms subject to an intensity imbalance, can be found using either a linear approximation, or an exact quadratic calculation. In both cases the intensity ratio of the two y laser beams,

$$i(x) = I_{y^+}/I_{y^-} = e^{-(4xs)/w^2},$$

is a helpful parameter.

The force in equation 3.27 can be approximated (near $x = 0$) to $F_y \approx F_0 - \alpha v_y$, where:

$$F_0(x) = F_y(v_y = 0) = \frac{\hbar k_L \Omega_0{}^2}{\Gamma} \left(\frac{e^{-(x+s)^2/w^2}}{1 + I_{tot}(\mathbf{r})/I_S + (\frac{2\Delta}{\Gamma})^2} - \frac{e^{-(x-s)^2/w^2}}{1 + I_{tot}(\mathbf{r})/I_S + (\frac{2\Delta}{\Gamma})^2} \right)$$

and $\alpha = \beta k_L/(\omega_B b)$. Equation (3) of Bagnato et. al [7] appears to have a mistake—their α is too strong, by a factor of 2π (this error was corrected in ref. [29]). The value for α used above has been modified from ref. [7] to include an exponential term, in the same manner as β was modified.

The equilibrium y velocity can be approximated as $v_{y_0}(x) \approx F_0(x)/\alpha$, as in ref. [7], or it can be obtained by the quadratic solution (cf. equation 2.26):

$$v_{y_0}(x) = \frac{-\Delta(i(x)+1)}{k_L(i(x)-1)} \left(1 - \sqrt{1 - \left(1 + (1 + I_{tot}(\mathbf{r})/I_S)\frac{\Gamma^2}{4\Delta^2}\right) \frac{(i(x)-1)^2}{(i(x)+1)^2}} \right). \tag{3.28}$$

As the damping force in a MOT is much shorter than the restoring force, it is possible to assume that the atoms accelerate rapidly to their equilibrium velocities with negligible change in position (i.e. they stay near the x axis while the equations are applied). The equilibrium y velocity of the atoms means that a centripetal force of magnitude $F_{cent} = mv_y{}^2/x$ must be applied if the atom are to stay at the same radius. Atoms are trapped in stable orbits at radius r when $\mathbf{F}_{trap}(r) + \mathbf{F}_{cent}(r) = 0$. The additional behaviour: $\mathbf{F}_{trap}(x) + \mathbf{F}_{cent}(x) < 0$ for $r < x < r_{max}$ and $\mathbf{F}_{trap}(x) + \mathbf{F}_{cent}(x) > 0$ for $0 < r_{min} < x < r$ is also required, where r_{min}, r_{max} are constants that denote the boundaries of a stable orbit's trapping range.

Instead of comparing the forces, it can be more convenient to compare their associated velocities, i.e. $v_{cent}(x) = |v_{y_0}| = \sqrt{|x\,\mathbf{F}_{cent}(x)/m|}$ and the 'trapping velocity' $v_{trap}(x) = \sqrt{|x\,\mathbf{F}_{trap}(x)/m|}$. A stable orbit occurs at radius r when $v_{diff}(r) = v_{trap}(r) - v_{cent}(r) = 0$. When $v_{diff}(x) > 0$ the net force on an atom is radially inward, and when $v_{diff}(x) < 0$ the converse is true. The form of these velocities will allow comparison with the figures of Bagnato $et\ al.$ [7].

One remaining point is necessary before calculating the theoretical forces, and that is to set a value for $I_{tot}(\mathbf{r})/I_S$. As only the x axis is under consideration, the total intensity is given by:

$$I_{tot}(\mathbf{r})/I_S = I_{tot}(x)/I_S = (I_{x^+}(x) + I_{x^-}(x) + I_{y^+}(x) + I_{y^-}(x) + I_{z^+}(x) + I_{z^-}(x))/I_S.$$

Because $\frac{I_{x^+}(x)}{I_S} = \frac{I_{x^-}(x)}{I_S} = \frac{2\Omega_0{}^2}{\Gamma^2}e^{-s^2/w^2}$, $\frac{I_{y^+}(x)}{I_S} = \frac{2\Omega_0{}^2}{\Gamma^2}e^{-(x+s)^2/w^2}$ and $\frac{I_{y^-}(x)}{I_S} = \frac{2\Omega_0{}^2}{\Gamma^2}e^{-(x-s)^2/w^2}$, it is only necessary to determine the functional behaviour of $\frac{I_{z^+}(x)}{I_S}$, $\frac{I_{z^-}(x)}{I_S}$. The z laser beams may well require different waists to the xy beams, in order to provide z confinement for atoms orbiting at large radii. The intensity may differ due to the change in waist, so the form

$$\frac{I_{z^+}(x)}{I_S} = \frac{I_{z^-}(x)}{I_S} = \frac{2\Omega_z{}^2}{\Gamma^2}e^{-x^2/w_z{}^2}$$

will be adopted for the z beams. The Gaussian z beams will be centred on the z axes for symmetry.

The two 1D theories for v_{trap}, v_{cent}, will now be compared with the more accurate 3D Monte Carlo simulation. The width parameter $w = 1$cm has been used in all of the simulations. The distance variables s, x can be changed to the 'dimensionless' x/w and s/w—however care must be taken when adjusting the trapping velocity, $\mathbf{v}_{trap}$, which scales as w. The figures 3.10, 3.11, 3.12, 3.13 all pertain to properties of a MOT in which $s = 1.2$cm ($s/w = 1.2$), $b = 15$G/cm, $\Delta/\Gamma = -2$, $I_0/I_S = 0.3$ ($\Omega_0 = \sqrt{0.15}\Gamma$), $\Omega_z = 0.5\Omega_0$ and $w_z = \infty$ (i.e. the z beams have 'flat' intensity profiles).

In the figures the grey curves correspond to the modified equations of Bagnato *et al.* [7], described above. The equations differ from ref. [7] by an exponential factor, and the form of I_{tot} used. The black curves in the figures correspond to the more exact versions of v_{cent} and v_{trap} derived from equations 3.28, 3.26.
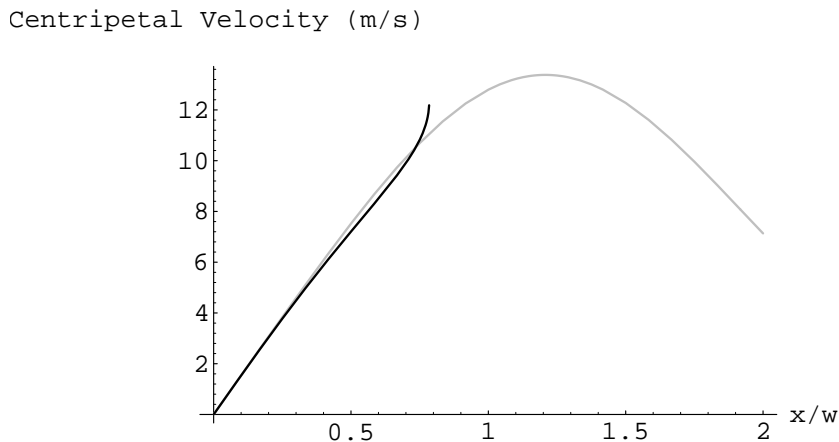
Centripetal Velocity (m/s)

Figure 3.10: A comparison of the approximate (grey) and more exact (black) calculations for the centripetal equilibrium velocity v_{cent}.
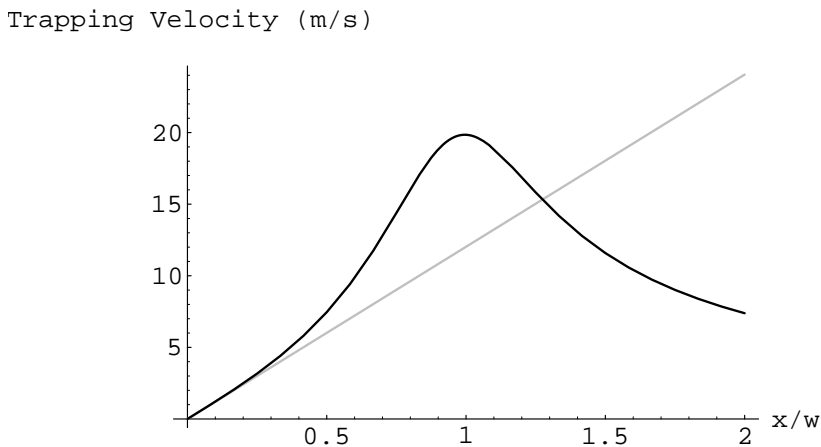
Trapping Velocity (m/s)

Figure 3.11: The same comparison for v_{trap}.

From figures 3.12, 3.13, it can be seen that the modified equations of ref. [7] do not give a very accurate prediction of where a ring will form in the MOT. The ring radius predicted by this theory is very different from the radius of the complete 3D MC solution for the same trap parameters. The more exact 1D non-linear equations developed here give better agreement with the MC, but still have a small error (which was expected, because the equations were obtained by simplifying a 2D problem). The unmodified equations of Bagnato *et al.* [7], where the e^{-s^2/w^2} factor was omitted, predict the trapping force is so strong that *no* ring should form, and the atoms should all accumulate near the origin. The two analytic theories developed here will agree if a ring is predicted near $x = 0$, as the linear Taylor expansions of the theories, at $x = 0$, are the same.

The difference between the two approximations for v_{cent} at high x/w is extremely large for most values of s/w. In fact, the more exact 1D calculation of v_{cent} in figure 3.10 shows that there are often regions
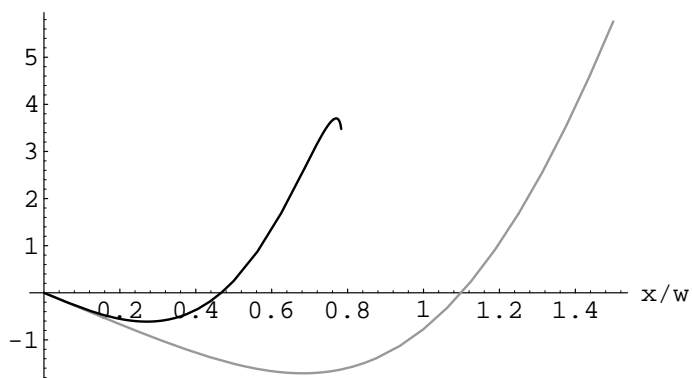
Difference Velocity (m/s)

Figure 3.12: The difference velocity $v_{diff} = v_{trap} - v_{cent}$ predicted by the two theories. The approximate 1D theory predicts that a ring will occur at $x = 11$mm, whereas the more exact 1D theory predicts a ring at $x = 4.6$mm.
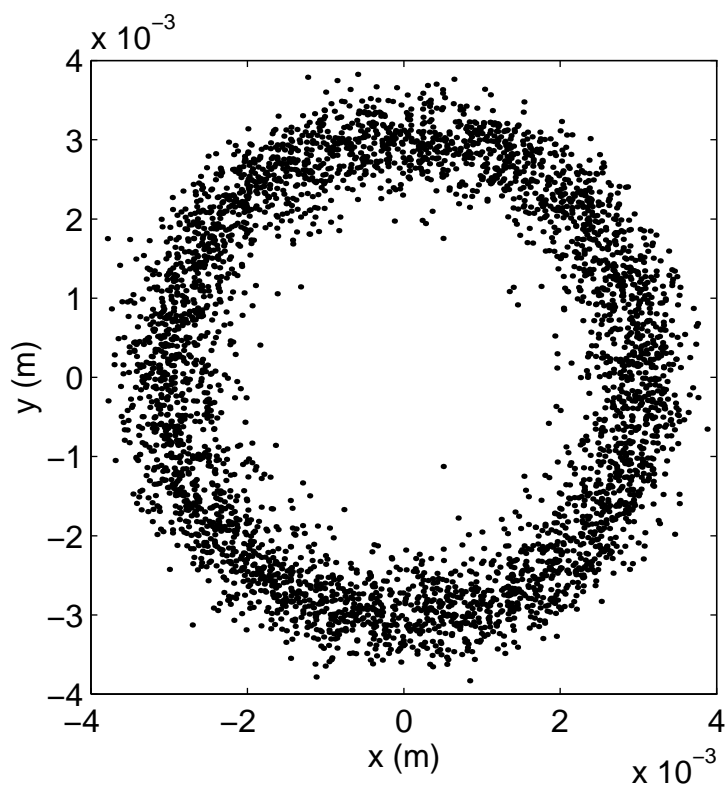

Figure 3.13: A collection of atomic distributions in the xy plane. The MC models 100 atoms released into the origin of a MOT, then allowed to reach equilibrium. The image is a conglomerate of 'snapshots' from various times. The ring radius is $r \approx 3$mm.

where the intensity imbalance is so high that no equilibrium velocity exists—atoms will accelerate out of the MOT in these regions. The bell shape of the approximate v_{cent} was a crucial step toward finding rings with central balls in ref. [7], however a bell shape is difficult to obtain using v_{cent} from equation 3.28, which is typically linear and of finite extent.

Problems in the Theory

The curvature of the more exact trapping and centripetal velocities imply that it will be difficult, if not impossible, to obtain a situation where a ring will form with a central core: i.e. a regime where the trapping force dominates near $x = 0$ and at large x, with an intermediate x region in which the centripetal force dominates. Solutions may still exist for the MC, even if the 1D theory predicts otherwise (e.g. a weak trapping force on the x axis may be counteracted by a stronger force on the $x = y$ axis), however the more likely possibility is that the present Doppler theory alone will not create rings with central cores.

Thus while it is relatively easy to obtain laser configurations that give ring-shaped distributions, using the two analytic theories or the MC, it is much more difficult to find rings with a central core of atoms in these models. The analytic theory developed in ref. [7] predicted such structures existed, and they obtained 2D examples using a numerical situation based on six Gaussian beams. The details of the method were omitted, and so comparison is difficult.

Two explanations why theoretical ring+ball configurations don't exist are suggested here—either sub-Doppler theory of the MOT [71] needs to be introduced (unlikely, due to the high intensities, and intensity imbalances involved), or some other effect may be causing the central cores to form inside rings.

Sesko *et al.* [65] suggested that the reradiation force was causing these objects to form. The paper by Bagnato *et al.* [7] attempted to show that the formation of rings, both with and without central atomic cores, could be explained even if reradiation was omitted. High intensities and low detunings were necessary to obtain the ring+ball configuration in both the theoretical and experimental situations, however. The reradiation force is linearly proportional to intensity, and low detunings tend to load more atoms into a trap. As the reradiation force also increases with N, then both the detuning and intensity changes suggest that experimentally observed ring+ball configurations occur when the reradiation force is relatively large.

Another point suggesting that the ring+ball configuration is due to the reradiation force is that the theory used both here and in refs. [7], [3] becomes inaccurate at high intensities. The intensity needs to be set high to explain the appearance of the ring+ball configuration, however the equations should only be used when $2\Omega_0{}^2/\Gamma^2 < 1$ [28], [43]. In refs. [7], [3] this parameter often needs to be set to values of 288 or more in order to obtain a theoretical ring+ball distribution. Even if the theory was valid at such high intensities, the reradiation force would certainly be evident and need to be considered in the description.

A paper by Guedes *et al.* [29] showed that it is possible to experimentally obtain rings with radii that do not depend on N and hence do not depend on reradiation. The theory used to explain the experimentally observed radii was similar to ref. [7], and had a reasonably close agreement to experiment—this suggests that Doppler theory is quite adequate to describe a ring MOT, at least in the low N regime. It is therefore possible to explain rings without reradiation, however a similar test has not been done for the ring+ball configuration. In fact the theoretical parameters necessary (if reradiation is omitted) to explain the observed ring+ball and double ring configurations are often quite different from the experimental parameters [3], [7].

De Araujo *et al.* [3] used a theoretical model with $2\Omega_0{}^2/\Gamma^2 = 338$ to explain their experimentally observed double ring structure. The relationship of v_{trap} and v_{cent} in ref. [3] implied that an outer ring should form, but that the trapping force for the internal ring would be very weak. With such a weak force holding the atoms into the unstable inner orbit, then if diffusion were included in the model it is highly likely that atoms could 'boil off' from the internal ring. The internal ring would have a much lower population than the external ring (which is not experimentally observed). Also of note is the form of the theoretical total force used in equation (1) of ref. [3]. Although the damping and trapping forces are position

dependent, an improvement on the constant values in ref. [7], they are constrained to be radial. The force on an atom is not radial, however non-radial components could have been included in the vortex force as the exact nature of this force is not given.

It is the opinion of the author that ring+ball and double ring configurations (when $2\Omega_0^2/\Gamma^2 < 1$) can only be explained if the reradiation force is considered. It would be of interest to check that this is the case when one studies the realm where $2\Omega_0^2/\Gamma^2 > 1$, however a theory which encompasses this area would have to be developed first. Such a theory would deal with high intensities and should probably include the reradiation force anyway.

3.2.2 Adding Reradiation

The notation of Sesko *et al.* will be adopted here. In a MOT configuration with a ring and central core, the total number of atoms is N. The fractions of atoms in the ring and core respectively are η_r and η_c. The ring of atoms is at a radius r from the central core of atoms, as seen in figure 3.14.
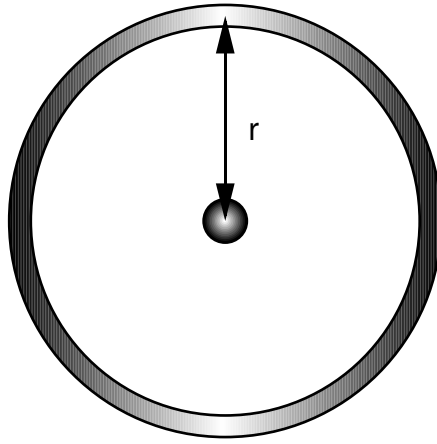

Figure 3.14: The geometry of a ring distribution with a central core of atoms. The ring contains $\eta_r N$ atoms, whilst the core contains $\eta_c N$.

The magnitude of the reradiation force on the outer ring of atoms, due to the central core, is given by (cf. equation 3.3):

$$F = \frac{\alpha \eta_c N}{r^2},$$

where $\alpha = \sigma_R \sigma_L I_{tot}/(4\pi c)$ and I_{tot} is the total intensity of the light incident on the core atoms. The force is radially outwards. There is also a reradiation force on the ring atoms due to the ring atoms themselves, as the reradiation force on a single atom is given by the sum of the reradiation forces of all surrounding atoms.

Sesko *et al.* [65] approximated the ring atoms as $\eta_r N$ atoms uniformly spaced around a circle of radius r. It is straightforward to show that the force on a single atom, due to the reradiation force of the other $\eta_r N - 1$ atoms, is then radially outward, with magnitude:

$$F = \frac{\alpha}{4r^2} \sum_{i=1}^{\eta_r N - 1} \frac{1}{\sin\left(\frac{\pi i}{\eta_r N}\right)}.$$

This summation can be approximated to an integral, and this integral gives:

$$F \approx \frac{\eta_r N \alpha}{2\pi r^2} \ln(2\eta_r N/\pi) = F_1,$$

which was used in ref. [65]. In fact it can be shown, by the use of more accurate integration limits, that a better approximation is:

$$F \approx \frac{\eta_r N \alpha}{2\pi r^2} \ln(4\eta_r N/\pi) = F_2.$$

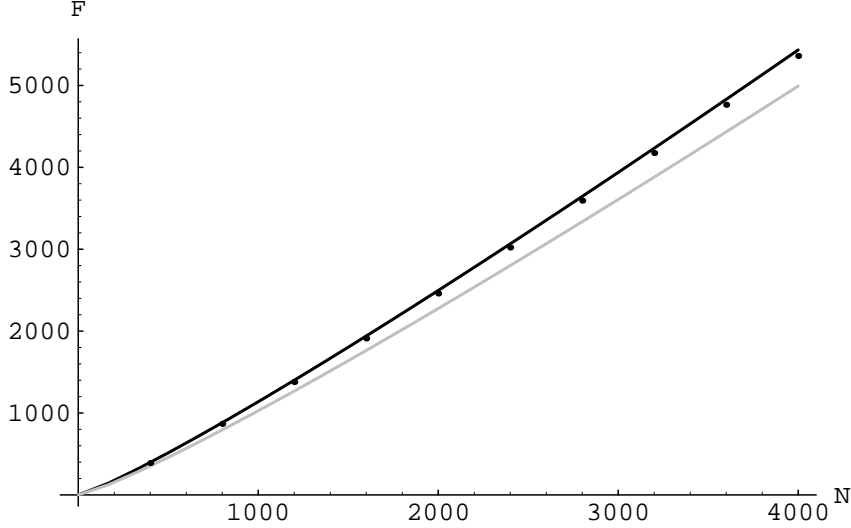The forces F, F_1 and F_2 are compared in figure 3.15.

Figure 3.15: The magnitude of the reradiation force felt by a ring atom, due to the $N-1$ other ring atoms, when the atoms are uniformly spaced around a circle. The figure shows a comparison of the exact force F (dotted) and the two approximations F_1 (grey), F_2 (black), when $\eta_r = 1$ and $\alpha/r^2 = 1$.

The relative difference between F_1 and F_2 is about 5% for $10^5 < N < 10^7$. Although this discrepancy is small, it may be worth noting. The force on an atom by its nearest neighbour, and for large N, is: $F_{nn} = \frac{\alpha \eta_r N}{4\pi r^2}$. Because $F_{nn}/F_2 = 1/(2\ln(4\eta_r N))$ is a slowly varying function of N, the nearest neighbour contribution to the total force will be quite significant, even for large N.

Consider the central core of the configuration. As the core will be at an off-axis point of the horizontal trapping laser beams (figure 3.9) it will have reduced x, y spring constants compared to a fully-aligned MOT. If a ring of atoms exists around the central core then there is another contribution to the spring constant at the core—due to the reradiation force from the ring atoms. This force appears to have been omitted in previous papers. The magnitude of the force, at a radius R from the origin, is given by:

$$F(R) = \frac{\alpha \eta_r N}{2\pi} \int_0^{2\pi} \frac{r\cos\theta - R}{(R^2 + r^2 - 2rR\cos\theta)^{3/2}} \, d\theta.$$

The direction of the force is radially inward, and the magnitude of the force can be approximated to the linear form:

$$F(R) \approx \frac{\alpha \eta_r N}{2r^2} \frac{R}{r} \qquad \text{for } R << r.$$

Possible Analytic Extensions of Section 3.1 and their Implications

When the off-axis spring constant, reradiation force from the ring, and centripetal force in the core are summed, a 'total' force acting on the central core of atoms is obtained. By making a linear approximation to this 'total force', it is possible to fit a modified spring constant k_{spring}' for the total trapping force acting at the central core. This simplification is possible because the three forces which generate the spring constant are solely position dependent, and do not depend on the density distribution of the core.

Once reradiative and absorptive forces are added to the model at the core it may be possible to extend the theory developed in section 3.1, to solve for the density distribution of the central core. The atoms in the core will rotate, as the laser beams are configured to apply a torque on the atoms. The speed the atoms acquire will depend largely on the intensity imbalances that are generated across the core. If the intensity from each beam remains relatively flat across the core, then the set-up will be very much like a typical MOT. The radial intensity gradient of the beams near the origin will therefore determine how fast the core will spin and whether the energy of this motion is comparable with the thermal energy of the distribution.

The reduced spring constant at the core will lead to a lower maximum density, as n_{max} is proportional to k_{spring} (section 3.1). This means the size of the core will grow rapidly as more atoms are added, and its size could in fact grow to an extent where the outer atoms are thrown into a ring by the increased centripetal forces. This would be one mechanism for the creation of rings with cores.

The centripetal forces from the tangential velocities of the atoms will affect the size of the distribution, but these forces will be included in k_{spring}', lowering the effective spring constant of the core. As the equilibrium velocities are tangential, not radial, they will have no further effect on the size of the distribution. This property of the tangential velocities and centripetal forces should also be true of the ring surrounding a core. In fact the ring itself should have a localised radial spring constant about the radius r, and so it should also be possible to use the results of section 3.1 on the outer ring.

In both the ring and core the spring constants in the radial and axial directions will be different, as no centripetal forces act in the z direction. This makes finding a density solution more difficult, due to anisotropy, however n solutions will still be possible using the techniques of section 3.1. It is also possible to set up the z beams with large waists, yielding intensities that are always approximately the on-axis z intensity, allowing simple approximations for the z spring constants at the ring and core.

If the ring is subject to the same forces as in section 3.1, this implies that there may be a maximum density for the ring of atoms, and also for the core. Thus when there is a sufficiently large number of atoms in the ring, the distance between the atoms will decrease to a minimum value proportional to $1/(n_{max})^{1/3}$. Modelling the atoms as uniformly distributed about a circle may therefore be unreasonable, as in such a model the distance between the atoms continues decreasing at a rate $\propto 1/N$. Another problem with the 'circle' model is that it does not allow the ring of atoms to include diffusion effects. These effects create a torus, with non-zero thickness. An atom on the *inside* of the torus will feel a force that is radially inward, unlike the radially outward force felt by atoms on the outside of the ring. This behaviour arises because most of an inner atom's nearest neighbours will exert a force that acts inward.

Another mechanism for the formation of rings with central cores may therefore be possible. 'Bowl' shaped forces similar to those shown in figure 3.12 could be formed, with near-zero force inside the stable ring radius. If the number of atoms in the initially ring-shaped distribution, or the intensity of the laser light, increase to a point where reradiation becomes important in the ring, then the atoms on the inner radius of the toroidal ring of atoms will be pushed inward. The converse is true of the outer atoms. The inner atoms will meet little resistance to moving to a lower radius, and creating a core, while the outer atoms meet the strong restoring force at the edge of the 'bowl' and remain in the ring.

Possible Extensions of the MC

To obtain a more accurate model for the atomic distribution when reradiation is included, reradiation would have to included in the MC simulation. It would be much too computer intensive to calculate the force on each atom, due to all other atoms, for every photon absorption/emission cycle. The interatomic force on a single atom has $N(N-1)/2$ contributions for each cycle, and $N > 10^6$ in a MOT. Several million time steps are necessary to create an accurate position distribution, and the interatomic force would need to re-evaluated at each step.

A simplification however, would be to split the MOT volume into several small cubes. After the atoms reach equilibrium (neglecting the reradiation/absorption forces) the reradiation and absorption forces could be applied at a single time step. The average reradiation force inside each cube could then be evaluated at that time step, for a given N, and implemented as a constant force for several more time steps. Once the atoms reach equilibrium again, the reradiation and absorption forced could be re-evaluated... this process is continued until the change in the distribution becomes negligible.

Before the implementation of a reradiative model, an MC must include diffusion effects. These effects have already been incorporated in the MC used here. Diffusion allows atoms to overcome small potential barriers, that would otherwise trap atoms. Diffusion can allow a flow of atoms between a ring and core, and

therefore give an indication of relative populations of the two structures—they need not be considered as separate entities. The position distribution of atoms in an atomic cloud is also affected by diffusion, which determines the distances between atoms, and hence the strength of the reradiation force.
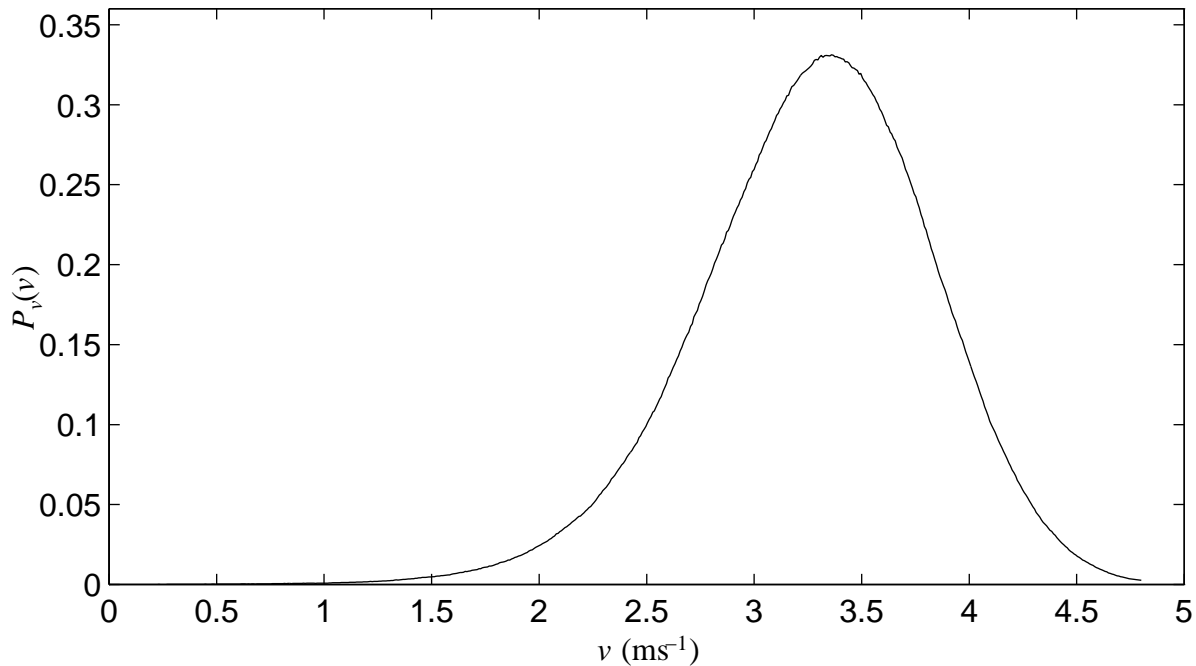

Figure 3.16: The relative probability distribution of the atomic velocity, v $(v^2 = v_x{}^2 + v_y{}^2)$, in the xy plane. The distribution was generated using the same run of the MC that created figure 3.13. Note the asymmetry of the distribution.

Previous papers have only included the average force acting on an atom, neglecting the fluctuating diffusive force. If only the average force is considered, the atoms are distributed in a 1D ring and the width of the velocity distribution cannot be found. Typical velocity distributions of the MC MOT can be seen in figures 3.16, 3.17. Laser configurations which yield narrow velocity widths could be used to launch atoms, and as atoms can only accelerate while they are in a region where lasers are present, a circular path provides more acceleration space than a linear path of the same length.

As well as the inclusion of reradiation and absorption, other extensions of the MC could also be added: sub-Doppler cooling and interatomic collisions. Including interatomic collisions would in fact be relatively easy, as Van der Waal's forces between atoms can be included in a similar manner to the reradiative force. They differ only because the Van der Waal's force has the form $ar^{-6} + br^{-12}$ (cf. $F_{rerad} \propto r^{-2}$).
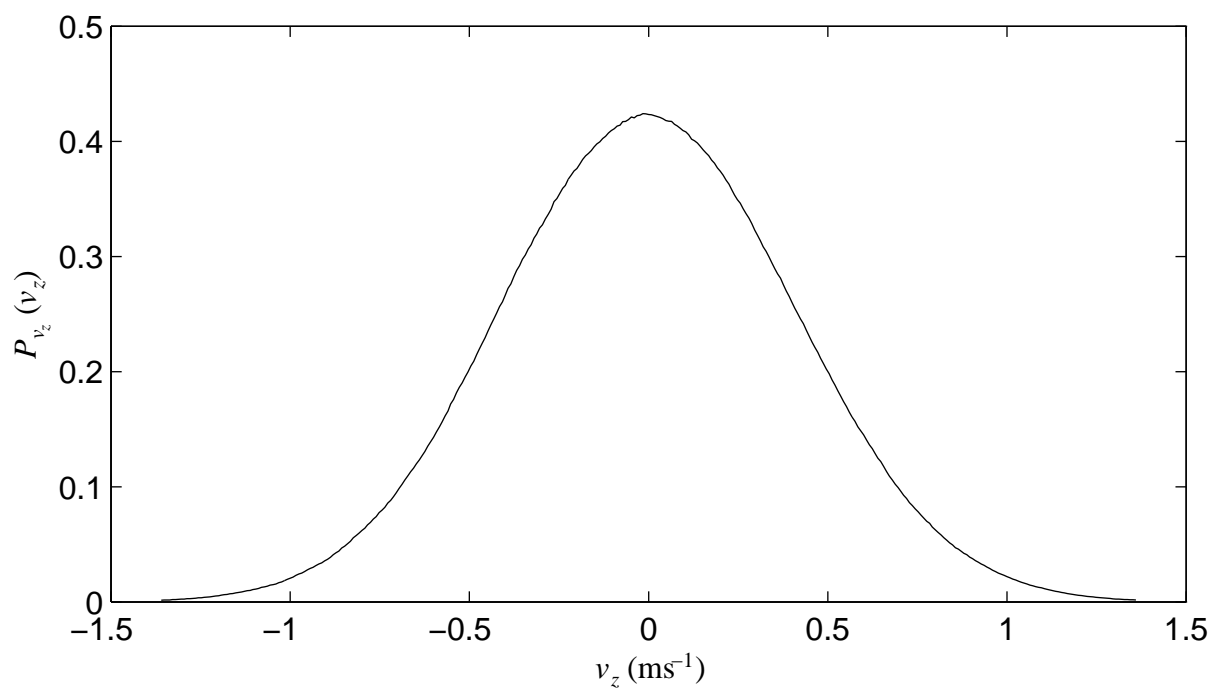
Figure 3.17: The relative probability distribution of the axial velocity v_z, using the same parameters. The distribution is Gaussian with a z 'temperature' $T_z = 465\mu$K.

Chapter 4

Sub-Doppler Theory

4.1 An Introduction to Sub-Doppler Cooling

The authority of Doppler Theory as a complete laser cooling theory was somewhat shaken in 1988, by the observation of sodium atoms in optical molasses that had been laser cooled to a temperature six times lower than the minimum temperature predicted by Doppler Theory. Several techniques for temperature determination were used by Lett *et al.* [42], and all verified their original observation. In the same paper the authors observed that the temperature depended quite strongly on the magnetic field in the molasses (low magnetic fields yielded lower temperatures) and that the temperature also depended on the polarisation of the lasers. They also speculated that it might be necessary to consider the fact that sodium atoms have multiple energy levels, rather than the two levels assumed in Doppler theory.

After a re-examination of the theory for multistate atoms, two groups proposed similar explanations of the sub-Doppler temperatures based on the non-adiabatic motion of a multilevel atom through a laser field with spatially varying polarisation [32]. These theories were developed with a more quantitative framework in 1989 by Dalibard and Cohen-Tannoudji [17], and Ungar *et al.* [75].

Three different mechanisms for sub-Doppler cooling were proposed, mainly concentrating on 1D models in their explanations. All the model involved the effects of the laser standing waves that were created in optical molasses and MOTs—unlike the Doppler theory, which assumes that the effect of each laser beam on an atom can be considered separately (i.e. phase is ignored). The mechanisms also involved spatial variation in the polarisation of the standing waves—or polarisation gradients.

The initial theories were considered in 1D, using two counterpropagating laser beams to create a standing wave: this approach was used in all three cooling mechanisms. In the following descriptions of the mechanisms, the lasers involved will propagate along the $\pm z$ axes. The definitions of the laser helicities with respect to this frame are shown in fig. 1 of ref. [17].

lin⊥lin configuration—Sisyphus effect

This mechanism relies on two linearly polarised laser beams, with axes of polarisation perpendicular to each other [17]. A magnetic field is not used in this mechanism, and so it can be assumed, without loss of generality, that the laser beam travelling in the $+z$ direction is polarised in the x direction ($\mathbf{E} = (E_x \cos(kz - \omega t), 0, 0)$) and the counterpropagating laser beam is polarised in the y direction ($\mathbf{E} = (0, E_y \cos(-kz - \omega t), 0)$). The total electric field created by the superposition of these two lasers is:

$$\mathbf{E}_{tot} = (E_x \cos(kz - \omega t), E_y \cos(-kz - \omega t), 0)$$

$$\mathbf{E}_{tot} = (E_x \cos kz \cos \omega t + E_x \sin kz \sin \omega t, E_y \cos kz \cos \omega t - E_y \sin kz \sin \omega t, 0). \tag{4.1}$$

At any given point on the z axis, the electric field can be thought of as the superposition of two

counter-rotating electric field vectors with variable phase and magnitude:

$$\mathbf{E}_+ = E_+ \left(\cos(\omega t + \phi_+), \sin(\omega t + \phi_+), 0 \right),$$

$$\mathbf{E}_- = E_- \left(\cos(\omega t + \phi_-), -\sin(\omega t + \phi_-), 0 \right),$$

(the subscripts denote the helicity of the light—σ^+ or σ^-). In this form, the total electric field is:

$$\mathbf{E}_{tot} = \quad ((E_+ \cos\phi_+ + E_- \cos\phi_-) \cos\omega t - (E_+ \sin\phi_+ + E_- \sin\phi_-) \sin\omega t,$$
$$(E_+ \sin\phi_+ - E_- \sin\phi_-) \cos\omega t + (E_+ \cos\phi_+ - E_- \cos\phi_-) \sin\omega t, 0). \tag{4.2}$$

Comparing co-efficients (with equation 4.1) and rearranging yields:

$$E_x \cos kz - E_y \sin kz = 2E_+ \cos\phi_+, \qquad E_x \cos kz + E_y \sin kz = 2E_- \cos\phi_-,$$

$$-E_x \sin kz + E_y \cos kz = 2E_+ \sin\phi_+, \qquad E_x \sin kz + E_y \cos kz = -2E_- \sin\phi_-.$$

The four equations can then be solved analytically for the new variables—only the simple case $E_x = E_y = E$ will be presented here however. The solutions for $E_\pm$ are: $E_+{}^2 = \frac{E^2}{2}(1 - \sin 2kz)$, $E_-{}^2 = \frac{E^2}{2}(1 + \sin 2kz)$. The details of the phases $\phi_\pm$ are easily derived, but unimportant for this discussion. From these relations it can be seen that the intensity ratio of the two senses of circular light varies periodically along the z axis, with period $\lambda/2$. The light varies from σ^+ only, to linear, to σ^- only and back again as z varies.

An $F = 1/2 \to F' = 3/2$ atomic transition is the simplest transition which leads to Sisyphus cooling, and will be considered here (see ref. [17], [69] for more detail), although the cooling scheme works for any $F \to F + 1$ transition. Two sublevels, $m_F = \pm 1/2$, exist in the $F = 1/2$ ground state. In a region of the z axis where the light polarisation is σ^+ an atom will be optically pumped into the $m_F = +1/2$ sublevel, whereas it will be optically pumped into the $m_F = -1/2$ sublevel when the polarisation is σ^- (see figure 4.1).
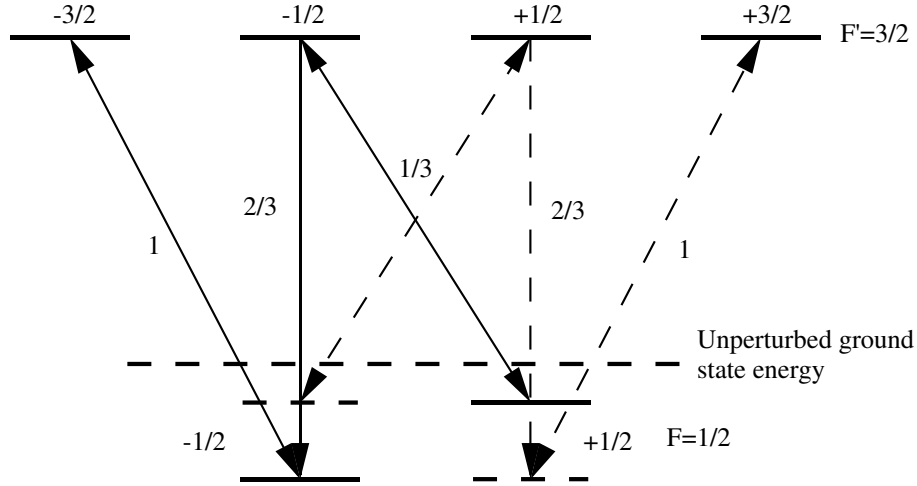

Figure 4.1: Energy level diagram of the $F = 1/2, F' = 3/2$ levels. Bold lines denote energy levels, with numbers corresponding to their m_F values. The finer lines denote allowable energy level transitions (labelled with their squared Clebsch-Gordan co-efficients). Dashed lines show shifted ground energy levels, and allowable transitions when the atom is in a region of σ^+ light only, the plain lines refer to the corresponding structures when it is in a region of σ^- light.

The one remaining feature that is necessary to observe the cooling mechanism is the AC Stark shift. When an atom is perturbed by a periodic electromagnetic field, this perturbation causes the energy levels of the atom to shift—a 'light shift.' This light shift is proportional to the intensity of the light used. For a red-detuned laser, the light shift is negative, and one can show using the Clebsch-Gordan coefficients of

the $F = 1/2 \rightarrow F' = 3/2$ transition that the $m_F = +1/2$ sublevel of an atom is shifted three times more by σ^+ light than σ^-. The converse is true of the $m_F = -1/2$ sublevel.

Using the $\sigma^\pm$ intensities derived above, the light shifts $\Delta E_\pm$ of the $m_F = \pm 1/2$ ground state sublevels are:

$$\Delta E_+ = \frac{\hbar \Delta s}{2} \left(\frac{1}{3}(1 + \sin 2kz) + (1 - \sin 2kz) \right) = \hbar(-\Delta)s(-2 + \sin 2kz)/3$$

$$\Delta E_- = \frac{\hbar \Delta s}{2} \left(\frac{1}{3}(1 - \sin 2kz) + (1 + \sin 2kz) \right) = \hbar(-\Delta)s(-2 - \sin 2kz)/3$$

where $s = \frac{2I/I_S}{1+(\Delta/\Gamma)^2}$, and $I = c\epsilon_0 E^2/2$ is the intensity in each laser beam. Note that these equations have $\sin 2kz$ instead of $\cos 2kz$ used in ref. [17], due to a different z axis origin in that description.

Now consider an atom at $2kz = \pi/2$, or $z = \lambda/8$ (figure 4.2). The light at this position is wholly σ^-, and so the atom is most likely to be in the $m_F = -1/2$ sublevel due to the optical pumping at that position. Suppose the atom has velocity v, in either the positive or negative z directions. In either case the light will begin to have a lower fraction of σ^- light, and the intensity of σ^+ light will increase. As the atom's position changes, its internal energy increases because the $m_F = -1/2$ sublevel is at a local minimum in energy when $z = \lambda/8$.

During the atom's motion in the laser light it will absorb and emit photons. After a single photon is absorbed and emitted the atom can either return to it's original $m_F = -1/2$ sublevel (this process can occur regardless of the helicity of light absorbed), or be optically pumped into the $m_F = +1/2$ sublevel (this process can only occur via the absorption of a σ^+ photon). If the latter of these two processes occurs, the potential energy of the atom changes while the kinetic energy stays approximately the same. The total energy of the atom (potential+kinetic) therefore changes, as does the atom's time-averaged kinetic energy. If the ground state sublevel transition occurs when the atom's initial potential is higher than its final potential, then the atom's total energy, as well as average kinetic energy, drops.
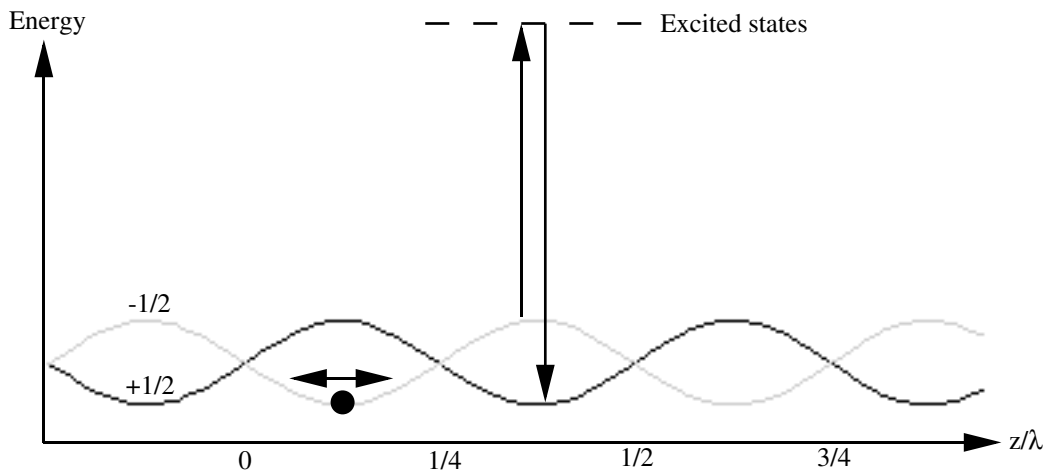

Figure 4.2: Ground level energies (denoted by their respective m_F values) vs. z/λ. An atom at $z = \lambda/8$ with $m_F = -1/2$ can travel in either direction. Whichever direction it travels, it will be more likely to undergo an absorption-emission cycle where it loses potential energy (as illustrated) rather than gain it.

For an atom in the $m_F = -1/2$ sublevel, the regions where its potential energy is higher than the $m_F = +1/2$ sublevel ($(n/2 - 1/4)\lambda < z < n/2\lambda$, $n \in \mathbf{Z}$) correspond directly to regions with higher σ^+ intensity. This means that the atom is more likely to make a change in kinetic energy (only possible with σ^+ light) when it is at a z position where it will *lose* kinetic energy. This cooling mechanism was dubbed Sisyphus cooling, after the Greek myth based on a character continually climbing hills.

This cooling effect relies on the energy level perturbation due to light shifts, and any other energy level perturbations, e.g. a Zeeman effect from a magnetic field, may in fact disrupt the cooling mechanism.

Difficulties will only arise when the Zeeman shift is comparable with the light shift, however [70], [51]. The light shift has approximate magnitude: $\Delta E \approx \hbar(I/I_S)\Gamma^2/(-\Delta)$ at large detunings. The Zeeman shift has magnitude $\Delta E \approx \mu_B B$ and so Sisyphus cooling should work in regimes where

$$\mu_B B << \hbar(I/I_S)\Gamma^2/(-\Delta). \tag{4.3}$$

This explains the experimentally observed low temperatures when the magnetic field is low [43].

It is possible to show that the theoretical temperature attained by atoms under this new cooling scheme is proportional to I/Δ at large detunings [13]. This trend has been frequently experimentally verified with caesium atoms [64], however it is difficult to obtain the same results with sodium. The reason for the difference is that sodium has low separation amongst its excited state energy levels. This makes it difficult to create large detunings (low temperatures) in these atoms without losing atoms to other energy levels [13].

$\sigma^+ - \sigma^-$ configuration—induced orientation

When a σ^+ laser beam travelling in the $+z$ direction ($\mathbf{E} = E(\cos(kz - \omega t), -\sin(kz - \omega t), 0)$) forms a standing wave with a σ^- laser beam, of equal intensity, travelling in the opposite direction ($\mathbf{E} = E(\cos(-kz - \omega t), \sin(-kz - \omega t), 0)$) the resulting electric field is:

$$\mathbf{E}_{tot} = 2E(\cos kz, -\sin kz, 0)\cos \omega t \tag{4.4}$$

i.e. at any given point on the z axis the polarisation is linear, but the direction of polarisation rotates helically with z. Sisyphus cooling doesn't occur in this regime, as the light in the standing wave contains equal quantities of σ^+ and σ^- sense light at all z values. Another cooling mechanism does exist however, the induced orientation effect.

An atom travelling with velocity v along the z axis will observe a rotating linear polarisation. It is possible to transform into a rotating frame within the atom's rest frame in which the laser polarisation has a fixed direction. However, Larmor's theorem states that an inertial field will appear as the result of the rotation, and that this inertial field is similar to a magnetic field along the rotation axis [17]. This induces a change in the populations of the ground state sublevels (the populations are symmetric when the atoms have no velocity), and creates a difference in the probability of absorption from each laser beam. The simplest atomic transition that this cooling mechanism will work on is an $F = 1 \rightarrow F' = 2$ transition.

The full details of the method are quite subtle, but can be found in ref. [17]. This more complicated treatment yields similar cooling forces and temperatures (proportional to I/Δ for large Δ) to the Sisyphus mechanism [75], [78], [17]. Steane and Foot [70] found that the induced orientation mechanism not only increased the damping force in a MOT, it also increased a MOT spring constant above the predicted Doppler level. Although a MOT has strong magnetic fields involved (unlike optical molasses), Steane and Foot also found that the strong spring constant confined the atoms to regions near the magnetic field zero of the trap—allowing polarisation gradient cooling to occur and producing sub-Doppler temperatures inside a caesium MOT.

$\sigma^+ - \sigma^+$ configuration, with transverse B field.

With two counterpropagating σ^+ laser beams, the total electric field is everywhere circular with σ^+ helicity, however the intensity of the light varies sinusoidally with position. Two distinct mechanisms can occur. If the optical pumping rate (in the standing wave nodes) is larger than the Larmor precession frequency, it is possible to show that a mechanism like the Sisyphus cooling effect occurs [75]. If the converse is true one can show that there is a magnetic resonance at a particular velocity [67]. This cooling mechanism slows atoms to a non-zero velocity.

These 1D theories do not have a complementary 3D, due to the complex nature of the standing waves involved, however 3D experimental results agree surprisingly well with the 1D model. The nature of the 3D standing wave, as it pertains to these 1D mechanisms will be considered in the next section.

4.2 Standing on Waves

In 1991 Hemmerich *et al.* [33] conducted an experiment in which the relative time phase of standing waves generated in two mutually orthogonal linear optical resonators was altered. The relative phase of the standing waves had a large effect on an atomic beam which was passed through the beam intersection region.

A 1D standing wave is made up of two counterpropagating laser beams, with arbitrary phases. Consider the linearly polarised arrangement with the beam travelling in the $+z$ direction governed by the electric field: $\mathbf{E}_{z+} = (\cos(kz - \omega t + \phi_{z+}), 0, 0)$. The corresponding field for the laser travelling in the $-z$ direction is chosen to be: $\mathbf{E}_{z-} = (\cos(-kz - \omega t + \phi_{z-}), 0, 0)$. These can be rewritten as:

$$\mathbf{E}_{z+} = \left(\cos\left(k(z - \frac{1}{2k}[\phi_{z+} - \phi_{z-}]) - \omega t + \frac{1}{2}[\phi_{z+} + \phi_{z-}] \right), 0, 0 \right),$$

$$\mathbf{E}_{z-} = \left(\cos\left(-k(z - \frac{1}{2k}[\phi_{z+} - \phi_{z-}]) - \omega t + \frac{1}{2}[\phi_{z+} + \phi_{z-}] \right), 0, 0 \right).$$

If a transformation to the new co-ordinate $z^* = z - \frac{1}{2k}[\phi_{z+} - \phi_{z-}]$ is made, then there is only one phase parameter necessary for describing the standing wave – the parameter $\overline{\phi_z} = \frac{1}{2}[\phi_{z+} + \phi_{z-}]$.

This parameter is relatively unimportant for a 1D standing wave, as it only places a phase delay on the total standing wave. If, however, two separate standing waves (along the y and z directionls, say) are compared, each with their own 'average phases' $\overline{\phi_y}, \overline{\phi_z}$, it is clear that although both standing waves are periodic in time, they may not necessarily pulsate synchronously. It is also clear that it is only the *difference* in these phases that will affect the total standing wave. If the phase difference is kept constant, but the phases vary, the only effect on the periodic total standing wave is a phase delay. For this reason one of $\overline{\phi_y}, \overline{\phi_z}$ can be set to zero without loss of generality. This idea generalises to three dimensions—the 'average phase' along one dimension can be set to zero, but the other two must be included for a general description.

The relative phase of the laser beams in a 3D standing wave, directly affects the polarisation gradients within the standing wave, and hence the expected size of the force parameters of the laser field. Detailed analytic calculations of the diffusion and damping constants versus phase, for a linearly polarised 2D beam arrangement, were carried out by Mølmer [49]. Numerical calculations in 3D for four different laser configurations, with all standing waves in phase, were also calculated.

If a quantisation axis is chosen in 3D, then the intensities of σ^+ and σ^- light, $I_{\sigma^+}, I_{\sigma^-}$, can be determined at a given position $\mathbf{r}$ and for a given choice of phases. Steane *et al.* [71] defined a parameter

$$p(\mathbf{r}) = I_{\sigma^+}(\mathbf{r}) - I_{\sigma^-}(\mathbf{r})$$

to represent the ellipticity gradient in the polarisation. If p alters between negative and positive with position, then a Sisyphus cooling mechanism will be present as the dominant polarisation varies between σ^- and σ^+. The parameter p can also be normalised against the average total intensity $\overline{I_{tot}(\mathbf{r})}$:
$q(\mathbf{r}) = (I_{\sigma^+}(\mathbf{r}) - I_{\sigma^-}(\mathbf{r}))/\overline{I_{tot}(\mathbf{r})}$. The intensities, and therefore p and q, are periodic in all three Cartesian directions, with period λ.

A study of Sisyphus processes in four different 3D laser standing waves will now be considered. The four different arrangements are described, without phase shifts, in ref. [49] and the phase shifts will be included here. First it is necessary to derive the total electric field vector for each configuration, and this can be made easier by using the permutation of co-ordinates to extend 1D configurations to 3D. From now on the overline on the 'average phase' will be removed for clarity. Phases on the y and z standing waves only will be included, for the reason discussed earlier.

The 1D configurations are (cf. ref. [49]):

(a) Linearly polarised plane standing wave:

$$\begin{aligned} \mathbf{E} &= E_z \left((\cos(kz - \omega t + \phi_z), 0, 0) + (\cos(-kz - \omega t + \phi_z), 0, 0) \right) \\ &= 2E_z(\cos\phi_z \cos kz \cos\omega t + \sin\phi_z \cos kz \sin\omega t, 0, 0) \end{aligned}$$

(b) σ^+–σ^- configuration (cf. equation 4.4):

$$\mathbf{E} = 2E_z(\cos\phi_z \cos kz \cos\omega t + \sin\phi_z \cos kz \sin\omega t, -\cos\phi_z \sin kz \cos\omega t - \sin\phi_z \sin kz \sin\omega t, 0)$$

(c) σ^+–σ^+ configuration:

$$
\begin{aligned}
\mathbf{E} \ &= E_z \left((\cos(kz - \omega t + \phi_z), -\sin(kz - \omega t + \phi_z), 0) + (\cos(-kz - \omega t + \phi_z), -\sin(-kz - \omega t + \phi_z), 0) \right) \\
&= 2E_z(\cos\phi_z \cos kz \cos\omega t + \sin\phi_z \cos kz \sin\omega t, -\sin\phi_z \cos kz \cos\omega t + \cos\phi_z \cos kz \sin\omega t, 0)
\end{aligned}
$$

(d) lin$\perp$lin configuration:

$$
\begin{aligned}
\mathbf{E} \ &= \ E_z \left((\cos(kz - \omega t + \phi_z), 0, 0) + (0, \cos(-kz - \omega t + \phi_z), 0) \right) \\
&= \ E_z \left(\cos(kz + \phi_z)\cos\omega t + \sin(kz + \phi_z)\sin\omega t, \cos(-kz + \phi_z)\cos\omega t + \sin(-kz + \phi_z)\sin\omega t, 0 \right).
\end{aligned}
$$

These configurations are based on the assumption that the $+z$ and $-z$ laser beams have equal intensities I_z. The relation $I_z = c\epsilon_0 E_z{}^2$ holds for the configurations with circularly polarised light ((b), (c)) whereas $I_z = c\epsilon_0 E_z{}^2/2$ for the linearly polarised cases.

By permuting the variables and co-ordinates $x \to y \to z \to x$ the total electric field vector in 3D is obtained from the configurations in 1D. An example is shown for (d):

$$
\begin{aligned}
\mathbf{E}_{tot} = \ &E_z \left(\cos(kz + \phi_z)\cos\omega t + \sin(kz + \phi_z)\sin\omega t, \cos(-kz + \phi_z)\cos\omega t + \sin(-kz + \phi_z)\sin\omega t, 0 \right) + \\
&E_x \left(0, \cos(kx)\cos\omega t + \sin(kx)\sin\omega t, \cos(-kx)\cos\omega t + \sin(-kx)\sin\omega t \right) + \\
&E_y \left(\cos(-ky + \phi_y)\cos\omega t + \sin(-ky + \phi_y)\sin\omega t, 0, \cos(ky + \phi_y)\cos\omega t + \sin(ky + \phi_y)\sin\omega t \right).
\end{aligned}
$$

If this technique is applied to polarisation (b), the polarisation configuration of a MOT is not obtained, because the $\mathbf{B}$ field in a MOT requires σ^-–σ^+ polarisation, rather than σ^+–σ^-, on the z axis. The results that follow are the same for both a MOT configuration and the 3D configuration of (b), however, and the only change in the electric field equations is that $+z$ has to be replaced with $-z$.

One feature that all laser configurations have in common is that the total electric field can be written in the form:

$$\mathbf{E}_{tot} = (a\,\cos\omega t + b\,\sin\omega t, c\,\cos\omega t + d\,\sin\omega t, e\,\cos\omega t + f\,\sin\omega t) \tag{4.5}$$

where a, b, c, d, e, f are all functions of $\mathbf{r}$, ϕ_y, ϕ_z. In the following derivation the z axis will be chosen as the quantisation axis. The z component of $\mathbf{E}_{tot}$, $E_{tot_z} = e\cos\omega t + f\sin\omega t$, is therefore π polarised light. It can be written as a single sinusoidal electric field: $E_{tot_z} = E\cos(\omega t - \epsilon)$ where $E^2/2 = (e^2 + f^2)/2 = I_\pi/(c\epsilon_0)$ and $\tan\epsilon = f/e$.

Another important point is that the electric field components in the xy plane can be described as the superposition of two circularly polarised electric field vectors (cf. the lin$\perp$lin description):

$$\mathbf{E}_+ = E_+(\cos(\omega t + \phi_+), \sin(\omega t + \phi_+), 0),$$

$$\mathbf{E}_- = E_-(\cos(\omega t + \phi_-), -\sin(\omega t + \phi_-), 0),$$

where the subscripts denote the helicity of the laser light. When the total of these two electric fields (equation 4.2) is compared to

$$\mathbf{E}_{tot} = (a\cos\omega t + b\sin\omega t, c\cos\omega t + d\sin\omega t, 0),$$

the following relations are obtained: $a = E_+\cos\phi_+ + E_-\cos\phi_-$, $b = -E_+\sin\phi_+ - E_-\sin\phi_-)$, $c = E_+\sin\phi_+ - E_-\sin\phi_-$, $d = E_+\cos\phi_+ - E_-\cos\phi_-$. Solving for these relations yields:

$$E_+{}^2 = \frac{1}{4}(a + d)^2 + \frac{1}{4}(c - b)^2 = \frac{I_{\sigma^+}}{c\epsilon_0},$$

$$E_-{}^2 = \frac{1}{4}(a - d)^2 + \frac{1}{4}(c + b)^2 = \frac{I_{\sigma^-}}{c\epsilon_0}.$$

Thus whichever 3D standing wave is under consideration, finding the functions a, b, c, d, e, and f will lead to the intensities I_π, $I_{\sigma\pm}$. The total of these three intensities is given by $I_{tot} = \frac{c\epsilon_0}{2}(a^2 + b^2 + c^2 + d^2 + e^2 + f^2)$. Also since $I_{\sigma\pm}$ are known, it is possible to find the polarisation parameter p, for the z quantisation axis. Note that by permuting the variables $(a, b) \to (c, d) \to (c, d)$ it is possible to find the equivalent intensities and polarisation parameters along the x and y axes. These parameters should be similar to the results when z is the quantisation axis, due to symmetry, however π light along one quantisation axis, is not π along a different axis. It is possible, for certain phase combinations (ϕ_y, ϕ_z), to obtain situations where the sub-Doppler mechanisms are stronger in one direction than others. Let p_{x_i} denote the polarisation parameter p when the quantisation axis is along the x_i direction.

In order to compare the effectiveness of the polarisation gradients in a given standing wave, it is helpful to have some sort of quantitative parameter. The Sisyphus cooling mechanism works best when the polarisation alternates between σ^+ and σ^-. A measure of the variation in p_{x_i} is the variance of p_{x_i}, $\mathrm{var}(p_{x_i}) = \overline{(p_{x_i} - \overline{p_{x_i}})^2}$. For the 3D standing wave arrangements (a)-(d), with equal intensities in counterpropagating laser beams, the result $\overline{p_{x_i}} = 0$ will be expected from the symmetry of the situation.

The next question is to ask what the p_{x_i} will be averaged over. A spatial average is a good option, especially as the intensities, and therefore p_{x_i}, are periodic in space. The technique of spatially averaging a function over a cubic volume, with sides of length λ, will be implemented in the following analytic calculations. The parameter $q_{x_i}' = p_{x_i}/I_{tot}(\mathbf{r})$ cannot be analytically averaged over such a volume, due to the spatial variation of I_{tot}. This function may in fact undulate significantly (I_{tot} can drop to zero at some points of the standing wave) and this was one of the reasons q was defined using the spatial average of $I_{tot}(\mathbf{r})$. The reason p is normalised to q is to give a quantitative measure of the strength of the polarisation gradients, relative to the laser intensity necessary to create them. This makes it easy to compare the effectiveness of different 3D standing waves, using the same light intensities in each beam. The values of $\overline{q_{x_i}}$ and $\mathrm{var}(q_{x_i})$ will therefore be used to measure the approximate strength of the Sisyphus mechanism in the various standing wave arrangements.

The simplification $E_x = E_y = E_z$ (i.e. $I_x = I_y = I_z = I$) will be employed for the calculations. This simplifies the algebra somewhat, although it is important to note that the technique used here will work for six laser beams with independent intensities (i.e. intensity imbalances can occur), and the beams can be misaligned. The reason that these cases are ignored is to simplify the description, although the model will hopefully still include most of the relevant Physics. With the simplifications used here, all configurations have $\overline{q_{x_i}} = 0$ regardless of the phases $\phi_{y/z}$—i.e. the spatial average of the σ^+ and σ^- intensities is the same. This would not be the case if counterpropagating laser beams had imbalanced intensities.

Full details of the results will be given for configuration (a), which generated the simplest standing wave. The polarisation parameters q_{x_i} are:

$$q_x = 4 \cos kx \cos ky \sin \phi_y / 3,$$

$$q_y = -4 \cos ky \cos kz \sin(\phi_y - \phi_z)/3,$$

$$q_z = -4 \cos kx \cos kz \sin \phi_z / 3,$$

note that the position dependent trigonometric terms will spatially average to zero. This leads to the result that $\overline{q_{x_i}} = 0$ anticipated earlier. The total intensity is:

$$I_{tot}(\mathbf{r}) = 2I(3 + \cos 2kx + \cos 2ky + \cos 2kz).$$

The function I_{tot} is independent of the laser phases, and spatially averages to the total intensity of the six separate lasers, $6I$. Another point is that the total intensity can fluctuate between values of 0 and $12I$, and so the intensity of this configuration is far from smooth and is similar to the 1D analogue of the type (a) standing wave in this respect.

The values of $q_{x_i}^2$ are as follows:

$$q_x^2 = 16 \left(\cos^2 kx \cos^2 ky \sin^2 \phi_y \right) /9,$$

$$q_y{}^2 = 16 \left(\cos^2 ky \cos^2 kz \sin^2 (\phi_y - \phi_z) \right)/9,$$

$$q_z{}^2 = 16 \left(\cos^2 kx \cos^2 kz \sin^2 \phi_z \right)/9.$$

Spatially averaging leads to the parameters:

$$\overline{q_x{}^2} = 4/18 \left(1 - \cos 2\phi_y \right),$$

$$\overline{q_y{}^2} = 4/18 \left(1 - \cos 2(\phi_y - \phi_z) \right),$$

$$\overline{q_z{}^2} = 4/18 \left(1 - \cos 2\phi_z \right).$$

As $\overline{q_{x_i}} = 0$, $\mathrm{var}(q_{x_i})$ and $\overline{q_{x_i}{}^2}$ are equivalent. From these calculations it is clear that the relative phases of the three 1D standing waves in configuration (a) are extremely important in determining the strength of the Sisyphus mechanism in the standing wave.

When $\phi_y = \phi_z = 0$ there are always equal amounts of the two σ components in the light, and so no Sisyphus mechanism exists in the trap. This is quite different from the case when $\phi_y = \phi_z = \pi/2$, as this will yield strong polarisation gradients ($q = 8/18$) for atoms travelling along the x and z axes. Most experiments in laser cooling have not controlled the relative phase of the standing waves however, and ϕ_y, ϕ_z will drift randomly due to mechanical vibrations, which can affect the phase on a millisecond time scale [49]. A better parameter for the cooling rate in the configurations would perhaps be the average, over the phases ϕ_y, ϕ_z, of the parameters $\mathrm{var}(q_{x_i})$. The values of this new parameter, $\zeta_{x_i} = \overline{\mathrm{var}(q_{x_i})}$ for the polarisation scheme (a), are

$$\zeta_x = \zeta_y = \zeta_z = 4/18.$$

Note that ζ ceases to be a useful parameter if fluctuations in the phase are slow enough so that the properties of any laser cooled atoms will follow the phase. If it was desirable to obtain optimal polarisation gradients in configuration (a), it is clear that the ability to hold the phases constant would be necessary, rather than allowing the phases to drift into regimes with less effective Sisyphus cooling.

Polarisations (b)–(d) all have $\overline{q_{x_i}} = 0$ for $i = 1 \to 3$, and the other results for polarisations (b)–(d) are:

(b):

$$I_{tot}(\mathbf{r}) = 2I \left(3 - 2 \sin kx \cos ky \cos \phi_y - 2 \cos kx \sin kz \cos \phi_z - 2 \sin ky \cos kz \cos(\phi_y - \phi_z) \right)$$

$$\mathrm{var}(q_x) = \mathrm{var}(q_y) = \mathrm{var}(q_z) = \left(3 - \cos 2\phi_y - \cos 2\phi_z - \cos 2(\phi_y - \phi_z) \right)/18$$

$$\zeta_x = \zeta_y = \zeta_z = 3/18$$

(c):

$$I_{tot}(\mathbf{r}) = 4I \left(\cos^2 kx + \cos^2 ky + \cos^2 kz + \cos ky \cos kz \sin(\phi_z - \phi_y) + \cos kx(\cos ky \sin \phi_y - \cos kz \sin \phi_z) \right)$$

$$\mathrm{var}(q_x) = \left(6 - \cos 2\phi_y - \cos 2\phi_z + \cos 2(\phi_y - \phi_z) \right)/18$$

$$\mathrm{var}(q_y) = \left(6 - \cos 2\phi_y + \cos 2\phi_z - \cos 2(\phi_y - \phi_z) \right)/18$$

$$\mathrm{var}(q_z) = \left(6 + \cos 2\phi_y - \cos 2\phi_z - \cos 2(\phi_y - \phi_z) \right)/18$$

$$\zeta_x = \zeta_y = \zeta_z = 6/18$$

(d):

$$I_{tot}(\mathbf{r}) = 2I \left(3 + \cos(kx + ky + \phi_y) + \cos(kx + kz - \phi_z) + \cos(ky + kz - \phi_y + \phi_z) \right)$$

$$\mathrm{var}(q_x) = \mathrm{var}(q_y) = \mathrm{var}(q_z) = 4/18$$

$$\zeta_x = \zeta_y = \zeta_z = 4/18$$

Plots showing the nature of $\mathrm{var}(q_{x_i})$ in configurations (a)–(c) can be found in figures 4.3, 4.4, 4.5.

From these results it is possible to make a number of deductions regarding the different configurations. In all configurations $\zeta_x = \zeta_y = \zeta_z$ ($= \zeta$ say), as expected from the isotropic nature of the laser configurations.
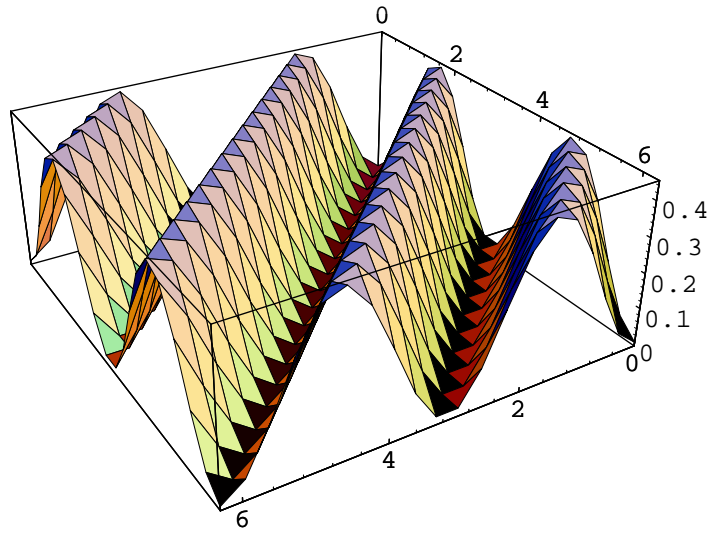
Figure 4.3: The Sisyphus cooling parameter $\mathrm{var}(q_y)$ versus the phases ϕ_y and ϕ_z, of the y and z laser beams. The figure shows $\mathrm{var}(q_y)$ for configuration (a)—the plots for $\mathrm{var}(q_x)$, $\mathrm{var}(q_z)$ are similar. The surface $\mathrm{var}(q_y)$ is periodic in the phases, and the region shown $(0 < \phi_y < 2\pi,\ 0 < \phi_z < 2\pi)$ gives a periodic 'tile' for the entire surface.
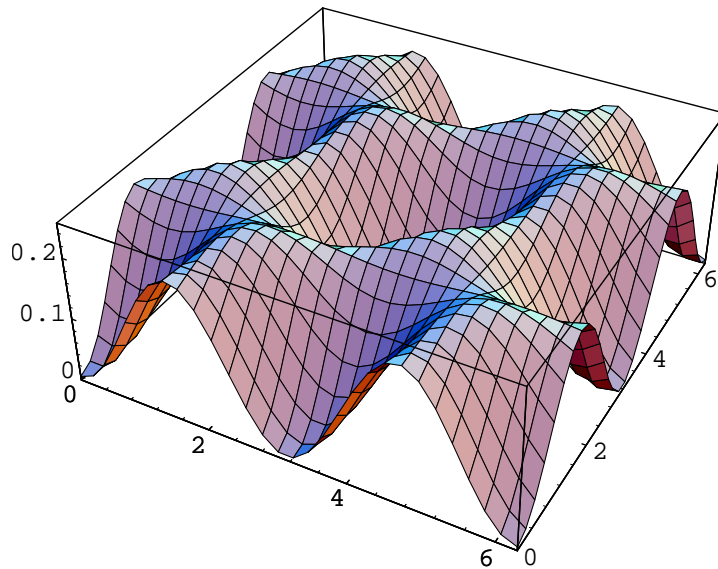

Figure 4.4: The Sisyphus cooling parameter $\mathrm{var}(q_x) = \mathrm{var}(q_y) = \mathrm{var}(q_z)$ for configuration (b) versus the phases ϕ_y and ϕ_z.
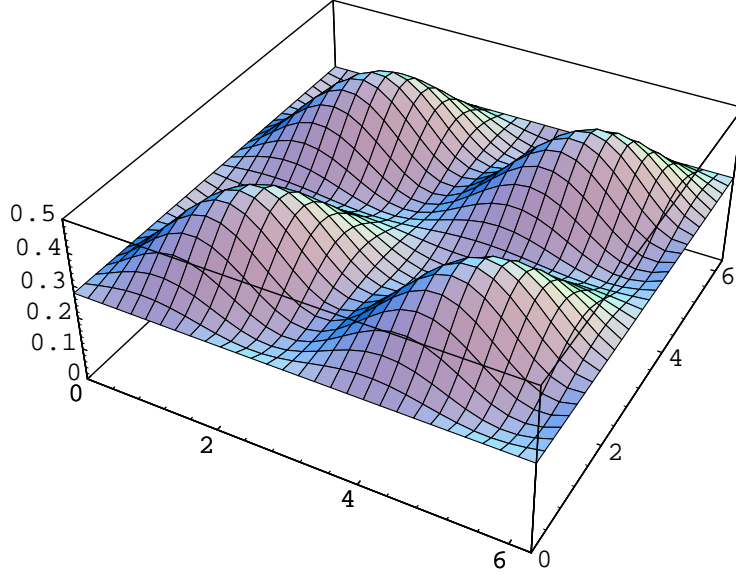
Figure 4.5: The Sisyphus cooling parameter var(q_x) for configuration (c), versus ϕ_y and ϕ_z. The figure for configuration (d) is omitted, due to the surface's simplicity.

If the phases alter randomly, then the Sisyphus parameter ζ gives an approximate quantitative measure of the lin⊥lin Sisyphus cooling strength in the standing waves. The values of ζ were: $\zeta = 8/36$ for configuration (a), $\zeta = 6/36$ for (b), $\zeta = 12/36$ for (c), $\zeta = 8/36$ for (d). It is clear that configuration (c) should give the best phase-averaged Sisyphus cooling. The equivalent value of ζ for a 1D lin⊥lin configured standing wave is $\zeta = 1/2 = 18/36$.

The ranges of the Sisyphus parameters over the phase domain were ($i \in \{1, 2, 3\}$): $0 \le \text{var}(q_{x_i}) \le 16/36$ for (a), $0 \le \text{var}(q_{x_i}) \le 9/36$ for (b), $9/36 \le \text{var}(q_{x_i}) \le 18/36$ for (c), $8/36 \le \text{var}(q_{x_i}) \le 8/36$ for (d). If the relative phases of the standing wave lasers were controlled, then configurations (a) and (c), with optimised phases, should give the best Sisyphus parameters. It should however be noted that unlike configurations (b) and (d), (a) and (c) have different phase dependences for var(q_x), var(q_y), and var(q_z). This also means that if configurations (a) and (c) are used, the phases which maximise var(q_x), say, do not necessarily maximise var(q_y). It is certainly clear, due to their var(q_{x_i}) ranges, that configuration (c) will always have higher polarisation gradients in all directions than configurations (b) (equivalent to a MOT) and (d). Configuration (c) certainly seems the best configuration for Sisyphus cooling, but a comparison with (a) still needs to be made.

The best way to optimise configurations (a) and (c), when considering *all* directions of travel, would probably be to optimise the average of the three var(q_{x_i}) parameters; i.e. optimise the variable:

$$\overline{\text{var}(q_{x_i})} = \sum_{i=1}^{3} \text{var}(q_{x_i})/3$$

with respect to phase. For configuration (a) this yields:

$$\overline{\text{var}(q_{x_i})} = \frac{2}{27} \left(3 - \cos 2\phi_y - \cos 2\phi_z - \cos 2(\phi_y - \phi_z)\right),$$

with corresponding result for configuration (c):

$$\overline{\text{var}(q_{x_i})} = \frac{1}{54} \left(18 - \cos 2\phi_y - \cos 2\phi_z - \cos 2(\phi_y - \phi_z)\right).$$

These functions have a similar phase dependence to the function var(q_{x_i}) of configuration (b). The phase term, $-\cos 2\phi_y - \cos 2\phi_z - \cos 2(\phi_y - \phi_z)$, has minimum -3 and maximum $+3/2$. Therefore the ranges of

$\overline{\text{var}(q_{x_i})}$ values for configurations (a) and (c) respectively are:

$$0 \leq \overline{\text{var}(q_{x_i})} \leq 36/108.$$

$$30/108 \leq \overline{\text{var}(q_{x_i})} \leq 39/108.$$

4.2.1 Conclusions

The phases that maximise and minimise the value of $\overline{\text{var}(q_{x_i})}$ in both configurations (a) and (c), are also phases which create equal values of $\text{var}(q_{x_i})$ in all three Cartesian directions, i.e. isotropic cooling regimes. It definitely appears therefore, that configuration (c) is still the best for Sisyphus cooling: it can create isotropic cooling, with a high value of $\overline{\text{var}(q_{x_i})}$ and only minor dependence on phase.

This conclusion can be compared with that of Mølmer [49]. In ref. [49] configurations (a)→(d) were considered, however the phases $\phi_{y/z}$ were set to zero. With these phases it is clear that $\text{var}(q_{x_i}) = 0$ in configurations (a) and (b) (no Sisyphus polarisation gradients exist along the Cartesian axes). It is therefore not surprising that Mølmer reached the conclusion that lower temperatures could be reached with zeroed phases in configurations (c) and (d), for which $\text{var}(q_{x_i}) = 5/18$, $4/18$ respectively ($i \in \{1, 2, 3\}$). His results predicted that configuration (d) would provide better cooling than that of (c) in this phase scheme, contrary to the $\text{var}(q_{x_i})$ parameters shown here. In both the calculations here and in ref. [49] the configurations (c) and (d) have very similar cooling parameters, and the difference can probably be explained by noting that Mølmer included the effects of induced orientation cooling mechanisms, which have been omitted here.

Although only a parameter for the lin⊥lin Sisyphus cooling mechanism has been developed here, it should be possible to develop similar parameters for measuring the 3D effects of other cooling mechanisms. From brief investigations into this idea it seems that, at least for induced orientation cooling, a parameter exists, but would have to be numerically integrated over space. Results could still be obtained however, without much calculation time. The main reason that the Sisyphus mechanism has been singled out is due to the fact that the diffusion and friction forces from this effect are stronger, by a factor of $\approx (\Delta/\Gamma)^2$ (at high detunings), than those created by the induced orientation mechanism. If Sisyphus effects are present, they will have the largest effect on cooling.

For complete coverage of the forces acting in a 3D standing wave, it would also be necessary to consider the radiation pressure vortices (RPVs) discussed by Hemmerich *et al.* [33], [34]. An approximate parameter to quantify this vortex force could also be calculated. A complete description of laser cooling could probably not be created around these parameters, as the equilibrium position distribution of the atoms on a wavelength scale is also important in the cooling process. The parameters may provide useful information about the relative sizes of the forces and their nature however.

Chapter 5

Sub-Doppler Experiment

5.1 The Plan

In chapter 4 the experimental observation of temperatures below the Doppler limit was discussed, as were the theoretical mechanisms behind the low temperatures. In a MOT the quadrupole magnetic field, $\mathbf{B} \approx \pm b(x, y, -2z)$, and circularly polarised lasers, lead to a trapping force on atoms within the intersection region of the laser beams. If counterpropagating laser intensities are balanced, then this confining force prevents the laser cooled atoms drifting away from the vicinity of the magnetic field zero.

Although sub-Doppler temperatures have been observed in a caesium MOT, [70], it was at the expense of the total number trapped atoms [51]. The magnetic field in a MOT also puts constraints (equation 4.3) on the sub-Doppler cooling mechanisms, which work best in regions with low magnetic fields. Removal of the magnetic field therefore tends to lower atomic temperatures, and so in order to obtain atoms cooled to sub-Doppler temperatures, atoms are initially collected in a MOT, generating a large number of trapped atoms. These atoms are further cooled in optical molasses. In molasses confinement is lost, due to the removal of the magnetic field, however the lasers still provide a cooling force. These atoms can then be used as a source of ultra-cold atoms for a variety of other experiments.

The temperature of atoms in molasses is expected to obey the relationship:

$$T \propto \frac{I}{-\Delta}.$$

Optimal temperatures in molasses can therefore be obtained when the intensity is low, and the detuning large. These conditions are different from those necessary to provide a large number of atoms in a MOT—i.e. moderate detunings and higher intensities [44]. However the atoms in the MOT can be collected at these optimal parameters, and the intensity and frequency can be 'switched' at approximately the same time as the magnetic field [50]. Simpler techniques involve only adjusting the laser frequency [62], or the laser intensity [38], [39].

The latter of these techniques has been used quite successfully in sodium—the close hyperfine levels of sodium, compared to caesium, mean that sub-Doppler cooling ceases to be effective at large detunings [13]. The detuning was held constant by Kasevich *et al.* [39], yet one of the lowest temperatures seen in sodium, $\approx 25\mu$K, was still obtained (cf. refs. [43], [78]). The detuning was at a value which approximately optimised the number of atoms collected in the MOT.

Altering the detuning requires the use of a double-pass AOM—a piece of equipment that is relatively difficult to set up, and so the method of Kasevich *et al.* is a much simpler mechanism for providing large quantities of sub-Doppler sodium atoms. Sodium atoms were used for the experiments in this thesis and the experimental goal was to emulate the technique of Kasevich *et al.*, or to find any problems in the present set-up that prevent the achievement of this goal.

5.2 The Initial MOT

A sodium MOT already existed in the lab and was created by Dr. Ann-Marie Oien as part of her PhD thesis. The MOT was loaded from the background vapour of a heated sodium cell, in a method similar to the first such MOT [50]. Kasevich *et al.* used a laser-cooled atomic beam to load their MOT.

A very instructive paper on how to build a rubidium MOT was written by Wieman *et al.* [80], and contains a detailed description of most of the equipment used in MOTs.
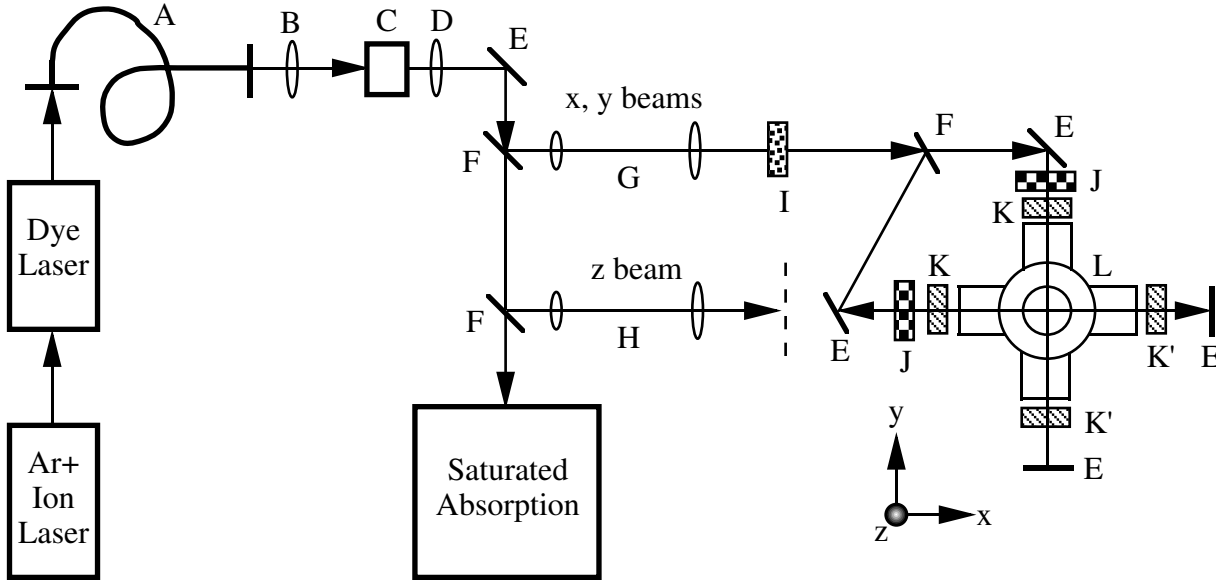

Figure 5.1: Schematic diagram of the MOT used in the lab. The optical components are: a fibre-optic cable (A), a spherical convex lens (B), an electro-optic modulator (C), a cylindrical convex lens (D), mirrors (E), 50/50 beam-splitters (F), the confocal beam expander for the $x + y$ laser beam (G), the confocal beam expander for the z beam (H), a half-wave plate (I), linear polarisers (J), quarter-wave plates (K, K') and the cell (L). The z beams, with it's associated linear polariser and quarter-wave plates, are omitted from the diagram. Also omitted are the magnetic field coils, which will be discussed later.

The Lasers

The laser light used in the MOT was created by a Coherent Radiation CR 699-21 dye laser, which was pumped by a Coherent Radiation CR-15 argon-ion laser. The laser light emitted by the dye laser was vertically polarised.

Optical Fibres and Wavemeter

After emerging from the dye laser, the laser light was separated into two beams with a beamsplitter. The majority of the light was coupled into a polarisation-preserving, single-mode optical fibre. This light was transferred from the table on which the lasers were situated, onto the table where the trapping apparatus was sited. In the process of travelling to this table, the fibre was rotated to obtain horizontal polarisation on the trapping table.

The weaker laser beam from the beamsplitter was coupled into a fibre which lead to another table, on which a wavemeter was situated. The wavemeter could be used to find the approximate wavelength of the laser light, and therefore differentiate between the D1 and D2 sodium lines (the latter of which produces trapping). Saturated absorption spectra of the two D lines are quite dissimilar, as are the tuning ranges of the D lines as observed in a sodium lamp. These methods could also be used to find the correct (D2) line.

5.2.1 The Electro-Optic Modulator (EOM).

Sodium's electronic energy levels will now be considered. The repumping energy transition, $F = 1 \to F' = 2$, and the cooling and trapping transition, $F = 2 \to F' = 3$, are shown as solid double-ended arrows in figure 5.2. The energy level scheme is considerably more complicated than the $F = 0 \to F' = 1$ system considered in the Doppler theory earlier.
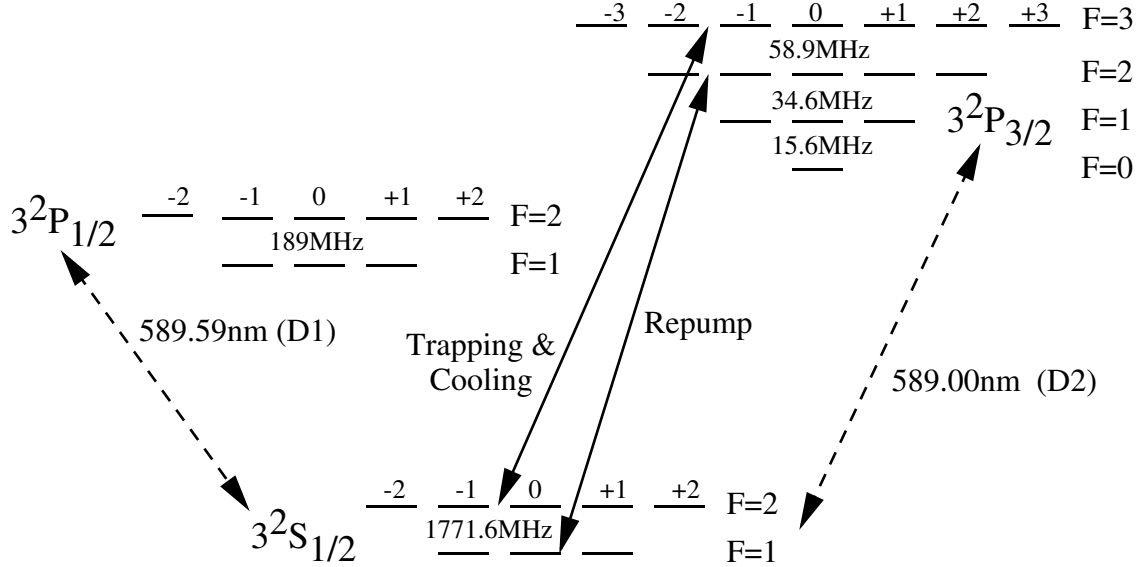

Figure 5.2: The energy level diagram of sodium—energy differences are not to scale. The frequencies written between F levels correspond to the energy differences between these levels. The smaller numbers on constant F levels denote the m_F value of energy sublevels.

A cloud of sodium atoms will typically have an equilibrium population distribution over the ground states $F = 1$ and $F = 2$. The $F = 2 \to F' = 3$ transition excites atoms to the $3^2P_{3/2}$ $F' = 3$ level, where they decay to the $F = 2$ ground state again after photon emission ($|F_{initial} - F_{final}| \leq 1$ for such a transition). Such processes do not change the ground level populations. This is unfortunately not always the case, and inter-atomic collisions can change the F value of atoms, causing them to enter $3^2P_{3/2}$ F levels that allow decay to the $F = 1$ ground state. Due to the Lorentzian response of an atom to near-resonant transition frequencies, it can be seen that light which excites the $F = 2 \to F' = 3$ may also excite transitions to other $3^2P_{3/2}$ F levels. This will once again provide a mechanism for atoms to leave the $F = 2$ ground state.

Laser cooling requires an atom to continuously cycle from $F = 2 \leftrightarrow F' = 3$, in order to provide cooling and confinement. If a repumping laser frequency is not used, the atoms are optically pumped into the $F = 1$ ground state and cooling stops. The repumping laser therefore ensures the $F = 2$ ground state population does not become depleted. The laser cooling/repump transitions described here lead to the 'type I' MOT, however it is also possible to cool and repump on the $F = 1 \leftrightarrow F' = 0$ and $F = 2 \leftrightarrow F' = 2$ transitions respectively. This mechanism leads to a 'type II' MOT.

In order to provide both a repump and a trapping laser, two lasers can be used, or a much simpler solution is provided in the Electro-Optic Modulator or EOM. If a radio frequency (RF) field with frequency ν_{RF} is applied to certain crystals, the RF field modulates the refractive index of the crystal at the same frequency, ν_{RF}. The fluctuating refractive index produces frequency sidebands on the 'carrier' light frequency, ν_0, of a laser passing through the crystal. The sidebands are at frequencies $\nu_m = \nu_0 + m\nu_{RF}$, where m is an integer. If laser light of intensity I_{in} is incident on the crystal, then the relative light intensity in the mth order sideband is:

$$I_m/I_{in} = J_m{}^2\left(\delta\sqrt{P_{RF}}\right),$$

where δ is a constant determined by the crystal used, J_m is the Bessel function of order m, and P_{RF} is the power of the RF signal.

The laser frequencies in figure 5.2 differ by $\Delta\nu = 1712.7\text{MHz}$ and so it is possible to use EOMs with $\nu_{RF} = 1713$ or 856MHz to create both frequencies required for a MOT. The frequency sideband for the repump is higher than the trapping frequency. EOMs capable of running off $\nu_{RF} = 1712.7\text{MHz}$ RF input are more expensive, although they were used in most of the original sub-Doppler sodium experiments. This frequency allows more flexibility, as it is possible to independently vary the zeroth and first order sideband intensities. The $\nu_{RF} \approx 856\text{MHz}$ frequency was chosen however, necessitating the use of either the two first order sidebands, or the $m = 0$ and one of the $m = \pm 2$ sidebands. This is a slightly less versatile situation, as can be seen in figure 5.3
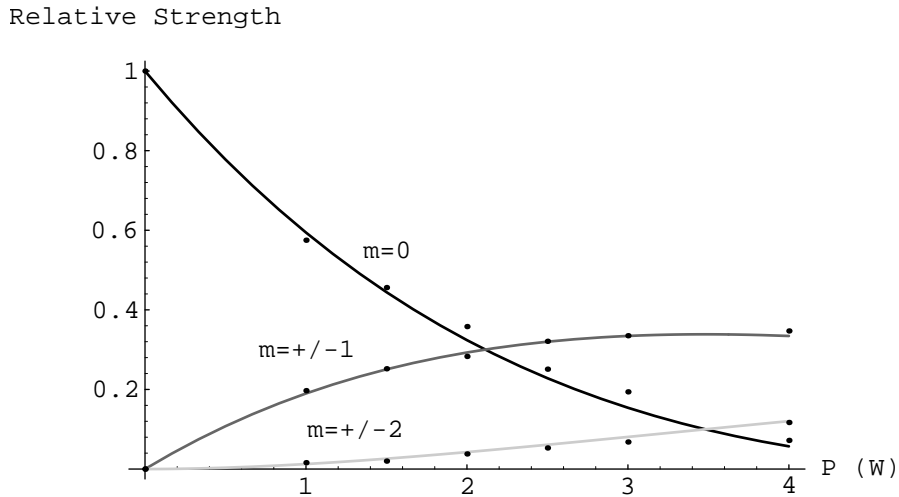

Figure 5.3: The relative strength of the sidebands produced by the EOM versus the input RF power, P_{RF}. The dots are experimental data and the solid lines correspond to theoretical curves for $\delta = 0.987\text{W}^{-0.5}$.

The EOM was a New Focus 4421, custom designed with an 856MHz resonant frequency and a Q value of 117 (these agreed with experimentally measured values, figure 5.4). The RF power supply was home-made and could lock to frequencies which were multiples of 2.5MHz—it was set to 857.5MHz while the MOT was in use.
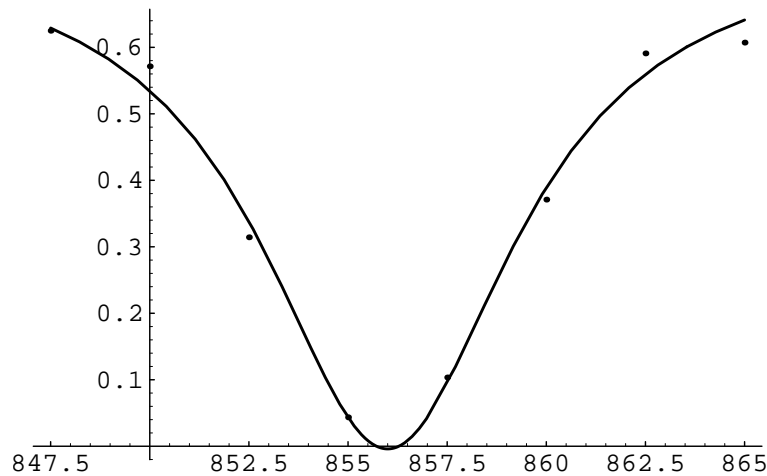

Figure 5.4: The power ratio, $P_{reflected}/P_{in}$, of the EOM versus ν_{RF} in MHz. Dots are experimental data, the solid line is a Lorentzian fit.

5.2.2 Other Components

After the laser left the optical fibre on the trapping table it passed through a convex lens (B in figure 5.1, $f = 30$cm) before it travelled through the EOM. The EOM was placed in a position near the laser beam waist to ensure that effects due to spatial variations within the crystal were minimised. Calculations had been made to ensure that the laser intensity was low enough to prevent photorefractive damage of the EOM.

A cylindrical convex lens (D in figure 5.1) was used after the EOM, to counteract the resulting laser beam expansion in the horizontal plane. Beam expander G consisted of an $f = 10$cm convex lens, followed by an $f = 50$cm convex lens which provided a $\times 5$ magnification in beam width. Beam expander H consisted of $f = 30$cm and $f = 50$cm convex lenses; creating $\times 2.5$ magnification.

The half-wave plate (I) adjusted the polarisation of the $x+y$ beam. Note that the x, y, and z lasers pass through a linear polariser (J), followed by a quarter-wave plate (K—a Fresnel rhomb) with its fast axis at the appropriate $\pm 45°$ angle to the axis of the polariser. The polariser+quarter-wave plate combination acts as a circular polariser, and the choice of $\pm 45°$ changes the helicity of the laser light. The helicities of each beam was chosen with the linear **B** field in mind, in order to provide a trapping (rather than repulsive) force at the centre of the MOT.

Rotation of the half-wave plate (I) caused different amounts of light to pass through the x and y linear polarisers, and the plate could therefore be used to adjust the intensities of the x and y beams. The beam splitter used to separate the x and y beams was set at an angle, in order to obtain a split ratio closer to 50/50.

After passing through the circular polarisers, the three Cartesian laser beams passed through separate axes of the glass cell. The cell consisted of a sphere of glass to which six cylindrical 'arms' were affixed, along the Cartesian axes. The 'arms' had planar windows through which the laser beams passed. An additional, thinner, arm was located on the $(1, 1, 1)$ axis of the cell and was used for observation. The cell contained a sodium reservoir, and extremely low pressures in the cell were maintained by an ion pump.

It should be noted that all of the optical components discussed so far have *not* been anti-reflection (AR) coated. The cell windows were not AR coated either. After the beams pass through the cell they next pass through quarter-wave plates (K'—these *were* AR coated), before being retroreflected along their original paths by mirrors. The presence of the second quarter-wave plate ensures that, after a double pass through the plate and a reflection from the mirror, the helicity of the light is optimal for trapping.

The cell was enclosed in a copper 'can' which was heated in order to provide an adequate vapour pressure of sodium in the cell. The cell was heated to $60°$C, at which temperature the vapour pressure is about $10^{-9} - 10^{-8}$Torr. Holes in the 'can' provided optical access to the cell.

Several magnetic field coils were also involved in the setup. A pair of anti-Helmholtz coils provided the linear magnetic field at the centre of the cell. Three pair of Helmholtz coils provided a constant magnetic field, with which to null the Earth's magnetic field. These coils will now be discussed.

5.3 Magnetic Fields

This section will deal with the nature of the magnetic fields necessary to produce MOTs and optical molasses. The speed with which they can be switched will also be considered. Optical molasses provides the best cooling in situations where the magnetic field is near zero, whereas a strong magnetic field is necessary in a MOT.

5.3.1 Helmholtz Coils

Using the Biot-Savart law it is relatively easy to derive the magnetic field along the axis of a current loop. If the loop has radius r, current I and z is a dimension along the coils axis, then the field has magnitude:

$$B_z(z) = f(z) = \frac{\mu_0 I}{2} \frac{r^2}{(r^2 + z^2)^{3/2}}$$

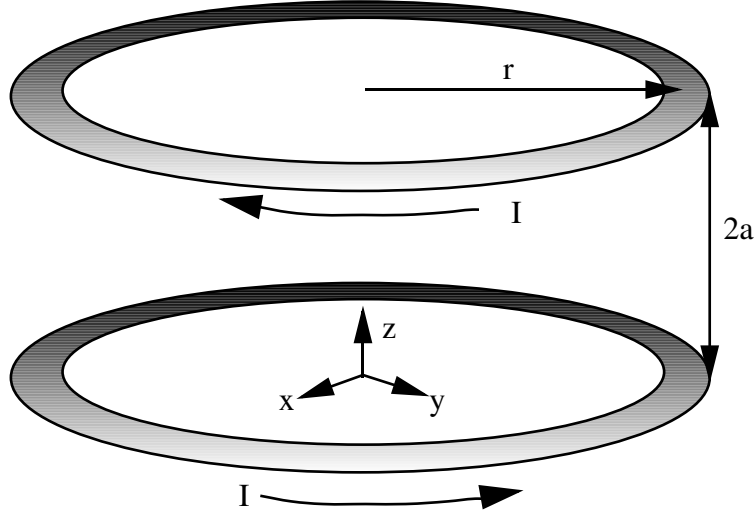and is directed along the axis (the sign is dictated by the right-hand rule).

Figure 5.5: An anti-Helmholtz coil configuration.

If two current loops (see figure 5.5) with the same axis are separated by a distance $2a$ then the magnetic field is of the form:

$$B_z(z) = B_H(z) = f(z - a) + f(z + a)$$

if the currents rotate with the same sense, and

$$B_z(z) = B_A(z) = f(z - a) - f(z + a)$$

if they rotate in opposite directions. The former is a Helmholtz configuration, and the latter is anti-Helmholtz. Both configurations yield a magnetic field that is solely radial and axial. The axial magnetic field is even in z for Helmholtz coils, and odd for anti-Helmholtz.

A Taylor expansion of the Helmholtz field therefore has the form:

$$B_H = b_0 + b_2 z^2 + b_4 z^4 + ...$$

By setting $b_2 = 0$ it is possible to obtain an axial field that is relatively constant near $z = 0$. Since $b_2 \propto \frac{d^2 B_H}{dz^2}$, it is straightforward to show that this arises precisely when $r = 2a$. These are 'true' Helmholtz coils, although the term is often used to describe coils with any separation. A similar calculation for the anti-Helmholtz coils shows that the axial field is relatively *linear* when $\frac{d^3 B_A}{dz^3} = 0$ or $\sqrt{3}r = 2a$—i.e. the separation of a given pair of coils increases compared to Helmholtz coils.

Analytic calculations of the magnetic field due to a current loop are not possible, due to the elliptic integrals involved [52], [66]. Taylor expansions of the fields can be taken about the point $r = z = 0$, (see ref. [71] for a third order expansion), or the fields can be found computationally. Although the anti-Helmholtz coils used in the MOT have the geometry $r \approx 2a$, computations showed that for distance scales comparable with the MOT size, the field is linear and of the form $\mathbf{B} = b(x, y, -2z)$. Care would have to be taken when using smaller coils however, or if a 'wobbling field' (used to measure the trap spring constant) pushed the atoms into a non-linear field regime.

The z magnetic field gradient at the centre of anti-Helmholtz coils, when each coil contains N current loops, is given by:

$$\frac{dB_z}{dz} = 3\mu_0 N I \frac{r^2 a}{(r^2 + a^2)^{5/2}}. \tag{5.1}$$

The anti-Helmholtz coils used in the experiment had $N = 50$, $a = 0.016$m, $r = 0.0375$m, and $I = 4$A, yielding a theoretical gradient ${B_z}' = 15$G/cm, in reasonable agreement with the experimental result: ${B_z}' \approx 13$G/cm.

Cancelling Background Fields

When the anti-Helmholtz coils are switched off to release the MOT atoms into a low magnetic field, the remaining magnetic field will be the background magnetic field. The main contributions to the background were the Earth's magnetic field, and the magnet on the ion pump. These fields are strong enough to disrupt sub-Doppler cooling [43] and need to be cancelled.

The background magnetic field is assumed to be approximately constant over the laser beam intersection. The background field can therefore be cancelled by a constant field, which is easily produced by Helmholtz coils. A single pair could cancel the field, however they would be difficult to orient. Three Helmholtz pairs along the Cartesian axes, and with independently controlled currents, were used. Rectangular coils were used instead of circular coils, as they can be joined to form a 'box' which is easily mounted around the 'can'. The dimensions of the box were approximately $27 \times 27 \times 13$cm, and although once again these are not the ideal Helmholtz separations for the coils, they provide adequate cancelling of the magnetic field near the centre of the MOT.

In order to measure the magnetic fields at the beam intersection, the cell was removed. A mount was made for the large magnet from the ion pump, in order to place the magnet close to its position prior to cell removal. Fields other than those due to the magnet and Earth should be small due to the lack of ferromagnetic material near the MOT. A modified ruler was used to hold a Gaussmeter and obtain magnetic field measurements at various positions in the trap. This information could then be compared with theoretical calculations of the magnetic field from the rectangular coils. The field from a rectangular coil is analytic, unlike the field from a circular coil.

The background magnetic field was measured to be $\mathbf{B}_{stray} = (420, -70, 970)$mG. The theoretical magnetic field generated in the cancelling coils when the field at the centre of the trap was zero, was $\mathbf{B}_{cancel} = (-430, 110, -1020)$mG. These fields add to zero, within 50mG, which was the experimental error of the field zero. After the magnetic field measurements the cell was replaced, and the measurements were repeated at a later time, yielding results within 50mG of the first experimental results. A 50mG magnetic field should still enable sub-Doppler cooling, which is typically disrupted in sodium when $B > 200$mG [42],[43].

Changes of 0.1A in a coil pair's currents typically produced a 100mG change in the field component associated with that coil pair. The orientation of the ion pump magnet had little effect on the $\mathbf{B}$ field: a ten degree rotation of the magnet altered the field components by < 50mG.

The field gradients in the stray magnetic field were also experimentally measured:

$$\frac{\partial B_x}{\partial x} = 19\text{mG/cm}, \qquad \frac{\partial B_y}{\partial y} = 8\text{mG/cm}, \qquad \frac{\partial B_z}{\partial z} = -28\text{mG/cm},$$

$$\frac{\partial^2 B_x}{\partial x^2} = 5.6\text{mG/cm}^2, \qquad \frac{\partial^2 B_y}{\partial y^2} = -1.4\text{mG/cm}^2,$$

and compare well with the theoretical Helmholtz coil results,

$$\boldsymbol{\nabla} \cdot \mathbf{B} = 0, \qquad \frac{\partial^2 B_x}{\partial x^2} = 6.2\text{mG/cm}^2, \qquad \frac{\partial^2 B_y}{\partial y^2} = -1.6\text{mG/cm}^2.$$

If these magnetic field gradients were substantial it would have been necessary to cancel the stray field gradients, as well as the constant term. This could have been achieved by controlling the six Helmholtz

coil currents independently, instead of in pairs. Two coils with independent currents I_1, I_2, are equivalent to a pair of Helmholtz coils with current $(I_1 + I_2)/2$ superposed with a pair of anti-Helmholtz coils with current $(I_1 - I_2)/2$. In this way both a constant term ($\propto (I_1 + I_2)/2$) and a gradient term ($\propto (I_1 - I_2)/2$) can be created in the cancelling field. The field gradients were insufficient to warrant any change of the existing current configuration however.

The only change made to the Helmholtz coils was to rewire the x and y coils from parallel to series, as the latter option guarantees a symmetric current distribution in the coils and hence a more constant, symmetric field.

5.4 Switching

5.4.1 Magnetic Field Switching

Once atoms have collected in the MOT, the magnetic field generated by the anti-Helmholtz coils needs to be switched off in order to induce enhanced sub-Doppler cooling. The field also has to be switched off *quickly*, otherwise the relatively hot Doppler atoms will escape, due to the reduced trapping forces, before sub-Doppler cooling slows the atoms.

How fast do the coils need to be switched off? Various authors have different switching times: the field is 'switched off' in less than 1ms [62], 2ms before the field drops to 1% [22], 20μs before the field drops to $1/e$ [25]), while some don't quote times at all [39], [50]. The faster the switching time, the faster the atoms will be cooled and less cloud expansion occurs. An approximate upper limit on the switch-off time can be found by assuming that the MOT atom cloud expands by less than 1mm in the switching time. Given that Doppler-cooled sodium atoms move at $\approx$ 1m/s, the field should be switched off in $<$ 1ms.

Probably the simplest way to switch off the magnetic field can be found in ref. [25], where a modified LR circuit is used. The current, and therefore magnetic field, in such circuits decays exponentially: $I = I_0 e^{-t/\tau}$, where $\tau = L/R$. The inductance of the coils, L, tends to be a good indication of how fast the coils can be switched of, as it is a measure of the inductive energy in the coils.

The self-inductance of a single circular coil, with circular cross-section, can be found using the formula [73]:

$$L = 0.628N^2 D(\ln(8D/d) - 1.75) \ \mu\text{H} \tag{5.2}$$

where the coil has diameter D (metres), N turns, and a cross-sectional diameter d. The dimension d of the anti-Helmholtz coils used in the experiment was $d = 0.01$m, and the theoretical self-inductance of one of the coils is thus $L = 276\mu$H.

One interesting thing about the self-inductance of a current loop is that the current cannot be approximated to flow through an infinitely thin wire—this leads to an infinite flux within the current loop, and Lenz's law breaks down. It is only when the current is distributed through a finitely thick wire that calculations start to agree with equation 5.2.

The two current loops used in the experiment have a theoretical total self-inductance of $L = 552\mu$H. Because the pair are anti-Helmholtz the mutual inductance subtracts from the self-inductances, and the theoretical inductance of the coils (using the elliptic integrals of ref. [66]) is $L = 436\mu$H, which compares well with the experimentally measured $L = 460\mu$H. If it were necessary to change the coils then one might wish to maximise the field gradient (equation 5.1) whilst minimising the inductance of the coils. This was not necessary for this MOT, but would be important if the coils were to be used in BEC experiments.

Replicas of the experimental coils were made in order to perform switching tests, as one of the MOT coils was wrapped around the cell. Experiments using an exponentially decaying LR switching circuit were performed, however due to the high L value of the coils, large resistors were necessary to lower the time constant τ. The coils need to operate at around $I = 4$A when the MOT is operational, and so any significant resistance would generate a lot of heat. Diodes were also considered, instead of resistors, as they have a

'resistance' which increases as the current in a circuit drops. This gives a faster-than-exponential current decay, however large quantities of diodes, with heat-sinking, would be necessary at 4A.

A circuit consisting mainly of two power MOSFETs was eventually chosen. The circuit relies in an integral way on the Zener diodes that are built into the MOSFETs, although these could have been added in parallel. The switch off time is relatively rapid, $\approx 15-20\mu s$, in which the current linearly decays to zero. The switching circuit generates very little heat.
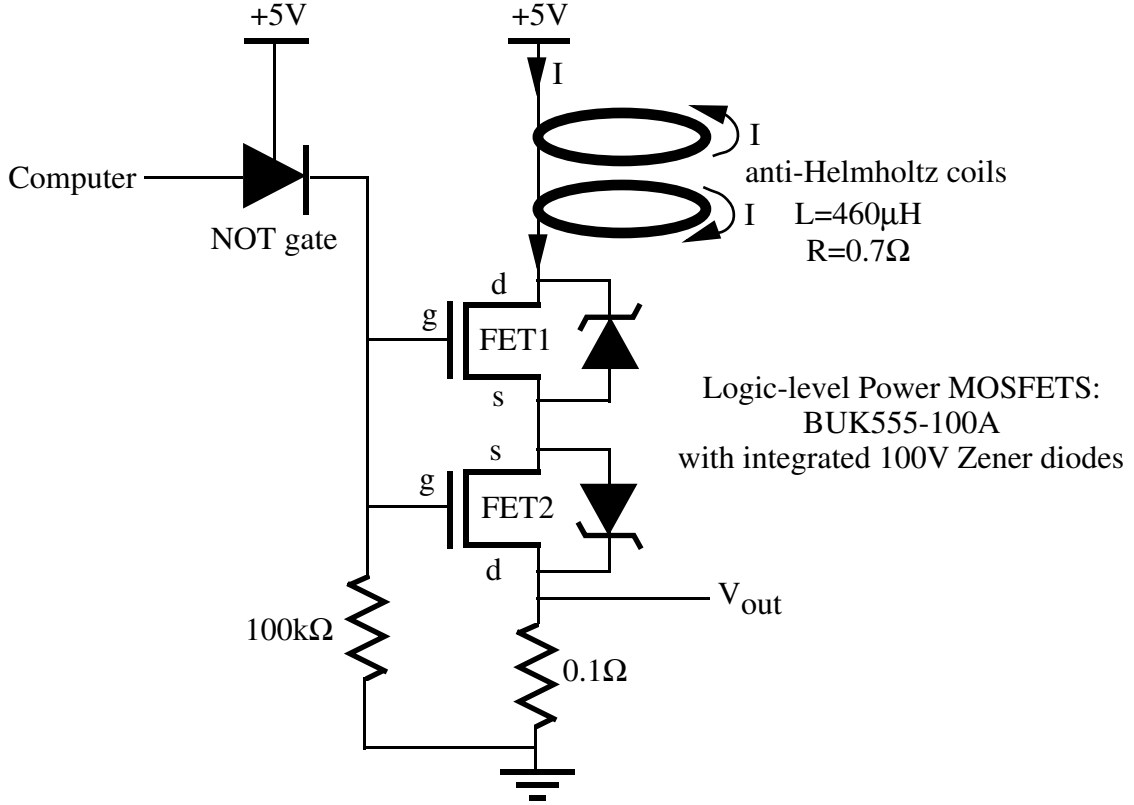

Figure 5.6: The magnetic field switching circuit. The FETs have on-state resistance of $\approx 0.1\Omega$. Voltage V_{out} can be used to determine the current in the coils. The power supply must be voltage-limited.

The computer could generate a $0V \rightarrow 5V$ transition, triggered by an inbuilt timing board. The NOT gate therefore sent a signal that initially switched the FETs on (while trapping occurred) and then switched them off at a given signal. An SN74LS00N NAND gate, with its inputs connected, was used as the NOT gate in figure 5.6 initially. A line-driving 74HC04 NOT chip, with the NOTs in parallel, was then used as the NOT gate. The line-driver chip was required to ensure sufficient current was supplied to the FETs, so their capacitances could quickly charge and the FETs could switch. The substitution of the line-driver did not improve the switching speed, and so the SN74LS00N chip would probably suffice.

With the FETs switched on, the total resistance of the coil circuit is 1Ω and thus 4-5V across the coil circuit creates a current of $4-5$A. If the FETs are switched off the current through the coils drops. Due to the coils' inductance, a voltage $V = -L\frac{dI}{dt}$ develops across the coils, directed to keep the current flowing. No passage for the current is offered through the FETs, and so the current drops rapidly, causing a high voltage to build up across the coils. Once the voltage reaches the Zener breakdown voltage, V_Z, current flows through the Zener attached to FET1, and through the forward-biased Zener in FET2. Due to the nature of a Zener diode, the voltage across the reverse-biased Zener will stay at $\approx V_Z$. If this voltage drops below V_Z the current will stop, and the coils' voltage will increase to V_Z again. If the current increases then the voltage across the Zener stays approximately the same (a Zener diode can draw almost any current when it has $\approx V_Z$ across it). The equation $-L\frac{dI}{dt} \approx V_Z$ therefore holds when the FETs switch off. This is a linear differential equation, and it is straightforward to show it has solution $I(t) = I_0 - V_Z t/L$.

The current theoretically drops to zero at $t_{off} = I_0 L/V_Z$, and with $I_0 = 4$A, $V_Z = 100$V, $L = 460\mu$H this leads to $t_{off} = 18\mu$s, in agreement with the measured switching time. The additional FET, FET2, was incorporated to ensure the current didn't become negative after reaching zero, however this FET is not actually necessary for successful switching however. The current should spend as little time flowing negatively as possible, as in such a regime the magnetic fields reverse, repelling atoms from the trap, rather than attracting them.

The arrangement of the Zeners (drain-source-source-drain) was necessary to create a large enough gate-source voltage V_{gs} across both Zeners (the s-d-d-s configuration destroyed the FETs). The switching time of the circuit can be changed by putting Zener diodes, with lower breakdown voltages, in parallel with the 100V Zeners (which are incorporated in the MOSFET packages). New values of t_{off} can be found by replacing V_Z with the lower Zener voltages.

Separate voltage supplies could be used for the coils and the NOT gate, however using a single supply is more efficient, and works just as well, when the supply voltage is kept above the minimum required by the NOT.

5.4.2 Intensity Switching

An ISOMET acousto-optic modulator (AOM) was used to switch laser intensity. AOMs are similar to EOMs in that they have an RF signal as an input, and the RF field in the crystal creates sidebands, differing by integral multiples of the RF frequency, on the carrier frequency. The two modulator types work on different principles however: the EOM acts via an oscillating refractive index, whilst the AOM is equivalent to a moving diffraction grating due created by sound waves within the crystal. Conservation of momentum requires that the 'sideband' frequencies leave the AOM at different angles, with approximately the same angle between the mth and $(m + 1)$th order modes.

The angle between modes is frequency dependent, and the intensity of light in the sidebands depends on the input RF power (as was the case with the EOM). A large amount ($> 80\%$) of the input laser power can be shifted into a first-order sideband of the AOM. The RF power can be adjusted, in order to control the intensity of light in this sideband, and so the first order sideband can be used as a constant-frequency, variable intensity light source. Arrangements are possible in which two AOMs, or a double pass through a single AOM, create a light source which can have variable frequency as well as intensity—such a configuration is unnecessary for sub-Doppler cooling however, as was pointed out at the start of the chapter.

The AOM's RF power signal could be attenuated by a voltage controlled attenuator (VCA) and the intensity in the $m = 1$ sideband was calibrated against the VCA voltage. It was later found that the VCA was unnecessary, and in fact a TTL 'switch' in the AOM power supply worked just as effectively, if it was sent an accurate voltage in the range $1 - 2$V. The switching speed was mainly limited by the voltage signal from the computer timing board's D/A converter: the D/A voltage could change at maximum rate 5V$/30\mu$s.

Care must be taken to ensure the laser light is switched off quickly. Lett *et al.* [43] found that the temperature of sodium molasses decreases with intensity, down to a critical intensity below which the temperature rises. This critical intensity is not observed in caesium. As sub-Doppler mechanisms act on time-scales of the order of 3μs, intensity switching in sodium molasses has to be faster than this or the molasses temperature will change with intensity during switching. Lett *et al.* [43] used an AOM with a switching speed of a few hundred nanoseconds.

5.5 Experiments with Switching

5.5.1 Motivation

The final aim of the experiments was to drop both the intensity and magnetic field, in order to cool the atoms to sub-Doppler temperatures. For this reason a computer program was written which used a timing board to send signals to an AOM, as well as the magnetic field switching circuit shown in figure 5.6. The two signals were created by separate counters on the same chip. It was possible to enter a magnetic switching time (t_B, accurate to $\pm1\mu$s) as well as an intensity switching time (t_I, accurate to $\pm3\mu$s). Once a MOT was formed the intensity could be dropped to a new, lower, level at $t = 0$. The magnetic field would then switch off at $t = t_B$ and the intensity would turn off at t_I. The accuracy of the timing was checked experimentally.

This was the ultimate goal, however a preliminary, relatively simple experiment was performed. In this experiment a MOT was formed at relatively low intensity, to ensure sub-Doppler effects, and then the magnetic field was switched off. The intensity was held constant throughout. Leaving the lasers on ensures that a frictional force acts on the atoms, instead of the ballistic expansion if the light is turned off.

Atoms with x temperature T_x, expanding ballistically from the point $\mathbf{r} = \mathbf{0}$, are subject to the statistical formula:

$$\sqrt{\overline{x^2}} = \sqrt{\frac{k_B T_x}{m}}\, t$$

which can be contrasted to the expansion rate in the molasses obtained if a MOT's magnetic field is removed and the lasers are left on,

$$\sqrt{\overline{x^2}} = \sqrt{\frac{k_B T_x}{\alpha_x}t} \tag{5.3}$$

Equation 5.3 is valid for both Doppler and sub-Doppler regimes, as long as the associated temperatures and damping constants are used. In particular Doppler theory predicts that $\sqrt{\overline{x^2}} \propto \sqrt{I}$ whereas the sub-Doppler counterpart is $\sqrt{\overline{x^2}} \propto 1/\sqrt{I}$.

Both molasses cooling mechanisms lead to extremely slow expansion rates, with sub-Doppler expansion slower than Doppler. If the laser intensities are balanced, then Doppler theory predicts that after 100ms an atomic cloud acted on by light with intensity $I_{tot}/I_S = 0.6$ and detuning $2\Delta/\Gamma = -1$, will expand to $\sqrt{\overline{x^2}} = 1$mm. Ballistically expanding atoms at $T_x = 240\mu$K acquire an rms x value of $\sqrt{\overline{x^2}} = 30$mm over the same time: quite a significant difference. At first it would appear that the experiment should allow extremely long observation times of the atoms in molasses, and a CCD camera connected with video equipment could grab several frames of data (the frame time was 40ms). The CCD camera would not be able to obtain many frames of atoms under ballistic expansion however.

The problem with the above results is that the intensity is never perfectly balanced. Doppler theory predicts that even a 10% imbalance in intensity, with the previous laser parameters, leads to a drift velocity of $v_{drift} = 18$cm/s and the atoms leave the laser beam intersection at approximately the same rate as a ballistic expansion.Sub-Doppler cooling, with its larger friction constant, leads to lower drift velocities, but is still affected by intensity imbalances. In order to obtain meaningful measurements of temperatures, as well as long confinement times, the drift velocity must be zeroed.

Note that while gravity has a strong affect when an atomic cloud expands ballistically, it has very little effect in molasses. The atoms acquire a (very small) constant downward drift velocity.

5.5.2 The Experiment

When the MOT had formed, the number of atoms in the MOT was maximised by adjusting the detuning. A TTL square wave with frequency ≈ 0.2Hz was applied to the magnetic field switching circuit. This caused the MOT to cyclically build up, followed by a release into molasses. The cell images were recorded on the CCD, but successive frames contained only the MOT, or no MOT, with no intermediate frames. Adjusting the detuning or intensity had no effect.

The molasses clearly had an associated drift velocity. It can be shown, in a manner similar to that of subsection 2.2.7, that intensity imbalances in a MOT can be counteracted by adjusting the background magnetic field. This was attempted, but to no avail—the direction that the molasses was travelling could not be seen, so it was extremely difficult to cancel the drift velocity.

5.5.3 Improving the MOT

It was postulated that the fast disappearance of the molasses was due to a drift velocity caused by intensity imbalances. The fact that the counterpropagating laser beams passed through optical surfaces which were not AR coated meant that they had lower intensity than their counterparts. This imbalance can be reduced by making the laser beams converging, rather than collimated, in the trapping region of the MOT.

EOM

Another possibility was that there was in fact a spatial variation of the intensity imbalance across the laser beams, due to imperfect laser profiles. This problem was implicated by the non-Gaussian shape of the MOT atom cloud. Magnetic fields can only counteract intensity imbalance ratios that are constant across counterpropagating laser beams. Large spatial fluctuations in intensity, slight misalignments in the reflected laser beam and converging/diverging laser beams all lead to spatial variations in the intensity imbalance. The spatial intensity variations in the MOT were traced to the EOM—the laser beam exiting the EOM was far from Gaussian.

The EOM was shifted from its original position on the trapping table to the laser table. By placing the EOM before the optical fibre, it was possible to use the fibre as a spatial filter. Although the EOM still distorted the beam, the laser beam which exited the single-mode fibre was Gaussian. The efficiency of the fibre was reduced by this modification: 60% without the EOM, and 30% with the EOM before the fibre.

Before the EOM was shifted it was necessary to compare the waists of the beam on both the trapping and laser tables, to ensure photorefractive damage would not occur. The waist on the laser table was measured to be three times larger, and so nine times more power could be used in the laser beam at that point; considerably more than was lost through the fibre efficiency.

The Field Coils

The anti-Helmholtz coils, like the Helmholtz coils, were slightly altered. Initially one of the coils was attached to the cell, whilst the other rested on a stand in the 'can'. It was difficult to position the cell on top of the lower coil without causing stress on the fragile cell. Also, if the lower coil is too low, then the magnetic field zero is no longer in the centre of the cell. The lower field coil was therefore strapped onto the cell.

The centre of the magnetic field was measured experimentally to ensure that it coincided with the centre of the cell. A large square-wave current was put through the anti-Helmholtz coils using the field-switching circuit. A loop of wire made from the end of a coaxial cable provided a means to measure the rate of change of flux in the loop with time (Lenz's law states that a voltage is induced in a loop of wire proportional to the rate of change of the flux through the loop).

The flux in the loop due to the anti-Helmholtz coils is proportional to the magnetic field from the anti-Helmholtz coils, and the rate of change of current in these coils. The induced voltage in the loop can only be zero if the flux through the loop is zero. The radial nature of the field from the coils means that the flux will be zero if the loop of wire is in a radial plane of the coils' field, and will stay zero while the loop is moved in this plane. This makes it relatively easy to find (two or more) radial planes in which the magnetic field zero lies, and thus find the axis of the magnetic field. The coils were positioned on the cell so that magnetic axis coincided with the cell's geometric axis. A similar technique can be used to find the plane between the coils in which the field zero lies and can be combined with the coil axis result to indicate

the coils' magnetic field zero. Note that this technique uses a fluctuating field (provided only by the coils) and DC magnetic field terms do not affect the result.

With both field coils attached to the cell, shifting the cell within the can became relatively easy, and the cell was shifted to a position where the beams passed more clearly through the cell windows.

Relative Beam Intensities

The intensity of the z laser beam was measured to be four times more intense than the intensities of the x and y beams. In order to create a more isotropic molasses, the lenses of the z confocal beam expander (H) were changed to have the same focal lengths as the $x + y$ confocal beam expander (G)—this removed the intensity discrepancy caused by the differing expansion ratios.

In the initial MOT arrangement, a single half-wave plate (I) was used to rotate the polarisation of the light and thus optimise the intensities of both the x and y MOT beams. The orientation of the linear polarisers for the x and y beams means that the optimum polarisation required by the x beam linear polariser is exactly the opposite required by the other linear polariser—if the intensity in one beam is maximised the other becomes zero. An additional half-wave plate was incorporated in the setup to allow independent adjustment of the x and y beam polarisations/intensities.

Intensity Imbalances

Shifting the EOM to the laser table meant there was no longer any requirement for lenses B and D. This changed the laser beam waists and their degree of collimation—affecting the intensity balance. For this reason the cell was removed and the intensities of counterpropagating laser beams were measured by picking off a fraction of both beams with a thin piece of flat-surfaced glass at 45° to the beam (figure 5.7). The intensities of the original beams were calculated using the transmission of the glass. The effect of removing the cell was also included, by measuring the transmission of the cell windows. The confocal beam expanders were used to adjust the collimation of the beams and counter intensity imbalances.
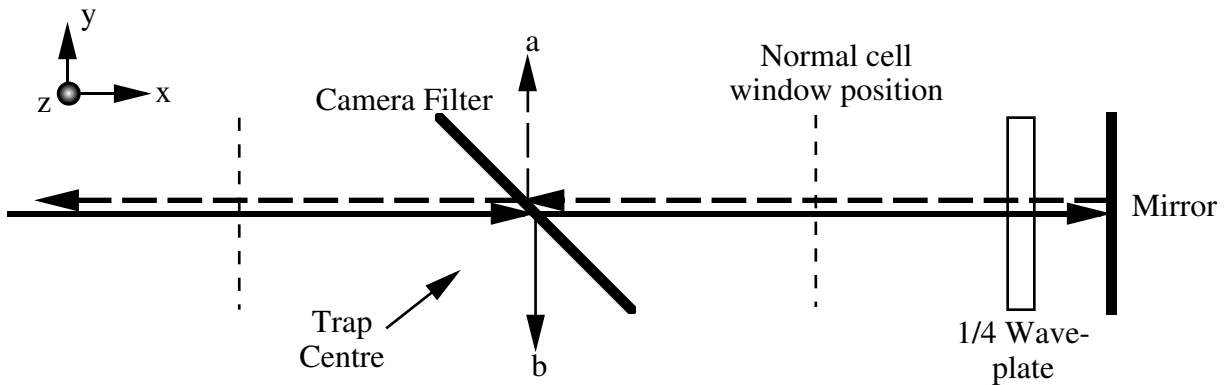

Figure 5.7: Arrangement for measuring the x intensity imbalance (the y and z measurements were similar). Bold arrows indicate parts of the laser beam travelling in the $+x$ direction, whereas dashed arrows are used for the retroreflected beam. The intensities at positions 'a' and 'b' were used to determine the intensity imbalance near the centre of the cell.

5.5.4 Results

With the improvements to the MOT discussed previously, there was a marked improvement in the trap. The beams were much smoother, and this lead to improved trapping—the initial MOT ceased to work once the laser power out of the fibre was below 30mW, but the equivalent power dropped to 4mW with the improvements.

With 50mW laser light out of the fibre it was possible to obtain MOTs at five different laser frequencies: 'type I' traps at (relative) laser frequencies of 0.54GHz, 1.44GHz, 2.34GHz, 3.24GHz as well as a type II MOT at 2.4GHz. This was surprising because one of these traps involves a third order sideband from the EOM, which would be very weak. The weak sideband was at the repump frequency, indicating that very little repump light is necessary for a MOT.

One of the quarter-wave plates (K') was briefly removed from the apparatus, however the MOT was not destroyed. This result suggests that the cell may in fact be birefringent, or that it is possible to trap with a σ^+–σ^+ configuration (ref. [36] discusses traps that do not rely on σ^+–σ^- polarisation).

Switching the magnetic field did not yield a cloud of slow molasses atoms, however the improved MOT yielded molasses atoms that expanded slowly enough (or rather had low enough drift velocity) to be seen on the video frames. During each switch-off only one intermediate video frame could be obtained, however, and these were obtained by optimising the laser detuning. Attempts to counter the drift velocity with a non-zero background field did not lead to improvements. The direction of the atoms' flight was not reproducible, and therefore the drift velocity was difficult to zero. Video frames could not be obtained for the type II trap—the atoms moved too fast.

Low transmission of retroreflected laser beams in the MOT ($T < 70\%$ in some instances, mainly due to the cell) created the need for strongly converging beams in order to counter intensity imbalances. This causes a spatially varying intensity imbalance across the beams that is not present if the laser beam are collimated. Attempts to observe molasses using collimated laser beams did not provide any improvements to the molasses lifetime.

Spatial structure was observed in the MOT. Small changes in beam alignment caused the position of the MOT to jump discontinuously. The shape of the atomic cloud was often decidedly non-Gaussian, and the cause appeared to be scratches on the cell windows which caused roughness in the laser beam intensities.

5.5.5   Conclusions

Type II MOTs rely on Doppler cooling mechanisms, whereas type I MOTs can have sub-Doppler processes. Video frames of the type I molasses could be observed, but this was not true of type II molasses, implying the type I molasses was slower. Indirect evidence that sub-Doppler processes are occurring in molasses has therefore been obtained. The molasses attained with the present apparatus has either a high temperature or drift velocity however.

In order to obtain a long-lived molasses it may first be necessary to replace the sodium cell. The scratches on the cell windows appear to cause spatially varying intensity imbalances which can therefore not be cancelled with non-zero magnetic fields. Other optical components could be checked for their role in the beam quality.

If the cell was replaced it would also be important to include more than one observation port in the cell. With the single observation window of the existing cell, drift velocities can only be observed in two dimensions. Zeroing such velocities is therefore difficult. The new cell could be AR coated, to improve intensity imbalances. The cell pressure could also be lowered, decreasing the effect of energetic background atoms on the MOT/molasses.

A new EOM might improve the molasses, as some groups appear to have found it necessary to replace their 856MHz EOM with a 1732MHz EOM in order to obtain low sub-Doppler temperatures [68], [78]. An 866MHz EOM might be a good compromise, as an 856MHz EOM will yield both trapping and repump light resonant with atomic energy levels. If the trapping light is detuned by 20MHz then this is also true of the repump light, and the repump will only be absorbed at $1/17$ of the resonant rate. If an 866MHz EOM were used then the zeroth order mode could be used for a 20MHz detuned trapping laser, and the $m = +2$ mode could be used as a resonant repump with approximately 10% of the carrier intensity, similar to the arrangement in refs. [43], [78]. Although an $m = 0, +2$ sideband MOT is possible with the present set-up, the trap is not as strong as the $m = -1, 1$ MOT, which has equal intensities of repump and cooling light.

An 866MHz EOM would strengthen the $m = 0, +2$ sideband MOT, also allowing the ability to change the relative strengths of the repump and trapping light.

The present x and y beams have different optical path lengths (see figure 5.1) and this will give rise to different degrees of convergence for the beams at the centre of the cell, making it impossible to balance both the x and y counterpropagating beams intensities. The beamsplitter which separates the x and y beams was not set at a 45° degree angle, as this ensured the x and y beams had similar intensities (the polarisation of the laser changed the ratio of the 50/50 beamsplitter). The relative intensities of the x and y beams are less important than the relative intensities of counterpropagating beams however and so it might be useful to set the beamsplitter at a 45° degree angle.

With the suggested improvements it should then be possible to obtain a long-lived molasses by zeroing the drift velocity with a constant magnetic field. Lower intensity imbalances require smaller magnetic fields, and therefore lead to lower temperatures. Thus zeroing the intensity imbalance will improve the molasses (early sub-Doppler molasses were observed in set-ups with imbalances less than 1% [43]). It was difficult to measure intensity imbalance in the lab, due to intensity fluctuations caused by both the laser and the rotating polarisation from the fibre.

The expansion of a long-lived atom cloud would be dictated by equation 5.3, and the ratio of temperature and damping constant, $\psi = T/\alpha$, could be measured and compared with Doppler and sub-Doppler theories. A new cell, with good optical access, would also allow time-of-flight temperature measurements to be taken. These 'direct' temperature measurements would mean that α could be obtained from ψ. Given the temperature and spatial size of the atom cloud, the spring constant, κ, can be determined The damping and spring constants can also be determined by 'wobbling' the trap centre with a magnetic field, although experimental measurement of the spring constant remains somewhat problematic [74]. The 'direct' method of determining α and κ is possibly more accurate than the perturbative methods ('wobbling' with a field or pushing the trap with a laser beam).

By ensuring that intensities are low it would be possible to neglect the effects of forces from reradiation and absorption on the molasses. These forces lead to a more rapid expansion of the atomic cloud. Experiments on the effects of the relative timing of both the intensity and magnetic field switching could be carried out. The effect of switching speed could also be considered.

Appendix A

Expectations of Spontaneous Emission

In the section on the Monte Carlo simulation dealing with spontaneous emission, probability distributions of spontaneous emission were stated. The distribution of spontaneous photons varies, depending on the dipole moment excited in an atom. If the atom is excited by π light polarised along the z axis, then the relative probability distribution of emitted light, over an area dA, is given [15] by:

$$P_\pi(\theta, \phi) = \sin^2 \phi \, dA.$$

The corresponding probability for a circular dipole moment in the x-y plane, excited by circularly polarised light travelling along the z axis is:

$$P_\sigma(\theta, \phi) = (1 + \cos^2 \phi) \, dA.$$

As the probabilities involved are relative probabilities, then the expectation value for an observable of the emitted photons, ϵ, when averaged over all emission directions is:

$$\bar{\epsilon} = \frac{\iint \epsilon \, P_{\sigma/\pi} \, dA}{\iint P_{\sigma/\pi} \, dA}.$$

The observables of interest are (cf. equation 2.37):

$$p_x{}^2 = p^2 \sin^2 \phi \cos^2 \theta,$$

$$p_y{}^2 = p^2 \sin^2 \phi \sin^2 \theta,$$

$$p_z{}^2 = p^2 \cos^2 \phi,$$

where $p = \hbar k_L$.

The probabilities will be integrated over the area of a unit sphere, as this includes all emission directions. The area element of such a sphere is $dA = \sin \phi \, d\phi \, d\theta$. The expectation value of the squared x component of momentum, $\overline{p_x{}^2}$, for spontaneous emission from light excited by a σ transition is thus:

$$\overline{p_x{}^2} = p^2 \frac{\int_0^{2\pi} \cos^2 \theta d\theta \int_0^\pi \sin^3 \phi \, (1 + \cos^2 \phi) \, d\phi}{\int_0^{2\pi} d\theta \int_0^\pi \sin \phi \, (1 + \cos^2 \phi) \, d\phi}.$$

The following mathematical result proves useful:

$$\int_0^\pi \sin^{2x-1} \phi \, \cos^{2y-1} \phi \, d\phi = \beta(x, y) = \frac{\Gamma(x)\Gamma(y)}{\Gamma(x+y)},$$

where y is not an integer, as the integral is then zero. The function Γ refers to the gamma function, for which $\Gamma(x + 1) = x\Gamma(x)$. From these equations it is clear that:

$$\overline{p_x{}^2} = p^2 \frac{(\pi)(\frac{\Gamma(2)\Gamma(0.5)}{\Gamma(2.5)} + \frac{\Gamma(2)\Gamma(1.5)}{\Gamma(3.5)})}{(2\pi)(2 + \frac{\Gamma(1)\Gamma(1.5)}{\Gamma(2.5)})} = p^2 \frac{(1)(\frac{\pi^{1/2}}{1.5 \times 0.5\pi^{1/2}} + \frac{0.5\pi^{1/2}}{2.5 \times 1.5 \times 0.5\pi^{1/2}})}{(2)(2 + \frac{0.5\pi^{1/2}}{1.5 \times 0.5\pi^{1/2}})} = \frac{3p^2}{10}.$$

The other averages for emission from a σ dipole, obtained in a similar manner, are: $\overline{p_y{}^2} = \frac{3p^2}{10}$ and $\overline{p_z{}^2} = \frac{2p^2}{5}$. The corresponding results for emission induced by a π transition are: $\overline{p_x{}^2} = \frac{2p^2}{5}$, $\overline{p_y{}^2} = \frac{2p^2}{5}$ and $\overline{p_z{}^2} = \frac{p^2}{5}$.

Appendix B

Multi-directional Heating

The necessity of extending the 1D description of spontaneous heating arises because in the 1D setting Δv_x was constant. If this parameter fluctuates with time then the atomic behaviour cannot be modelled as the average of distinct constant-Δv_x processes. The following description allows Δv_x to vary after each spontaneous emission.

Consider, at time $t = t_{old}$, an atom with a distribution of n possible x velocities: v_{x_i} ($i \in \{1, ..., n\}$) and the limit $n \to \infty$ can be taken for a continuous distribution of velocities). The probability that the atom has velocity v_{x_i} is denoted by p_i and the expectation value of the velocity squared at time $t = t_{old}$ is therefore $\overline{v_{x_{old}}^2} = \sum_{i=1}^n p_i v_{x_i}^2$.

If at time $t = t_{new} = t_{old} + \delta t$ (where $\delta t = 1/R$) a spontaneous emission occurs which changes the atom's velocity by $\pm \Delta v_x$ (with equal probability of $+$ or $-$ due to the symmetry of emission), then the probability the atom's velocity is either $v_{x_i} + \Delta v_x$ or $v_{x_i} - \Delta v_x$ is $p_i/2$. Each time step creates a step in the probability tree of the atom's velocity. The squared velocity expectation value after emission (at $t = t_{new}$) is given by:

$$\overline{v_{x_{new}}^2} = \sum_{i=1}^n (p_i/2) \left((v_{x_i} - \Delta v_x)^2 + (v_{x_i} + \Delta v_x)^2 \right) = \overline{v_{x_{old}}^2} + (\Delta v_x)^2. \tag{B.1}$$

Thus the increase in $\overline{v_x^2}$ after a single spontaneous emission depends solely on Δv_x—the velocity recoil of the emitted photon. If the term $R(\Delta v_x)^2$ in equation B.1 is replaced by the sum of all possible values $(\Delta v_x)^2$ weighted by the rate the atom will receive a velocity change of size Δv_x, then a value for the expected time evolution of $\overline{v_x^2}$ can be found—hence equation 2.14.

Appendix C

Sample File From the MC

```
/* Three dimensional Doppler simulation keeping track of probability */
/* distributions in two Cartesian planes. Isotropic spontaneous emission */
#include <stdio.h>#include <stdlib.h>
#include <math.h>#include "myutil.h"
#define pi 3.1415927
float ran2(long *idum); double it;
int main(int argc,char *argv[])
{
 int n,t,tmax,tot,totd,m;    long *idum;
 double R,R2,X,Y,Z,f,v0,p,q,l,del,gam,r1,r2,r3,r4,r5,r6,r,jd,jv;
 double X2,Y2,Z2,B,t1,t2,k,b,is,s,I1,I2,I3,I4,I5,I6,dmax,vmax;
 double i01,i02,i03,i04,i05,i06,hk,c1,w1,w2,w3,w4,w5,w6,d;
 double ip1,ip2,ip3,ip4,ip5,ip6,im1,im2,im3,im4,im5,im6,xbar,ybar,zbar;
 double xo,xn,vx,vX,yo,yn,vy,vY,zo,zn,vz,vZ,T,*Tbar,*V,*D;
 double **XY,**XZ,**VXY,**VXZ,i1,i2,i3,i4,i5,i6; FILE *fp;
 double rate(double arg1,double arg2); extern double it;
/* declaration of variables */
 tmax=atoi(argv[1]);          /* number of absorption/emission cycles */
 jv=atof(argv[2]); jd=atof(argv[3]);      /* number of velocity and position 'bins' */
 totd=2*nint(jd)+1;        tot=2*nint(jv)+1; /* parameters for the 'bins' */
 dmax=0.006;             vmax=1.0;          /* maximum position/velocities considered */
 VXY=dmatrix(1,tot,1,tot); VXZ=dmatrix(1,tot,1,tot); XY=dmatrix(1,totd,1,totd);
 XZ=dmatrix(1,totd,1,totd); V=dvector(1,tot); D=dvector(1,totd);
 T=0;                 /* initial time */
 idum=(long *)malloc((size_t)sizeof(long));    *idum=(-1);
 k=2.0*pi*10000000/5.89;  /* wavevector of Na */
 hk=k*1.055/23.0/1.67/10000000.0;   /* hk=k*hbar/m - vel. recoil from one photon */
 b=1.602/2.0/9.109*10000000000;
 b=14*b;    /* B field 14G/cm on x,y axes)   B=b(x,y,-2z) */
 gam=2.0*pi*10000000.0;  /* linewidth */
 c1=2.0/gam; del=-2.5*gam;   /* detuning */
 t2=1.0/gam;  /* spontaneous emission time */
 w1=0.0072*0.0072/2;   w2=w1; w3=w1; w4=w1; w5=w1; w6=w1;   /* beam waists */
 s=0.007/2; /* beam separation */
 is=1.0;     i1=0.5/is; i2=i1; i3=2*i1; i4=2*i1; i5=i1; i6=i1;
/* On-axis beam intensities (in units of the saturation intensity) */
```

```
  vx=hk;   vy=hk;   vz=hk;   xo=0.005;   yo=0.00001;   zo=0.00001;
    /* initial velocity and momentum of atom */
for (n=1;n<=tot;n++)
{V[n]=vmax*((double) (n-1-(tot-1)/2))/jv;
for (t=1;t<=tot;t++)   { VXY[n][t]=0; VXZ[n][t]=0;  }}
for (n=1;n<=totd;n++)
{D[n]=dmax*((double) (n-1-(totd-1)/2))/jd;
for (t=1;t<=totd;t++)    { XY[n][t]=0; XZ[n][t]=0;  }}
/* preparing the velocity and position matrices */

for (t=1;t<=tmax;t++)
{ /* one loop corresponds to one photon absorption/emission cycle */
    X=xo;   Y=yo;   Z=zo;   X2=X*X;   Y2=Y*Y;   Z2=Z*Z;
    R2=X2+Y2+4*Z2;   R=sqrt(R2);   B=b*R;         /*position and magnetic field */
I1=i1*exp(-((Y-s)*(Y-s)+Z2)/w1);        I2=i2*exp(-((Y+s)*(Y+s)+Z2)/w2);
I3=i3*exp(-((X+s)*(X+s)+Z2)/w3);    I4=i4*exp(-((X-s)*(X-s)+Z2)/w4);
I5=i5*exp(-(X2+Y2)/w5);                      I6=i6*exp(-(X2+Y2)/w6);
it=I1+I2+I3+I4+I5+I6;
i01=0.5*(1-X2/R2)*I1; i02=0.5*(1-X2/R2)*I2;
i03=0.5*(1-Y2/R2)*I3; i04=0.5*(1-Y2/R2)*I4;
i05=(0.5-2*Z2/R2)*I5; i06=(0.5-2*Z2/R2)*I6;
ip1=.25*(1+X/R)*(1+X/R)*I1; ip2=.25*(1-X/R)*(1-X/R)*I2;
ip3=.25*(1+Y/R)*(1+Y/R)*I3; ip4=.25*(1-Y/R)*(1-Y/R)*I4;
ip5=.25*(1+2.0*Z/R)*(1+2.0*Z/R)*I5;    ip6=.25*(1-2.0*Z/R)*(1-2.0*Z/R)*I6;
im1=I1-i01-ip1; im2=I2-i02-ip2;
im3=I3-i03-ip3; im4=I4-i04-ip4;
im5=I5-i05-ip5; im6=I6-i06-ip6;
/* calculation of the pi and sigma intensities from each laser beam */
   d=del-k*vx; r1=(rate(i01,c1*d)+rate(im1,c1*(d+B))+rate(ip1,c1*(d-B)))/c1;
   d=del+k*vx; r2=(rate(i02,c1*d)+rate(im2,c1*(d+B))+rate(ip2,c1*(d-B)))/c1;
   d=del-k*vy; r3=(rate(i03,c1*d)+rate(im3,c1*(d+B))+rate(ip3,c1*(d-B)))/c1;
   d=del+k*vy; r4=(rate(i04,c1*d)+rate(im4,c1*(d+B))+rate(ip4,c1*(d-B)))/c1;
   d=del-k*vz; r5=(rate(i05,c1*d)+rate(im5,c1*(d+B))+rate(ip5,c1*(d-B)))/c1;
   d=del+k*vz; r6=(rate(i06,c1*d)+rate(im6,c1*(d+B))+rate(ip6,c1*(d-B)))/c1;
/* absorption rates from each beam - see subroutine */
   r=r1+r2+r3+r4+r5+r6; /* total absorption rate */
   t1=1/r-t2;       /* absorption time */       T=T+t1+t2;   /* change in total time */
   xn=xo+t1*vx;     xbar=xo+0.5*vx*t1;
   yn=yo+t1*vy;     ybar=yo+0.5*vy*t1;
   zn=zo+t1*vz;      zbar=zo+0.5*vz*t1;
/* new and average positions immediately prior to absorption */
n=nint(xbar/dmax*jd+jd+1);     m=nint(ybar/dmax*jd+jd+1);
if (n<totd+1)
{ if (n>0)
{if (m>0)
{if (m<totd+1) {  XY[n][m]=XY[n][m]+t1;  }}
m=nint(zbar/dmax*jd+jd+1);
if (m>0)
{if (m<totd+1) {  XZ[n][m]=XZ[n][m]+t1;  }}
```

```
}
}          /* weighting the position 'bin' in which the atom is contained (with time) */
 p=ran2(idum);
    vX=vx;      vY=vy;     vZ=vz;
   if (p<r1/r)
     {   vX=vx+hk;    }
      else if (p<(r1+r2)/r)
     {   vX=vx-hk; }
      else if (p<(r1+r2+r3)/r)
     {   vY=vy+hk;      }
      else if (p<(r1+r2+r3+r4)/r)
     {   vY=vy-hk;      }
      else if (p<(r1+r2+r3+r4+r5)/r)
     {   vZ=vz+hk;      }
      else
     {   vZ=vz-hk;      }   /* statistical selection of the absorption beam */
xbar=xn+0.5*vX*t2;      ybar=yn+0.5*vY*t2;      zbar=zn+0.5*vZ*t2;
/* new and average positions immediately prior to emission */
n=nint(xbar/dmax*jd+jd+1); m=nint(ybar/dmax*jd+jd+1);
if (n<totd+1)
{if (n>0)
{if (m>0)
{if (m<totd+1)   {XY[n][m]=XY[n][m]+t2;}}
m=nint(zbar/dmax*jd+jd+1);
if (m>0)
{if (m<totd+1)   {XZ[n][m]=XZ[n][m]+t2;}}
}
}      /* weighting the position 'bin' in which the atom is contained (with time) */
n=nint(vx/vmax*jv+jv+1); m=nint(vy/vmax*jv+jv+1);
if (n<tot+1)
{if (n>0)
{if (m<tot+1)
{if (m>0)   {VXY[n][m]=VXY[n][m]+t1;}}
m=nint(vz/vmax*jv+jv+1);
if (m<tot+1)
{if (m>0)   {VXZ[n][m]=VXZ[n][m]+t1;}}
}
}    /* weighting the pre-absorption 'bin' of the atom */
n=nint(vx/vmax*jv+jv+1); m=nint(vy/vmax*jv+jv+1);
if (n<tot+1)
{if (n>0)
{if (m<tot+1)
{if (m>0)   {VXY[n][m]=VXY[n][m]+t2;}}
m=nint(vz/vmax*jv+jv+1);
if (m<tot+1)
{if (m>0)   {VXZ[n][m]=VXZ[n][m]+t2;}}
}
}    /* weighting the pre-emission 'bin' of the atom */
```

```c
p=1.0-2.0*ran2(idum);        q=sqrt(1-p*p);        l=2*pi*ran2(idum);
    xo=xn+t2*vX;        vx=vX+hk*p;
    yo=yn+t2*vY;        vy=vY+hk*q*cos(l);
    zo=zn+t2*vZ;        vz=vZ+hk*q*sin(l);
/* velocity change due to isotropic spontaneous emission */
}
 fp=fopen("aidan","wb");
 for(n=1;n<=tot;n++) { fwrite(VXY[n]+1,sizeof(double),tot,fp); }
 for(n=1;n<=tot;n++) { fwrite(VXZ[n]+1,sizeof(double),tot,fp); }
 fwrite(V+1,sizeof(double),tot,fp);
 for(n=1;n<=totd;n++) { fwrite(XY[n]+1,sizeof(double),totd,fp); }
 for(n=1;n<=totd;n++) { fwrite(XZ[n]+1,sizeof(double),totd,fp); }
 fwrite(D+1,sizeof(double),totd,fp);
/* writing the results to a file which MATLAB can read */
 free_dmatrix(VXY,1,tot,1,tot); free_dmatrix(VXZ,1,tot,1,tot);
 free_dmatrix(XY,1,totd,1,totd); free_dmatrix(XZ,1,totd,1,totd);
 free_dvector(V,1,tot); free_dvector(D,1,totd);
}
 double rate(double arg1,double arg2)
{    /* subroutine for absorption rate */
 extern double it;
 double ra;
 ra=arg1/(1+it+arg2*arg2);
 return ra;}
```

Bibliography

[1] C. S. Adams, H. J. Lee, N. Davidson, M. Kasevich and S. Chu, Phys. Rev. Lett. **74**, 3577 (1995).

[2] M. H. Anderson, J. R. Ensher, M. R. Matthews, C. E. Wieman and E. A. Cornell, Science **269**, 198 (July 1995).

[3] M. T. de Araujo, L. G. Marcassa, S. C. Zilio, and V. S. Bagnato, Phys. Rev. A **51**, 4286 (1995).

[4] A. Ashkin, Phys. Rev. Lett. **24**, 156 (1970), and **25**, 1321 (1970).

[5] A. Aspect, E. Arimondo, R. Kaiser, N. Vansteenkiste and C. Cohen-Tannoudji, Phys. Rev. Lett **61**, 826 (1988).

[6] V. S. Bagnato, G. P. Lafyatis, A. Martin, K. Helmerson, J. Landry and D. E. Pritchard, J. Opt. Soc. Am. B **6**, 2171 (1989).

[7] V. S. Bagnato, L. G. Marcassa, M. Oria, G. I. Surdutovich, R. Vitlina and S. C. Zilio, Phys. Rev. A **48**, 3771 (1993).

[8] V. I. Balykin, V. S. Ltokhov and V. I. Mushin, JETP Lett. **29**, 560 (1979).

[9] C. C. Bradley, C. A. Sackett, J. J. Tollett and R. G. Hulet, Phys Rev. Lett. **75**, 1687 (1995).

[10] S. Chu, L. Hollberg, J. E. Bjorkholm, A. Cable and A. Ashkin, Phys. Rev. Lett. **55**, 48, (1985).

[11] S. Chu, Scientific American, 49 (Feb. 1992).

[12] S. Chu, Science **253**, 861 (1991).

[13] C. N. Cohen-Tannoudji and W. D. Phillips, Physics Today, 33 (Oct. 1990).

[14] C. J. Cooper, G. Hillenbrand, J. Rink, C. G. Townsend, K. Zetie and C. J. Foot, Europhys. Lett. **28**, 397 (Nov. 1994).

[15] A. Corney, *Atomic and Laser Spectroscopy*, Oxford University Press, Oxford, 1979, p. 39.

[16] J. Dalibard and C. Cohen-Tannoudji, J. Opt. Soc. Am. B **2**, 1707 (1985).

[17] J. Dalibard and C. Cohen-Tannoudji, J. Opt. Soc. Am. B **6**, 2023 (1989).

[18] T. Dalibard, Opt. Commun. **68**, 203 (1986).

[19] K. B. Davis, M-O. Mewes, M. A. Joffe, M. R. Andrews and W. Ketterle, Phys. Rev. Lett. **74**, 5202 (1995).

[20] K. B. Davis, M-O. Mewes, M. R. Andrews, N. J. van Druten, D. S. Durfee, D. M. Kurn and W. Ketterle, Phys. Rev. Lett. **75**, 3969 (1995).

[21] M. R. Doery, E. J. D. Vredenbregt and T. Bergeman, Phys Rev. A **51**, 4881 (1995).

[22] M. Drewsen, Ph. Laurent, A. Nadir, G. Santarelli, A. Clairon, Y. Castin, D. Grison, C. Salomon, Appl. Phys B **59**, 283 (1994).

[23] J. Eschner and I. Littler: recents experiments at the Australian National University.

[24] C. J. Foot, Contemporary Physics, **32**^{6}, 369 (1991).

[25] A. Friederich, Hons. Thesis, Australian Nat. Uni., 1994.

[26] R. Gaggl, L. Windholz, C. Umfer and C. Neureiter, Phys. Rev. A **49**, 1119 (1994).

[27] M. Gajda and J. Mostowski, Phys. Rev. A **49**, 4864 (1994).

[28] P. L. Gould, P. D. Lett and W. D. Phillips, in *Laser Spectroscopy VIII*, edited by W. Persson and S. Svanberg, Springer-Verlag, 1987, pp. 64-67.

[29] I. Guedes, M. T. de Araujo, D. M. B. P. Milori, G. I. Surdutovich, V. S. Bagnato and S. C. Zilio, J. Opt. Soc. Am. B **11**, 1935 (1994).

[30] R. Gupta, S. Padua, C. Xie, H. Batelaan and H. Metcalf, J. Opt. Soc. Am. B **11**, 537 (1994).

[31] T. W. Hänsch and A. L. Schawlow, Opt. Commun. **13**, 68 (1975).

[32] S. Haroche, J. C. Gay, G. Grynberg, eds., *Atomic Physics 11*, World Scientific, Singapore (1989), pp. 633 & 636.

[33] A. Hemmerich, D. Schropp and T. W. Hänsch, Phys. Rev. A **44**, 1910 (1991).

[34] A. Hemmerich and T. W. Hänsch, Phys. Rev. Lett. **68**, 1492 (1992).

[35] B. Hoeling and R. J. Knize, Optics Comm. **106**, 202 (1994).

[36] A. Höpe, D. Haubrich, H. Schadwinkel, F. Strauch and D. Meschede, Europhys. Lett. **28**, 7 (1994).

[37] W. M. Itano, J. C. Bergquist and D. J. Wineland, Science **237**, 612 (1987).

[38] M. A. Kasevich, E. Riis, S. Chu and R. G. DeVoe, Phys. Rev. Lett. **63**, 612 (1989).

[39] M. A. Kasevich, D. S. Weiss and S. Chu, Optics Lett. **15**, 607 (1990).

[40] A. P. Kazantsev, G. I. Surdutovich, D. O. Chudesnikov and V. P. Yakovlev, J. Opt. Soc. Am. B **6**, 2130 (1989).

[41] W. Ketterle, K. B. Davis, M. A. Joffe, A. Martin and D. E. Pritchard, Phys. Rev. Lett. **70**, 2253 (1993).

[42] P. D. Lett, R. N. Watts, C. I. Westbrook, W. D. Phillips, P. L. Gould and H. J. Metcalf, Phys. Rev. Lett. **61**, 169 (1988).

[43] P. D. Lett, W. D. Phillips, S. L. Rolston, C. E. Tanner, R. N. Watts and C. I. Westbrook, J. Opt. Soc. Am. B **6**, 2084 (1989).

[44] K. Lindquist, M. Stephens and C. Wieman, Phys. Rev. A **46**, 4082 (1992).

[45] G. Mandl, *Mechanics of Tectonic Faulting - Models and Basic Concepts*, Elsevier Science Publishing Co., Amsterdam, 1988.

[46] A. G. Martin, K. Helmerson, V. S. Bagnato, G. P. Lafyatis and D. E. Pritchard, Phys. Rev. Lett. **61**, 2431 (1988).

[47] H. Metcalf, J. Opt. Soc. Am. B **6**, 2207 (1989).

[48] A. L. Migdall, J. V. Prodan and W. D. Phillips, Phys. Rev. Lett. **54**, 2596 (1985).

[49] K. Mølmer, Phys. Rev. A **44**, 5820 (1991).

[50] C. Monroe, W. Swann, H. Robinson and C. Wieman, Phys. Rev. Lett. **65**, 1571 (1990).

[51] C. Monroe, PhD. Thesis, Uni. of Colorado, 1992.

[52] Peck, E. R., *Electricity and Magnetism*, McGraw-Hill, New York, 1953, pp. 206, 262-263.

[53] W. Petrich, M. H. Anderson, J. R. Ensher and E. A. Cornell, J. Opt. Soc. Am. B **11**, 1332 (1994)

[54] W. Petrich, M. H. Anderson, J. R. Ensher and E. A. Cornell, Phys. Rev. Lett. **74**, 3352 (1995).

[55] W. D. Phillips and H. Metcalf, Phys. Rev. Lett. **48**, 596 (1982).

[56] W. D. Phillips, P. L. Gould and P. D. Lett, Science **239**, 877 (1988).

[57] Press, W. H., Teukolsky, S. A., Vetterling, W. T., Flannery, B. P., *Numerical Recipes in C: the Art of Scientific Computing*, Cambridge University Press, New York, 1992, pp 274-304.

[58] E. L. Raab, M. Prentiss, A. Cable, S. Chu and D. E. Pritchard, Phys. Rev. Lett. **59**, 2631 (1987).

[59] Reif, F., *Fundamentals of Statistical and Thermal Physics*, McGraw-Hill, Tokyo, 1965, pp. 574-7, 584.

[60] Risken, H., *The Fokker-Planck Equation: Methods of Solution and Application*, Springer-Verlag, Berlin, 1989, pp. 7-8.

[61] T. M. Roach, H. Abele, M. G. Boshier, F. Gahbauer, H. L. Grossman, K. P. Zetie and E. A. Hinds, Phys. Rev. Lett. **75**, 629 (1995).

[62] W. J. Rowlands, D. C. Lau, G. I. Opat, A. I. Sidorov, R. J. McLean and P. Hannaford, Phys. Rev. Lett. (to be published).

[63] C. Salomon, A. Aspect, H. Metcalf and C. Cohen-Tannoudji, Phys. Rev. Lett. **59**, 1659 (1987).

[64] C. Salomon, J. Dalibard, W. D. Phillips, A. Clairon and S. Guellati, Europhys. Lett. **12**, 683 (1990).

[65] D. W. Sesko, T. G. Walker and C. E. Wieman, J. Opt. Soc. Am. B **8**, 946 (1991).

[66] Shadowitz, A., *The Electromagnetic Field*, McGraw-Hill, New York, 1975, pp. 204-205.

[67] S-Q. Shang, B. Sheehy, P. van der Straten and H. Metcalf, Phys. Rev. Lett. **65**, 317 (1990).

[68] Y. Shevy, D. S. Weiss, P. J. Ungar and S. Chu, Phys. Rev. Lett. **62**, 1118 (1989).

[69] A. M. Steane, PhD thesis, University of Oxford, 1991. Europhys. Lett. **14**, 231 (1991).

[70] A. M. Steane and C. J. Foot, Europhys. Lett. **14**, 231 (1991).

[71] A. M. Steane and C. J. Foot, J. Opt. Soc. Am. B **9**, 2142 (1992).

[72] S. Stenholm, Rev. Mod. Phys. **58**, 699 (1986).

[73] Terman, F. E., *Radio Engineers' Handbook*, McGraw-Hill, New York, 1943, pp. 63, 72.

[74] C. G. Townsend, N. H. Edwards, C. J. Cooper, K. P. Zetie, C. J. Foot, A. M. Steane, P. Szriftgiser, H. Perrin and J. Dalibard, Phys. Rev. A **52**, 1423 (1995).

[75] P. J. Ungar, D. S. Weiss, E. Riis, and S. Chu, J. Opt. Soc. Am. B **6**, 2058 (1989).

[76] T. Walker, D. Sesko and C. Wieman, Phys. Rev. Lett. **64**, 408 (1990).

[77] T. Walker, D. Hoffman, P. Feng, R. S. Williamson III, Physics Lett. A **163**, 309 (1992).

[78] D. S. Weiss, E. Riis, Y. Shevy, P. J. Ungar and S. Chu, J. Opt. Soc. Am. B **6**, 2072 (1989).

[79] C. I. Westbrook, R. N. Watts, C. E. Tanner, S. L. Rolston, W. D. Phillips and P. D. Lett, Phys. Rev. Lett. **65**, 33 (1990).

[80] C. Wieman, G. Flowers and S. Gilbert, Amer. J. Phys. **63**, 317 (1995).

[81] J. Wloka, *Partial Differential Equations*, Cambridge University Press, Cambridge, 1987.